Unsteadiness of Blood Flow in 90-degree Bifurcations

by

Stevin van Wyk

Licentiate Thesis
in
Engineering Mechanics

December 2011
Technical Reports from
Royal Institute of Technology
KTH Mechanics
SE-100 44 Stockholm, Sweden

Akademisk avhandling som med tillstånd av Kungliga Tekniska Högskolan i Stockholm framlägges till offentlig granskning för avläggande av teknologie licentiatexamen Torsdagen den 8 december 2011 kl 10:00 i sal E3, Osquarsbacke 14, Kungliga Tekniska Högskolan, Stockholm.

TRITA-MEK Technical report 2011:16
ISRN KTH/MEK/TR–11/16–SE
ISSN 0348-467X
ISBN 978-91-7501-194-3

Universitetsservice US–AB, Stockholm 2011

Unsteadiness of Blood Flow in 90-degree Bifurcations

Stevin van Wyk 2011

KTH Department of Mechanics
SE-100 44 Stockholm, Sweden

Abstract

The blood is a complex fluid that contains, in addition to water, cells, macromolecules and a large number of smaller molecules. The physical properties of the blood are therefore the result of non-linear combination of its constituents. Hence, the blood viscosity depends on the local flow field itself. The local blood viscosity conditions determine the local concentration of the blood constituents. This study considers blood like flows in generalised 90-degree arterial bifurcations relevant to the large aortic branches in humans. It is shown that the Red Blood Cell (RBC) distribution in the region of bifurcations may lead to changes in concentration. This implies changes to the viscosity that changes the fluid mechanical properties in the near wall regions, for example, playing a role in arterial disease development. Furthermore, it is shown that oscillatory wall shear stresses, are affected by changes in RBC concentration in the regions of the bifurcation associated with atherogenesis. More importantly, an intrinsic rhoelogical property of blood, in conjunction with stagnation in separated flows, may be responsible for elevated temporal wall shear stress gradients influencing endothelial cell function.

Descriptors: Blood Rheology, Viscosity, CFD, Bifurcations, Unsteadiness, Wall Shear Stress.

Papers and Division of authors contributions

The main advisor of the project is Professor Laszlo Fuchs and co-advisor Doctor Lisa Prahl Wittberg of the department of Mechanics, KTH.

Paper 1

Haemodynamics in a 3D 90-degree bifurcation.
S. van Wyk (SvW), L. Prahl Wittberg (LPW) & L. Fuchs (LF)
Proceedings of the ECCOMAS Thematic International Conference on Simulation and Modeling of Biological Flows (SIMBIO 2011) September 21-23, 2011, VUB, Brussels, Belgium

The analyses and simulations have been performed by SvW as well as the writing, with help from LPW and LF. LPW also helped with structuring of the paper.

Paper 2

Wall shear stress variations and unsteadiness of pulsatile blood-like flows in 90-degree bifurcations
S. van Wyk (SvW), L. Prahl Wittberg (LPW) & L. Fuchs (LF)
To be submitted to Medical Engineering and Physics in December 2011 .

SvW has carried out the simulations, writing and the analyses with the help of LF and LPW. LPW and LF helped with reading, commenting and structuring of the paper.

Confusion is a word we have invented for an order which is not understood.

Henry Miller (Novelist & painter, 1891-1980)

Contents

Part I

Overview

CHAPTER 1

Introduction

Blood flow is essential for maintaining the functionality of the human body. The circulatory system is responsible for the delivery of oxygen, nutrients and substances needed by the cells in addition to removing waste products. However, there are critical health issues stemming from pathological changes in the blood vessel leading to cardiovascular diseases (CVD). CVD is related to half of all mortalities in Sweden. CVD related illness is responsible for the largest share of the costs of public health care.

The understanding and consideration of the multiphase flow mechanisms in the modelling of blood flow is important in the study of macroscopic, physiological flow parameters. The rheological properties of blood can be simplified to being described as a two phase fluid, due to the dominance of the bulk red blood cell (RBC) (the haematocrit phase) making up approximately 95 % of the particulate or suspended phases. Blood viscosity has therefore been commonly correlated to fixed, homogeneous bulk haematocrit fractions and the shear rate, which directly influences the RBC alignment and interactions (Carreau 1972; Casson 1959; Merrill *et al.* 1966; Walburn & Schneck 1976). Empirical relations have also been developed for non-Newtonian viscosity models that account for the variation in haematocrit fraction (Cockelet 1987; Cockelet *et al.* 1963; Walburn & Schneck 1976). The non-Newtonian relations, developed between the 1950's and 80's, are applied in modelling the two phase behaviour from a bulk macroscopic flow perspective, assuming homogeneous mixtures of varying haematocrit fractions in discretized volumes of an arterial domain. Since the dynamics of RBCs are not well understood. The basic hypothesis in this work is that the local concentration of RBCs is non-homogenous but it is a function of space and time. Non-uniformity of RBC concentration (and possibly also of large molecules) implies that the blood viscosity also varies in space and time. This by itself leads to an additional non-linearity of blood flows.

The variations in mass transport due to the variation of the blood rheology, affects the dynamics of other macromolecules and blood-cells thought to be important in the artherogenic process (Ross *et al.* 1999). In the understanding of atherogenesis it has historically been strongly linked to the localized flow characteristics, usually separation and reversed flow (Caro & Lighthill 1966; Duguid & Robertson 1957; McDonald 1960). Plaque formation has been observed in regions of arterial curvature or bifurcation, where these flow structures exist (DeBakey *et al.* 1985; VanderLaan *et al.* 2004). Important physiological parameters, commonly related to the location of atherogenesis is the variation in wall shear stress (WSS). Many authors correlate atherogenesis to either regions of low WSS, low time-averaged and oscillatory WSS or simply flow unsteadiness (Caro *et al.* 1969, 1971; Ku *et al.* 1985; Zarins *et al.* 1983). It is thought that these flow parameters are associated with regions where either mass transport is altered or the endothelium are disturbed

(Ross *et al.* 1999). The evolution of the WSS is dependent on the local viscosity that in turn is dependent on the local haematocrit fraction.

This study aims to increase the knowledge for and quantification of the local RBC concentration (haematocrit) in 90-degree arterial like bifurcations. Four coupled non-Newtonian viscosity models are implemented in order to model a blood like fluid, where the coupling is defined by dependencies on shear rate and local haematocrit fraction. The WSS parameters are analysed in detail for varying load conditions in relation to observed development of atherosclerosis.

CHAPTER 2

Circulation Physiology and the Blood

2.1. Circulation Physiology

The circulatory system is one of the most important components in the functioning or maintenance of the human body. The heart and the vascular network together define the circulatory system transporting all oxygen, nutrients, hormones and by-products to and from the cells, essential to bodily processes. The circulatory system, together with the blood also help regulate the cellular pH and body temperature.

2.1.1. *The Heart and Vascular Network*

The blood is pumped through the body via the vascular network by a muscular organ, the heart. The heart is located in the left, central region of the chest, near the lungs. It consists of four chambers, two ventricles and two atria. The atria fulfill the purpose of collecting blood to supply the ventricles. The ventricles have thicker muscle walls as compared to the atria due to the fact that the ventricles have to withstand greater blood pressures. The left atrium has the thickest muscular walls because it supplies most of the body with blood, imposing a higher resistance and higher pressure. The flow sequence through the heart can be described in four main steps:

1. Blood flows into the right atrium, supplied with de-oxygenated blood by the superior and inferior venae cavae and the coronary sinus. The right atrium is separated from the right ventricle by the tri-cuspid valve.
2. The right ventricle pumps the blood via the pulmonary artery, regulated by the pulmonary valve, to the lungs where the blood is re-oxygenated.
3. The re-oxygenated blood then flows back into the heart, into the left atrium via the pulmonary veins. The left atrium is separated from the left ventricle by mitral valve.
4. Flow of the oxygen rich blood to the rest of the body is maintained by the left ventricle via the ascending aorta, regulated by the aortic valve.

The circulation (vascular network) physiology is formally divided into two parts, the systemic and pulmonary circulations. The systemic circulation refers to circulation that supplies the oxygenated blood to the cells in the rest of the body. It makes up approximately 83% of the total blood volume in the body, where diastolic and systolic pressures are in the range of 80 and 120 mmHg (11 and 16 kPa). The pulmonary circulation transports blood via the lungs for re-oxygenation and carbon dioxide removal containing approximately 12% of the total blood volume. The rest of the blood volume is contained in the heart, 5 %. Each of these circulatory networks consists of three main vessel types; the arteries transporting blood away from the heart, the capillaries that deliver and distribute nutrients at the different organs and the veins that transport blood towards the heart. In the pulmonary

circulation systolic and diastolic pressures are much lower in the range 20 and 30 mmHg. The flow properties and vascular dimensions throughout the circulatory network vary substantially depending on the distance from the heart, shown in Table 2.1. The systemic artery closest to the heart has the largest cross-section (i.e. the so called ascending aorta). It initially extends upwards from the heart and has multiple branches starting with the aortic arch, where there is a set of bifurcations forming the carotid arteries leading blood to the head and branches leading blood to the arms. The aorta makes a large turn continuing down through the chest and abdominal cavity forming the thoracic and abdominal aorta sections. There are large more or less symmetric branches off the abdominal aorta, namely the renal and iliac arteries that lead towards the kidneys and legs, respectively. The angles of these bifurcations from the aorta are closer to 90^0 (Pedley 1980; Tortora & Derrickson 2006). Figure 2.2 depicts a schematic drawing of some of the larger arteries of the human body. The flow rates (mean velocities) in some arteries, shown in Table 2.1, depend on the individual and the degree of physical effort. Also given are the Reynolds (Re_p) and Womersley (α_p) numbers quoted, equations 2.1 and 2.2 respectively. Here, one uses the viscosity of the plasma (which is the blood minus the cells which means that it is water containing large and small molecules).

$$Re_p = \frac{U_0 D \rho_p}{\mu_p} \tag{2.1}$$

$$\alpha_p = \frac{D}{2}\sqrt{\frac{\omega \rho_p}{\mu_p}} \tag{2.2}$$

where the plasma density (ρ_p) and dynamic viscosity (μ_p) are defined in Table 2.2.

TABLE 2.1. Human systemic and pulmonary circulation physiological properties. Data taken from Bronzino (2000); Caro *et al.* (1978); Charm & Kurland (1974)

Vasculature	Internal diameter range (D, mm)	Mean peak velocity (U_0, m/s)	Re_p	α_p
Ascending Aorta	∼15	∼0.18	∼2100	∼21
Abdominal Aorta	∼9	∼0.14	∼1000	∼12
Renal Artery	∼5	∼0.40	∼1500	∼4
Femoral Artery	∼4	∼0.12	∼400	∼4
Pulmonary Artery	20-30	∼0.19	∼3700	∼20

The blood vessels consist of several wall layers that have different functional characteristics. Depending on the location of the vessel in the systemic or pulmonary circulations, it can be subjected to lower or higher pressures. The arterial wall structure consists of the three main layers; Tunica Intima (Intima), Tunica Media (Media) and the Tunica Adventitia (Adventitia). The Intima is the inner most layer made up mostly of endothelial cells that are directly exposed to the flow. These cells form the inner most layer for all vessels. There is also a basement

membrane and a layer of elastic tissue called the elastica intima, between the endothelium and the Media. The thickest of the layers is the Media attached to the Elastica Intima, consisting mostly of smooth muscle cells and elastic tissue that stretch around the vessel. The Smooth Muscles are covered by a layer of elastic tissue called the elastica Media. Smooth muscle tone is controlled to stiffen when the pressure in the flow increases, maintaining the arterial form (Bronzino 2000). The outer most layer is the Adventitia composed of connective tissue. The arterial cavity carrying the blood is called the Lumen. Figure 2.1 shows a schematic picture of the arterial structure. Veins have thinner walls as compared to arteries and in particular it has a thin media with few smooth muscle cells. The down scaling appears in the two inner most layers where there is only a thin smooth muscle layer, making the Adventitia the thickest layer in veins. The smooth muscle in veins is not as important as in arteries, because veins do not function in a contractile manner and they have to support only the pressure found in the post-capillary vessels.

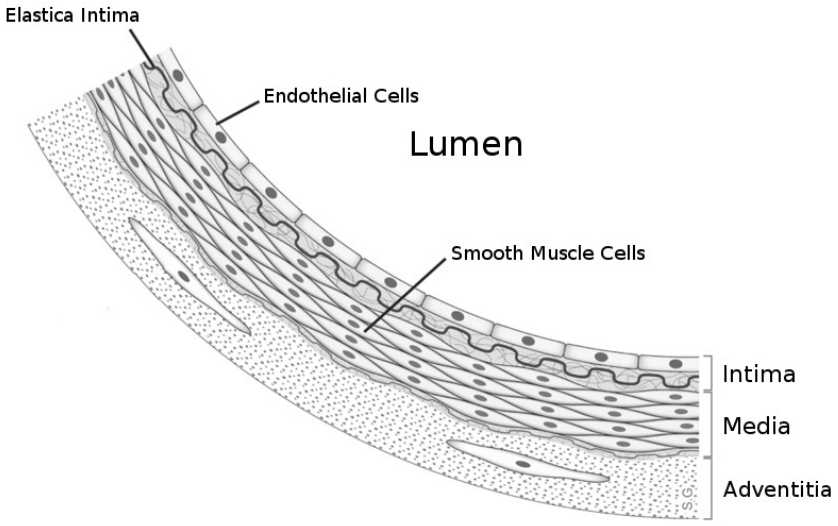

FIGURE 2.1. A schematic view of the layers of the arterial wall structure

2.1.2. *The Pathology of Atherosclerosis*

Atherosclerosis is a focal, multifactorial vascular disease that tends to occur in arterial regions where the flow is disrupted with strong flow unsteadiness, secondary flows and presence of flow separation. (DeBakey *et al.* 1985; VanderLaan *et al.* 2004). It is a slowly evolving disease (may take up to several decades) affecting the intimal layer of the vessel wall, characterized by a localized fibro-fatty plaque build-up under the endothelial layer. It often leads to obstruction of the lumen (stenosis), eventually leading to blood clot formation or thrombosis, subsequently blocking the vessel. The most commonly mentioned factors to influence the progression of the disease are smoking, obesity, nutrition, genetics and infection. Other less obvious influences, increasing the risk of development have been identified to be age, gender

and diseases such as diabetes (Bakhru & Erlinger 2005; Farmer & Gotto 1997; Ferdowsian & Barnard 2009; Sinha *et al.* 2009; Streppel *et al.* 2009). The process of development is not fully understood due to its complexity, considering both biomechanical and biochemistry processes. One of the key factors studied over the last two decades is the inflammation process, thought to participate in all stages of atherogensis (Libby *et al.* 2002; Montecucco & Mach 2009; Ross *et al.* 1999).

2.1.2a. *The Process and Localization.* The process of atherogenesis is described by many researchers (Libby *et al.* 2010; Raja BS 2002; Weissberg 2000), summarized as follows:

1. The first stage is an accumulation of lipid under the endothelium, the beginning stage of the forming of a fatty streak.
2. Endothelial cell activation entails extending molecules (selectins and adhesion molecules) from the surface that attracts and captures inflammatory cells (macrophages, T-cells and mast cells) in the circulation. 'This facilitates their migration into the subendothelial space' (Weissberg 2000).
3. Once the inflammatory cells are captured, the cells migrate into the subendothelial space created by the lipid accumulation. Activation of the cells then takes place by local proinflammatory chemokines, where the monocytes mature. The main role of macrophages is to ingest and dispose of the lipids, becoming macrophage foam cells. However, the activated inflammatory cells contribute to the plaque evolution.
4. Vascular smooth muscle cells (VSMC) are recruited into the intima and subsequently proliferate. The necessary proteins to form a fibrous cap are produced, maintaining stability and protection for the plaque against rupture and subsequent thrombosis.
5. Inhibited VSMC proliferation or VSMC death, due to inflammatory cell influence, leads to weakening or erosion of the fibrous cap and possible rupture.
6. The rupture or erosion of the cap leads to platelet accumulation. This leads to fibrin formation, followed by thrombosis. In extreme cases the lumen is occluded.

Initially, the pathological changes in the aortic wall are localized to the aortic arch and the renal bifurcation. Over time one may find lesions at larger number of locations throughout the aorta and its larger branches where plaques usually form. The onset of atherosclerosis tends to form near bifurcations or major curvatures in the vascular geometry (Gimbrone Jr *et al.* 2000). An arterial plaque distribution is shown in Figure 2.2, where the darker shaded, most affected regions, are the carotid arteries, the renal arteries, the iliac arteries and the bifurcations with the abdominal aorta (DeBakey *et al.* 1985; Stary 2000; Stary *et al.* 1992; VanderLaan *et al.* 2004). Each specific location is shown to cover a broad arterial region due to the patient specific variability in arterial geometry and the rate of plaque development (Friedman *et al.* 1983).

2.1.2b. *Fluid Mechanical Aspects.* The influence of haemodynamics on Atherogenesis has been studied for many years. Several hypotheses have been proposed in the attempt to relate the development to distinct mechanisms of the flow. Over the last 60 years experimental and numerical studies have related disturbed and separated flow conditions, in the regions of bifurcations, to the susceptibility of atherosclerotic

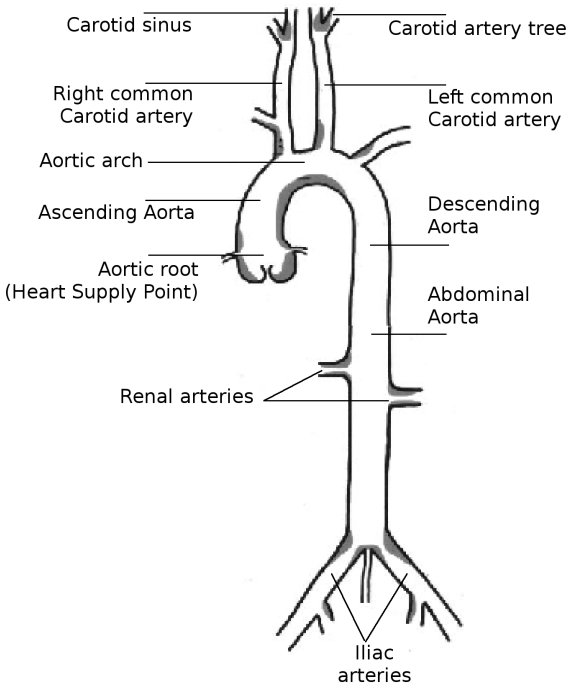

FIGURE 2.2. The sketch of the vascular network and typical plaque distribution. The grey regions show the localization of atherosclerosis (DeBakey *et al.* 1985; VanderLaan *et al.* 2004)

formation. Wall shear stress (WSS) magnitudes, distributions and gradients have in recent times become the focal point of study. These fluid mechanical parameters are thought to be related to endothelial dysfunction, endothelial erosion or mechanical damage and enhanced mass transport of solutes to the affected areas (Caro 2009; Gimbrone Jr *et al.* 2000; VanderLaan *et al.* 2004).

For many years the belief was that high levels of WSS lead to arterial wall damage and was the explanation for the localized development of atherosclerosis. This hypothesis was first hypothesised by Duguid & Robertson (1957) and later McDonald (1960) relating the maximum shear stresses to the most common atherosclerotic sites. Major contributions were made by Fry (1968) relating morphological changes to endothelial cells and enhanced, non-uniform protein transport to increased levels of shear stress. Endothelial cell structure was found to be retained below shear stresses of 38 Pa, above which severe deterioration was observed. The study by Fry (1968) represents extreme stenotic flows and thresholds of endothelial cells. No direct relation to atherosclerosis was made, although it was suggested that high WSS values could exist near branches. The WSS value quoted by Fry (1968) is approximately an order of magnitude larger than WSS magnitudes commonly associated with non-stenosed bifurcations, quoted in works to follow. Experimental work carried out by Friedman *et al.* (1981) on a human aortic bifurcation model showed there was no correlation between higher WSS and intimal thickness. Bharadvaj *et al.* (1982a) also showed that regions subject to higher WSS tend to be free of disease.

Caro (1966); Caro & Lighthill (1966) recognized that branching and curvature are important arterial features, indicating the presence of secondary flow and large wall shear variations in these regions. Caro *et al.* (1969, 1971) went on to correlate regions of low WSS with early atheroma and relating the WSS to mass transport processes. A 'low' WSS is defined to be lower relative to the peak in the branch domain, outer versus inner wall magnitudes. It has now been widely confirmed that there is a correlation between low WSS regions and plaque distribution, as described by Lee & Chiu (1996). Pulsatile 2D Numerical simulations by Friedman *et al.* (1975) showed flow separation and large variations to the WSS. Friedman *et al.* (1975) emphasized the influence of transient flow behaviour on the arterial wall, reporting values for WSS of $\sim$3 Pa. Bharadvaj *et al.* (1982a,b) carried out steady flow experiments and stated that zones susceptible to disease formation experienced low or oscillatory WSS related to low or reversed axial flow. Peak WSS values were found to range between 2.5 and 5 Pa. Pulsatile flow experiments carried out by Ku *et al.* (1985) also produced similar ranges of WSS between 1 and 4.1 Pa, found at the inner wall during diastole and systole, respectively. Furthermore, the location of thickest plaque was found to be at the outer wall where the WSS is the lowest and oscillatory, between -0.7 and 0.4 Pa. Zarins *et al.* (1983) also concluded that intimal thickening and atherosclerosis show preference to regions of low and oscillatory shear, ranging between 0 and -0.6 Pa at the outer wall, while ranging between 3.1 and 60 Pa at the inner wall. The magnitudes depend on the Reynolds. There is common agreement between several authors (Bharadvaj *et al.* 1982b; Caro 1966; Caro & Lighthill 1966; Jou & Berger 1998; Ku *et al.* 1985) concerning how the low and oscillating WSS stresses increase fluid residence time and thereby enhance gradual accumulation of atherogenic substances near the arterial wall due to the modified mass transport in the lumen.

The most commonly accepted hypotheses regarding the initiation of plaque formation, nowadays is that of low and oscillatory WSS. Low time averaged and oscillatory WSS have been found to adversely affect the anti-atherogenic properties of the endothelial cell layer (Birchall *et al.* 2006; Gambillara *et al.* 2005). Correlations between locations for atherosclerosis or intimal thickening and oscillatory or low time-averaged WSS have been repeatedly documented by several researchers (Gibson *et al.* 1993; Lee & Chiu 1996; Moore *et al.* 1994; Soulis *et al.* 2006; Zarins *et al.* 1983), where shear stresses range between 0.75 and 2.25 Pa (Soulis *et al.* 2006). DePaola *et al.* (1992); Farmakis *et al.* (2004); Nagel *et al.* (1999) on the other hand suggested that elevated WSS gradients affect the function of endothelium or cause endothelial dysfunction in regions of disturbed flow, enhancing atherogensis. A 3D simulation carried out with the same 90-degree branch geometry used during this study showed temporal and spatial gradients located in regions commonly associated with atherogenesis. However, similar WSS gradients were also found in other regions not commonly associated with plaque formation (Evegren *et al.* 2010).

Regions where intimal thickening have been shown to be the highest, display WSS values of less than 1.0 Pa, according to Wootton & Ku (1999). Wootton & Ku (1999) states that the arterial walls try to maintain a constant WSS of $\sim$ 1.5 Pa in high shear regions. Again, the difference between high and low WSS can be seen to be as little as 50 %, due to an inner and outer wall comparison of magnitudes. It is shown that regions of high uni-directional WSS tend to be free of plaque formation (Zarins *et al.* 1983). On the other hand, further growth of advanced plaques are

shown to be different to the processes involved in plaque initiation, happening under elevated high shear stress conditions (Tang *et al.* 2008; Yang *et al.* 2010). Experiments carried out by Friedman *et al.* (1986) indicated that intimal thickness growth increased rapidly initially in regions of high shear but then the growth is slowed down dramatically. Whilst, areas of lower shear showed a relatively constant but slower thickness development, eventually surpassing the higher shear areas.

2.2. The Blood

Blood is a multiphase fluid with a dense suspension of cells in plasma. The non-Newtonian behavioural property of blood was discovered already by Hess in 1915, who found that blood viscosity was shear dependent. It has also been shown that blood exhibits viscoelastic and thixotropic behaviour caused by the formation of RBC microstructures that break-up at higher flow rates (Chien 1970; Thurston 1979, 1994). The rheological characteristics of the blood will be described in more detail in the following paragraphs.

2.2.1. *Blood Plasma and the Cellular Elements*

The volume of blood existing in each adult human is between 4 to 6 litres, with a density of approximately 1060 kg/m^3 in a homogeneous state (Brooks *et al.* 1970; Cutnell & Johnson 1998). When all particles or cellular components are removed the carrier fluid plasma remains and makes up 55% of the blood volume. It is an aqueous solution with 8% organic and inorganic solutes in low concentrations. Proteins make up approximatley 7% of these solutes. One of these proteins, fibrinogen, has been suggested as being the pincipal agent responsible for the RBC aggregating capacity of plasma. Aggregation capacity has been found to increase with increasing fibrinogen concentration (Merrill *et al.* 1963*a*). The properties of plasma are displayed in Table 2.2.

TABLE 2.2. Plasma properties at 37^oC. Data taken from Bronzino (2000); Burton (1965); Caro *et al.* (1978)

Contituents:	*Water*	92
Mass fraction (%)	*Proteins*	7
	Inorganic Salts	1
Dynamic viscosity (μ_p, $mPas$)		1.32
Density (rho_p, kg/m^3)		1025

The cellular elements in the blood can be split up into three main groups; Erythrocytes (RBCs), Leukocytes and Thrombocytes, shown in Table 2.3. The Leukocytes, or White Blood Cells (WBC), exist in several different forms, as described in Table 2.3. The WBC are the largest of the cells and roughly spherical in shape, perform as part of the body's defence and are much lower in concentration than RBCs. The Thrombocytes, or Platelets, are the smallest of the cellular elements. The Platelets are disk shaped and induce the important process of coagulation when a wound is sustained, rushing to the affected area to form a plug to

stop the bleeding. RBCs dominate the cellular element fraction in blood representing 99% of the mass fraction of the cellular elements. Therefore the RBCs are the most important phase in defining the viscosity and will be described in more detail in the sections to follow.

TABLE 2.3. The cellullar constituents of human blood. Data taken from Caro *et al.* (1978)

Cell type	***Number per*** mm^3	***Unstressed Shape & Dimension*** (μm)	***Volume fraction of Blood (%)***
Red Blood Cells	4-6 million	Bi-concave disc 8 x 1 x 2	45
Leucocytes (Monocytes, Lymphocytes & Granulocytes)	4-11 thousand	Roughly Spherical 7-22	1
Platelets	250-500 thousand	Oval disc 2-4	

2.2.2. *RBCs and Microstructural Behaviour*

The Red Blood Cell is bi-concave disk approximately 6-8 μm in diameter, 2-3 μm at its thickest point and 1 μm at its thinnest (Caro *et al.* 1978). On average the RBCs make up approximately 45% of the blood volume at normal levels (Bronzino 2000; Cutnell & Johnson 1998; Lowe *et al.* 1993), and the collective or bulk terminology is the haematocrit. Each RBC is made up of an elastic, permeable membrane enclosing the interior fluid constituted of water, haemoglobin and inorganic compounds. The elastic membrane allows RBCs to deform and squeeze their way through the narrowest of capillaries to the extremities of the body. Haemoglobin gives blood its red colour and carries the oxygen. The viscosity of the interior fluid is strongly influenced by the concentration of haemoglobin and can be between 1 and 6 $mPas$ (Dintenfass 1968a,b), also including membrane effects. Table 2.4 below displays all physical properties of the RBC.

The microstructure in blood defined by the concentrated particle suspension, is dominated by the RBCs. According to Chien (1970), two qualitatively distinct microstructures exist in response to the flow conditions. At low shear rates (0-1 s^{-1}) the RBCs form an extended network of aggregates called rouleaux. With increasing shear rate the aggregates break up, decreasing the average aggregate size and thereby defining the non-Newtonian viscosity relationship. The aggregation, disaggregation and deformation properties of the RBCs are the dominating processes in the relation of the microstructure to the effective viscosity of blood. The effects of aggregation and deformation on the viscous behaviour has been documented by Chien (1970), shown in Figure 2.3. The hardening of RBCs leads to an almost Newtonian type fluid viscosity, where as the loss of aggregation capacity leads to a

TABLE 2.4. The Composition of the Red Blood Cell. Data taken from Bronzino (2000); Burton (1965); Caro *et al.* (1978).

Contents: *Mass fraction (%)*	***Water***	65
	***Membrane* components** (Proteins, Phospholipid & Cholestorol)	3
	Haemoglobin	32
Average Surface Area (μm^2)		$\sim$138
Average Volume (μm^3)		$\sim$94
Internal Aqueous Solution Viscosity ($mPas$)		$\sim$1-6
Density (kg/m^3)		$\sim$1100

decrease in peak viscosity at low shear rates ($\dot{\gamma} < 1s^{-1}$). The aggregation process is a reflection of the existence of a yield stress i.e. the flow shear stress required to initiate flow from rest state (Merrill *et al.* 1963*a*). The stronger the aggregation, i.e. higher concentration of fibrinogen, the higher the yield stress (Merrill *et al.* 1966, 1963*c*). RBCs in serum (plasma minus fibrinogen) also possess a yield stress, but approximately half of that with fibrinogen (Chien *et al.* 1966), shown in Figure 2.3. The yield stress can dramatically increase by only minute increases in fibrinogen (Copley *et al.* 1968).

2.2.3. *RBC Diffusivity and Tube Flow*

The mass diffusivity of RBCs is a consequence of several factors such as fluid shear, electrostatic forces and collisions. The few studies quantifying the enhanced diffusivity RBCs display due to shear, are restricted to flow in straight, narrow tubes on the capillary scale (Bishop *et al.* 2002; Cha & Beissinger 2001; Goldsmith & Marlow 1979). Steady flow conditions are the focus in all studies, not complex pulsatile flows. The experimental studies show that mass diffusivity in a concentrated suspension of RBCs may be very low, approximately of the order of magnitude 10^{-11} to 10^{-13} (m^2/s). Most studies are more interested in the diffusivity of Platelets, due to the influence during the later stages of atherogensis. The diffusivity of RBCs has been shown to be enhanced by the flow (Bishop *et al.* 2002; Cha & Beissinger 2001; Goldsmith & Marlow 1979; Hudson 2003; King & Leighton Jr 2001; Leighton & Acrivos 1987) and constrained by close packing of neighbouring particles (Cohen & De Schepper 1992), in concentrated suspensions. In the tube flow studies for blood, the RBCs are observed to migrate away from the walls due to hyrdrodynamic wall effects (Aarts *et al.* 1988; Goldsmith 1971; Goldsmith & Mason 1971). This migration effect dominates the movement of RBCs towards the centre of the channel, in large arteries. The 'caging effect' (Cohen & De Schepper 1992), caused by close neighbours, along with the migration effect, limits the diffusion component towards the walls. Therefore, in large arteries RBCs are thought to exist in lower concentrations near the wall. In contrast, at the capillary scale, Goldsmith & Marlow (1979) shows that RBC concentration increases towards the walls at normal

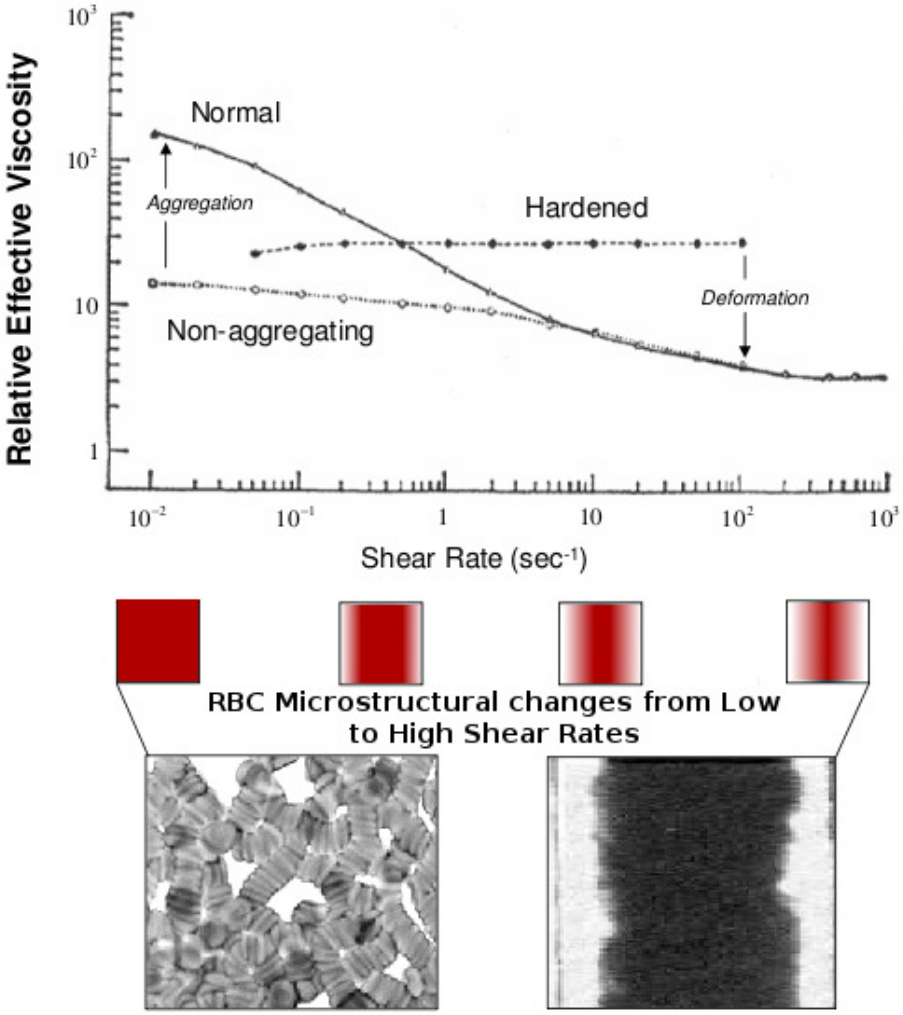

FIGURE 2.3. (top) Schematic of the relationship between the microstructure and the apparent viscosity. (bottom) The illustration of the RBC microstructure scales from the aggregation dominated regime at low shear and distribution at high shear. Data taken from Chien (1970); Chien *et al.* (1966).

bulk haematocrits (45%) with increasing flow rate. This is a capillary attributed property RBCs portray, related to deformation properties, not replicated in the larger vasculature flows.

Higher values of diffusivity could be expected during pulsatile flows in complex bifurcating domains where enhanced flow shear patterns, due to strong secondary flow, may further enhance diffusion. It is not yet known how transport of blood is affected in the region of bifurcations. In this study, a wide range of values is considered to represent the possible values for diffusivity that could occur in the large scale vascular regions of the circulation. An interesting observation in the region of bifurcations is the formation of a separation bubble. In 90-degree bifurcations, it is observed as a forced extension of the shear layer at the wall into the core, due to the centrifugal effect. The shear layer gradients at the wall and the separation bubble fluid boundary are therefore similar in magnitude. Therefore the majority of the RBCs can be expected to migrate away from the shear layer, as in tube flow. This should be true providing the shear gradients are comparably greater as compared to the inverse of the RBC dimensions. The shear induced migration is therefore dominant. In combination with the 'caging effect', it can be hypothesised that the transport of bulk RBCs (haematocrit) can be described to be dominated by advection. An expression for the particle Peclet number (Pe), a measure of the relative dominance of advection of the particles (RBCs) with respect to the particles diffusive properties, can be written according to Equation 2.3. It represents the reasoning behind the advection dominance on the RBCs, by the flow, in large arteries.

$$Pe = ReSc = \frac{U_0 D}{D_H} \sim \frac{U_0 D}{a^2 \dot{\gamma} f(H)} \sim \frac{D^2}{a^2} >> 1 \tag{2.3}$$

where Re is the Reynolds number, Sc is the Schmidt number, $U_0(m/s)$ is the peak inflow velocity, D is the inlet or main branch diameter, $\dot{\gamma}(s^{-1})$ is the shear rate, a is the equivalent spherical radius of the bi-concave disk shaped RBCs, H is the RBC volume fraction and $D_H(m^2/s)$ is the effective diffusivity of the RBCs. Typical values for D and a in this study i.e. D=13.2 mm and $a \approx$3.5 μm. In Equation 2.3, the shear rate has been approximated to be of the order of U_0/D in tube flow. D_H has been shown to be proportional to the product of the square of the particle radius and the shear rate, in tube flows of concentrated suspensions (Cha & Beissinger 2001; Leighton & Acrivos 1987; Nott & Brady 1994) These studies consider shear induced diffusion of RBCs and spherical particles. In the case of concentrated RBCs the shear induced diffusivity was found to decrease with increasing RBC volume fraction H at or above volume fractions of 45% (Cha & Beissinger 2001). Thus, D_H is shown to be proportional to $(a^2 \dot{\gamma} f(H))$ in Equation 2.3.

CHAPTER 3

Mixture Models

The following section describes viscosity relations developed for blood, implemented during this study. In the experimental and theoretical proposals to be reviewed, only the macroscopic or bulk properties of the blood are considered. From an experimental point of view, the parameters intended to describe the behavioural character are fixed by macroscopic measurements in viscometers and not the microscopic properties of the suspension. The effective viscosity the measurements define are not an intrinsic property of the suspension instead dependent on flow conditions and the averaging of the instrument used to measure (Barnes 1995, 2000). The blood is defined as a homogeneous mixture for each measurement and all the empirical relations defining the viscosity of blood can be termed mixture models. All constitutive models considered are time-independent and therefore the viscoelastic properties of the blood is not included. The viscosity of blood is strongly influenced by concentrated suspension behaviour due to the dynamics of the RBCs and will be introduced in short.

3.1. Blood Viscosity Models

Over the last five decades, a handful of non-Newtonian models have been developed, describing the shear thinning properties of blood. Many non-Newtonian constitutive models exist that have either been adapted or developed for blood. Four distinctly different models, from what can be viewed as four main model structure categories, are chosen to carry out this investigation. Each model is chosen for its consideration of parameters identified as being important for describing the behavioural nature of blood flow. The behavioural parameters include the existence of shear strength (shear stress required to initiate flow), Newtonian viscous limits, shear rate dependency and the dependency on cell and molecular composition (Charm & Kurland 1972; Wilkinson 1960). The following paragraphs will describe the models implemented. The four models chosen, quantifying the dynamic viscosity (μ) of Human blood, have been identified during this study as the most well developed and widely used. Three of the models are functions of both haematocrit and shear rate, while the fourth is a function based solely on the shear rate.

The most general shear-thinning relation that may be used to describe the phenomenological characteristics of the blood, without the dependence on haematocrit, is the well known power law model $\mu = k\dot{\gamma}^{(n-1)}$. This model can only represent a small part of the entire shear rate range. Multi-parameter models for the relationship between apparent viscosity (μ) and shear rate are more representative. A generalised three parameter model was theorized by Cross (1965, 1970):

$$\mu = \mu_\infty + (\mu_0 - \mu_\infty)[1 + k_{Cr}\dot{\gamma}^{(n_{Cr}-1)}] \tag{3.1}$$

where μ_0 and μ_∞ are the viscosities in the limits $\dot{\gamma} \to 0$ and $\dot{\gamma} \to \infty$, respectively, extending the power law model to a larger part of the phenomenological range.

The Newtonian viscosity value for Blood is commonly found to be the lowest viscosity (at high shear rates) of a homogeneous blood mixture at normal levels and approximately 3.5 times that of water. The haematocrit composition of blood at normal levels is about 45% on average, varying between individuals (Bronzino 2000; Cutnell & Johnson 1998; Lowe *et al.* 1993).

3.1.1. *Bird-Carreau model*

A model initially developed for polymers, the Bird-Carreau model, describes the reaction kinetics between particle chain formation and chain structure rupture due to varying shear rates. It is similar to the model postulated by Cross (1965, 1970) representing the reaction kinetics. The relation between limits is described by a similar power law relation that has been adapted to fit data for blood properties (Carreau 1972; Johnston *et al.* 2004; Soulis *et al.* 2008). It describes the viscosity by the following equation;

$$\mu = \mu_\infty + (\mu_0 - \mu_\infty)[1 + (\lambda\dot{\gamma})^2]^{\frac{n_C - 1}{2}} \tag{3.2}$$

where $\mu_0 = 0.056 Pas$ represents "zero shear viscosity", the viscosity value just before the fluid comes to rest; $\mu_\infty = 0.00345 Pas$ is the Newtonian viscosity or "infinite shear viscosity", the viscosity value at high shear rates; $\lambda = 3.313 s$ is the relaxation time constant for haematocrit and n_C is the power law index defining the degree of non-Newtonian behaviour. The Bird-Carreau model has been widely used with the values for the above constants. It represents the widest range of shear rates of the four models, however with no explicit RBC volume fraction correction or dependency.

3.1.2. *Casson model*

The Casson model, initially derived to describe the flow behaviour of printing ink, was suggested for application in the description of blood viscosity by Casson (1959). The basis for the suggestion was the similarities portrayed by blood, with respect to the shear rate and shear strength properties of the relation. The group size of the mutually attractive particles is a function of shear rate i.e. the aggregate size is a function of the shear rate, decreasing in size for higher shear rates. Shear strength of the suspension is another property defining the shear stress required to break the static structure and thereby initiate flow. The Casson model is expressed by equations 3.3 and 3.4, defined by the linear squared relation between shear stress and shear rate (Casson 1959; Charm & Kurland 1972).

$$\mu = \frac{\tau}{\dot{\gamma}} \tag{3.3}$$

$$\begin{aligned} &\frac{\tau}{\dot{\gamma}} = \frac{\left[\sqrt{k_C(H)\dot{\gamma}} + \sqrt{\tau_y(H)}\right]^2}{\dot{\gamma}} \quad \text{for} \quad \tau > \tau_y(H) \\ &\dot{\gamma} = 0 \quad \text{for} \quad \tau <= \tau_y(H) \end{aligned} \tag{3.4}$$

Terms $k_C(H)$ and $\tau_y(H)$ are functions of the haematocrit H as follows:

$$k_C(H) = \frac{\mu_p}{(1-H)^A} \tag{3.5}$$

$$\tau_y(H) = \left[\frac{B}{A}((1-H)^{A/2} - 1)\right]^2 \tag{3.6}$$

where μ_p and H is the blood plasma viscosity and fraction haematocrit respectively, values for which are described in section 2.2.2 and displayed in Table 2.2 at normal human levels. The constants A and B represent grouped experimental constants, where $A = a\beta$ and $B = a\alpha_B - 1$ (Cockelet *et al.* 1963). The values of the constants are evaluated according to experimental values for $k_C(H) = 0.003\ Pas$ and $\tau_y(H) = 0.0053\ Pa$, determined for human blood at $H \sim$45 % (Cockelet *et al.* 1963; Merrill *et al.* 1963*b*; Perktold *et al.* 1991). The Casson model was regarded as the best for expressing the relationship between shear stress and shear rate for normal blood in the 1960s. The Casson model is seen to express a valid relationship over a wide range of shear rates, although only greater than 1 s^{-1} (Charm & Kurland 1972; Zydney *et al.* 1991).

3.1.3. *Quemada model*

One of the most recently developed models is that of the Quemada constitutive equation, known to represent the broadest range of shear rates for blood, greater than approximately 0.01 s^{-1} (Zydney *et al.* 1991). It was initially developed to describe the Newtonian viscosity of concentrated particle suspensions, according to the principle of minimum energy dissipation (Quemada 1977);

$$\mu = \mu_p \left(1 - \frac{k(\dot{\gamma}, H)}{2} H\right)^{-2} \tag{3.7}$$

where $k(\dot{\gamma}, H)$ is identified as a non-dimensional, effective, intrinsic viscosity coefficient, a function of the maximum particle packing concentration. μ_p and H are the blood plasma viscosity and fraction haematocrit described earlier for the Casson model. In follow up work by Quemada, the equation was extended to non-Newtonian systems similar to blood. A model was developed for k to incorporate the shear rate dependency on the maximum packing concentration, yielding (Quemada 1978);

$$k(\dot{\gamma}, H) = \frac{k_0 + k_\infty(\dot{\gamma}/\dot{\gamma}_C)^{1/2}}{1 + (\dot{\gamma}/\dot{\gamma}_C)^{1/2}} \tag{3.8}$$

parameters $\dot{\gamma}_C$, k_0 and k_∞ are the critical shear rate and non-dimensional intrinsic viscosities related to low and high shear rates, respectively. Extensive correlations of the above parameters, as a function of haematocrit H, have been developed by Cockelet (1987) as follows;

$$\dot{\gamma}_C = e^{\left(-6.1508 + 27.923H - 25.6H^2 + 3.697H^3\right)} \tag{3.9}$$

$$k_0 = e^{\left(3.874 - 10.41H + 13.8H^2 - 6.738H^3\right)} \tag{3.10}$$

$$k_\infty = e^{\left(1.3435 - 2.803H + 2.711H^2 - 0.6479H^2\right)} \tag{3.11}$$

3.1.4. *Walburn-Schneck model*

In 1976, Walburn and Schneck used a multi-regressional technique to curve fit two power-law model parameters to viscometric data obtained from anti-coagulated blood samples of which the haematocrit and chemical composition was determined. The optimised model includes the complex dependencies on haematocrit and plasma protein concentration. This model represents a statistical correlation of three of the most influential fluid parameters; shear rate, haematocrit and plasma protein concentration (Walburn & Schneck 1976);

$$\mu = C_1 e^{C_2 H} e^{C_4 \frac{TPMA}{H^2}} \dot{\gamma}^{-C_3 H} \tag{3.12}$$

Here the empirical constants are $C_1 = 0.000797\ Pas$, $C_2 = 0.0608$, $C_3 = 0.00499$, $C_4 = 14.585\ l/g$. Haematocrit is defined as a percentage and $TPMA = 25\ g/l$ is the Total Proteins Minus Albumin concentration for normal human blood. The shear rate validity for this model has been reported as being in the broad range greater than approximately $0.01\ s^{-1}$ (Zydney *et al.* 1991).

CHAPTER 4

CFD Models and Methods

The CFD methods used during this work are intended to describe the flow of blood as a multiphase mixture from a continuum perspective, implemeneting finite volume descritization.

4.1. Governing Equations

The governing equations used to model the flow are the incompressible equations for conservation of mass and momentum, commonly known as the incompressible Navier-Stokes equations, including the non-constant density variable to define mixtures;

$$\frac{\partial \rho}{\partial t} + \frac{\partial (\rho u_i)}{\partial x_i} = 0 \tag{4.1}$$

$$\frac{\partial (\rho u_i)}{\partial t} + u_j \frac{\partial (\rho u_i)}{\partial x_j} = -\frac{\partial p}{\partial x_i} + \frac{\partial \tau_{ij}}{\partial x_j} + \rho f_i \tag{4.2}$$

where ρ is the density, u_i is the velocity component in i-direction, p is the static pressure, τ_{ij} is the viscous stress tensor and f_i represents the possibility of any external body force acting on the fluid (e.g. gravity). A derivation for the conservation equation forms can be found in Anderson (1995). The viscous stress tensor, τ_{ij}, accounts for the stress due to the fluid motion, given by

$$\tau_{ij} = 2\mu(S_{ij}) \tag{4.3}$$

where μ respresents the dynamic viscosity, a function of temperature for Newtonian fluids or a multi-variable dependency for non-Newtonian fluids or mixtures as considered here. Considered variables are the shear rate, $\dot{gamma}$, and local RBC phase fraction, H. The non-Newtonian viscosity models are described in Section 3.1, where stress due to fluid motion is not simply a linear function of the shear rate. The shear rate is obtained from the rate of shear tensor, S_{ij}, defined as found for Netwonian fluids;

$$S_{ij} = \frac{1}{2}\left(\frac{\partial u_i}{\partial x_j} + \frac{\partial u_j}{\partial x_i}\right) \tag{4.4}$$

The forms of equations 4.1 and 4.2 maintains the influence of density on the left handside, demonstrating the considerations of density variations when modelling multiphase liquid mixtures. The mixtures considered here are assumed to be almost homogeneous, since the difference in RBC and plasma density is small. Thus, the density is as assumed to be constant and all external forces are neglected whereby 4.1 and 4.2 reduce to the following;

$$\frac{\partial u_i}{\partial x_i} = 0 \tag{4.5}$$

$$\frac{\partial u_i}{\partial t} + u_j \frac{\partial (u_i)}{\partial x_j} = \frac{1}{\rho}\left[-\frac{\partial p}{\partial x_i} + \frac{\partial \tau_{ij}}{\partial x_j}\right] \tag{4.6}$$

The RBCs are relatively stiff and in larger vessels they can be considered to be solid. The cells have a density close to that of the plasma and for simplicity this fact is neglected. The forces that act on the RBCs include the drag, lift, electrostatic forces and collisions among cells. We assume that all these forces can be modelled by an equivalent diffusivity of mass (assuming a Fickian relation). With these assumptions, the motion of the RBCs is determined by a typical conservation relation with convection by the fluid flow and diffusion by a concentration gradient. In the future we intend to examine the validity of these assumptions for the high RBC concentration found in the blood.

$$\frac{\partial (H)}{\partial t} + u_j \frac{\partial (H)}{\partial x_j} = D_H \frac{\partial^2 H}{\partial x_j \partial x_j} \tag{4.7}$$

where H is the local volume fraction of the mixture species or phase and D_H is the effective mass diffusivity co-efficient thereof.

4.2. Numerical Methods

The solution of the non-linear partial differential governing equations of the flow, namely the Navier-Stokes equations, is not trivial. The progress of the computational age now allows the study of non-linear flow field characteristics at an ever increasing level of complexity. The equations are discretized into a set of non-linear algebraic equations and solved iteratively. The governing equations are discretized as described in the following paragraphs.

This section describes the numerical methods implemented for discretization of space, time and the governing equations. The finite volume method implemented in OpenFOAM-1.6 is used for all numerical simulation data presented in this thesis.

4.2.1. *Spatial Discretization*

We use unstructured grids consisting of non-orthogonal hexhedral cells to discretize the governing equations. The computational cost is increased as compared to structured grids but better suited to complex geometries and adaptive mesh refinement in achieving a satisfactory level of accuracy. The discretization, equivalent to the Central Difference Scheme (CDS) on a Cartesian grid, is used to spatially discretize the variables, thereby rendering the accuracy to second order. Two schemes, CDS and Quadratic Upwind Interpolation (QUICK), are compared in our accuracy studies. A previous study offers comparable data but through the implementation of a different solver, Fluent 3.6. Therefore a comparison study was carried out to ensure the quality of the results. The two schemes mentioned above are described below.

4.2.1a. *Central Difference Scheme (CDS).* The central difference scheme is the simplest and most widely used. The discretization of the equations requires that values of the variables are approximated at control volume (CV) face centres, as well as

grid nodes. Therefore the scheme performs linear interpolation between the two nearest nodes, leading to second order accuracy on uniform grids. On non-uniform grids the scheme performs in a similar manner yielding a second order approximation as long as the grid is fine enough (asymptotic convergence is achieved), the computational grid is not too skewed and the grid-spacing gradients are not too large. These conditions apply to any discretization if one wants to avoid degradation of the order of approximation. It "offers a good compromise among accuracy, simplicity and efficieny"(Ferziger & Perić 1999).

4.2.1b. *Quadratic Upwind Interpolation (QUICK).* The interpolation scheme is fully named the Quadratic Upwind Interpolation for Convective Kinematics (QUICK) and has a formal third order accuracy on uniform grids. It extends the interpolation by one more node in every dimension upstream, to construct a parabola rather than the straight line characteristic of CDS. However, both QUICK and CDS converge asymptotically with a second order behaviour and "differences are rarely large"according to Ferziger & Perić (1999). In certain cases where the CDS produces oscillatory behaviour the QUICK scheme will offer a compromise between stability and accuracy. Leonard (1979)

4.2.2. *Temporal Discretization*

Temporal discretization is carried out via the unconditionally stable second order backward implicit scheme. The Courant Friedrichs Levy (CFL) condition is maintained, where no physical information is allowed to propagate further than one grid cell during a single time-step.

4.2.3. *Computational Domain and Boundary Conditions*

The geometry is a simplified 90-degree arterial branch or bifurcation shown in Figure 4.1, depicting the distinguishing features and dimensions important to the study. The junction region has a curved intersection that is characteristic of the larger vessels *in-vivo*. As stated in spatial discretization, the grid is constructed of an unstructured hexahedral cell set. An O-grid is used to define orthogonality at the walls of the tubes and the radius of curvature, R=9.7 mm, defining the intersection of the main and daughter branches of diameters 13.2 and 9.375 mm, respectively. Cells are progressively finer towards the walls to ensure resolution of the boundary layer. The mesh properties are displayed in Figure 4.1. Care is also taken to maintain a high enough resolution in the core of the daughter branch to capture the gradients in the mass transport equation, Equation 4.7.

The domain used during this this, D2, is an extended version of that used in a previous study by Evegren *et al.* (2010), D1. The extension is made along with a simplification of the cell structure from a hybrid cell (hexahedra and tetrahedra) type to the pure hexahedral type. The main reason for the extension is to remove the influence of the outlets on the field values defined by the mass transport equation in the regions of interest near the bifurcation. The advantages of changing the cell type to a pure hexahedral structure is that it is easier to control a more uniform mesh density where needed, along with the ease of high quality refinement when needed. A detailed comparative grid study is carried out to ensure that accuracy is maintained when grid cell structure, domain extents and the solver is changed. The

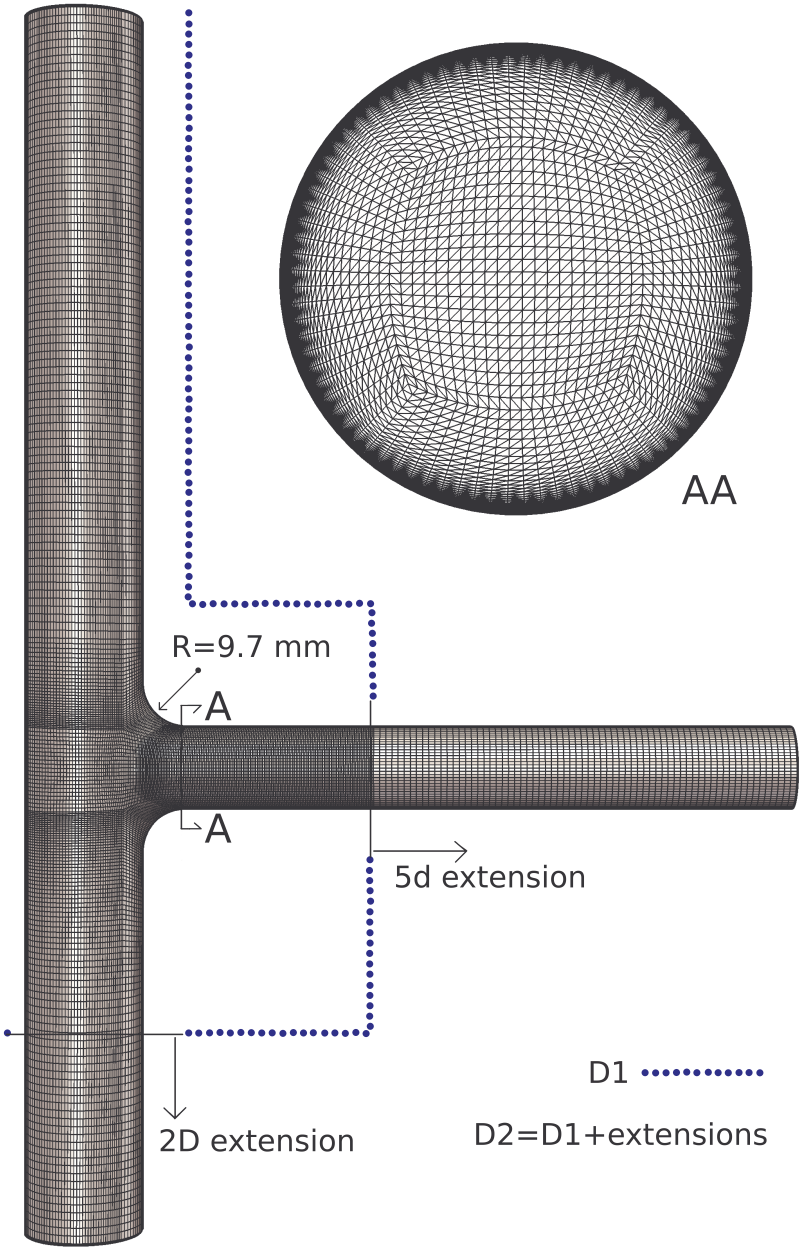

FIGURE 4.1. The 90-degree bifurcation geometry, displaying geometric features, domain extensions and cell distribution of the numerical grid.

results are displayed in the Results section. Figure 4.1 displays the two domains, D1 and D2, considered during the grid study.

Common boundary conditions are implemented throughout the study. The no-slip condition is set at the walls. At the outlets constant pressure is set while the zero gradient condition is set for the scalar transport equation. The zero gradient condition is also set at the walls for the scalar transport equation since the haematocrit never diffuses across the arterial walls.

The inflow conditions are described by a time dependent axial velocity profile and vanishing cross-flow velocity components. The representing the periodic pulsating character of the flow in the vascular network, implemented in previous, comparative work by Evegren *et al.* (2010). The haematocrit distribution at the inlet is defined according to observations from experimental work by Aarts *et al.* (1988). A similar equation applied to the inlet, describing this observed average distribution, was first implemented by Hund & Antaki (2009).

4.3. Solution Procedure and Case Setups

The flow field is defined through Equations (4.5)-(4.6). and solved via a hybrid transient incompressible solver (OpenFOAM solver pimpleFoam) implementing the PISO algorithm for pressure-velocity coupling. The velocity field is coupled to the scalar transport Equation 4.7, defining the advection of haematocrit. The distribution of the scalar (the haematocrit) is considered passive i.e. not coupled back and hence not influencing the flow field itself. A single flow rate with three different heart pulsation frequencies are studied, as given in Table 4.1. Reynolds and Womersley numbers are based on Newtonian viscosity value for blood take to be 3.5 times that of water.

The first phase of the study, results are described in Paper 1, focuses on the transport behavioural differences of haematocrit between non-Newtonian and Newtonian viscosity models.

TABLE 4.1. Case set up parameters for the Uncoupled simulations. Peak inflow velocity, heart beats per minute (BPM), max (Re) and max (α).

	Peak Inlet Velocity (m/s)	BPM	Re max	α max
case 1	0.11	30	440	6.5
case 2	0.11	60	440	9
case 3	0.11	90	440	11

During the follow up phases of the work, the scalar or haematocrit distribution is coupled back to the non-Newtonian viscosity models, implying a two-way interaction between the RBC transport equation, Equation 4.7, and the governing equations of the flow, Equations (4.5)-(4.6). A more complete model of the blood-like viscosity is obtained by utilizing the local haematocrit and shear-rate. The equations are solved in the same manner as described earlier, except that the local RBC concentration is coupled to the viscosity models, described in Section 3.1.

The effect of varying inflow rate, inlet haematocrit distribution and heart pulsation frequency are considered, displayed in Table 4.2. Wall Shear stress variations, pump work and haematocrit distribution variation are related to the non-Newtonian characteristics.

TABLE 4.2. Case set up parameters for the coupled simulations. Peak inflow velocity, heart beats per minute (BPM), Reynolds Re_p and Womersley (α_p) numbers with respect to Blood Plasma (p).

	Peak Inlet Velocity (m/s)	BPM	Re_p	α_p
case 1	0.11	60	1130	14.6
case 2	0.11	90	1130	18.2
case 3	0.22	60	2260	14.6

The simulations for all cases are run on clusters for up to 18 pulsation periods before data is acquired, taking up to 2 days per pulsation period. The numerical accuracy of the optimized grid is considered regarding the acquired variables of interest and is presented in a section below.

CHAPTER 5

Summary of Results

In this chapter we describe the assessment of the numerical accuracy as well as a short summary of the results, that are presented in more detail in the enclosed papers.

5.1. Numerical Accuracy

5.1.1. *Steady flow*

For assessing the accuracy of the numerical results, the grid type and its resolution is changed along with an extension of the domain at the outlets. Even though care was taken in maintaining comparable resolution in the change of cell structure and domain extents it is desired to confirm agreement of results. Since the solver used here is different from the one used in a previous study by Evegren *et al.* (2010), a comparison between the results is required. Table 5.1 shows the grid study matrix, where the average grid element size is:

$$h = \sqrt[3]{\frac{\sum_{i=1}^{n_{cells}} V_i}{n_{cells}}} \tag{5.1}$$

where V_i is the individual grid cell volume, summed up with all other cells to define the domain volume, n_{cells} is the number of grid cells. The domains considered are denoted with reference to Figure 4.1 in Section 4.2.3. If the grid element size refinement ratio is quoted for a grid, the subscript indicates which base grid it is a hexahedral refinement of. The inflow velocity condition used is a common function used in the previous study by Evegren *et al.* (2010), and the shear viscosity (μ) implemented is a value commonly used to define blood as a Newtonian fluid, 3.5 times higher than water. Velocity gradients in the steady flow case, in the region of the bifurcation, are higher than that in the pulsatile case due to fully developed flow.

The accuracy of the velocity plots extracted from the highest gradient regions in the daughter branch, representing parallel and normal components, is defined by an RMS error Equation 5.2. Here, the ϕ represents the variable or property and n is the number of samples.

$$Error = \frac{\sqrt{\frac{\sum_{i=1}^{n}(\phi_{1,i} - \phi_{2,i})^2}{n}}}{(\phi_{1,2,max} - \phi_{1,2,min})} \tag{5.2}$$

Figure 5.1 shows the absolute velocity plots for cases A, B and C at the axial position, x/d =0.5 in the daughter branch where the gradients are found to be the greatest. The axial component (along direction of bulk flow) and the major normal

TABLE 5.1. The steady flow grid study matrix considering the original and extended domains

	Domain	***Solver***	***Grid cell type***	***Grid cell size*** (n_{cells})	***Average grid element size*** (h, mm)	***Grid element size refinement ratio*** ($r_{BA} = \frac{h_B}{h_A}$)
case A	D1	Ansys-Fluent	Hybrid	918,282	0.264	-
case B	D1	OpenFOAM-1.6	Hybrid	918,282	0.264	-
case C	D1	OpenFOAM-1.6	Hexa-hedral	919,851	0.264	-
case D	D1	OpenFOAM-1.6	Hybrid	3,722,559	0.166	$r_{DB} = 1.59$
case E	D1	OpenFOAM-1.6	Hexa-hedral	3,700,909	0.166	$r_{EC} = 1.59$
case F	D2	OpenFOAM-1.6	Hexa-hedral	475,179	0.329	-
case G	D2	OpenFOAM-1.6	Hexa-hedral	1,410,945	0.229	$r_{GF} = 1.44$
case H	D2	OpenFOAM-1.6	Hexa-hedral	4,818,447	0.152	$r_{HG} = 1.51$

component (y-axis) of the flow are compared. The differences observed between cases A and B represent the change in discretization and the change in grid type by cases B and C. The axial component shows little difference between cases A, B and C, with an error of less than 1 %. However, the y-axis or secondary flow component displays more interesting discrepancies. There is approximately a 1 % difference between cases A and B, but approximately a 5 % difference between B and C. This shows that there is a greater sensitivity to the change in mesh compared to a change in solver. This may be related to a lack of resolution when creating a hexahedral mesh of equilavent density characteristics. The further local hexahedral refinements carried out for cases B and C in the region of interest of the daughter branch, yielding cases D and E respectively. The purpose is to ensure that grid resolution is not the reason for the discrepency.

Figure 5.2 shows the comparison of between cases B and D, and cases C and E, respectively. Both plots show that lack of resolution is not the problem. The refinements only lead to a difference of approximately 0.5 % or less in both comparisons. Instead this shows that the sensitivity is associated with the change in grid type and that the pure hexahedral grid size of 919,851 cells produces accurate results.

The grid extension is therefore carried out yielding case G of grid size of 1,410,945 cells. Local coarsening and refinement of case G, defining cases F and H,

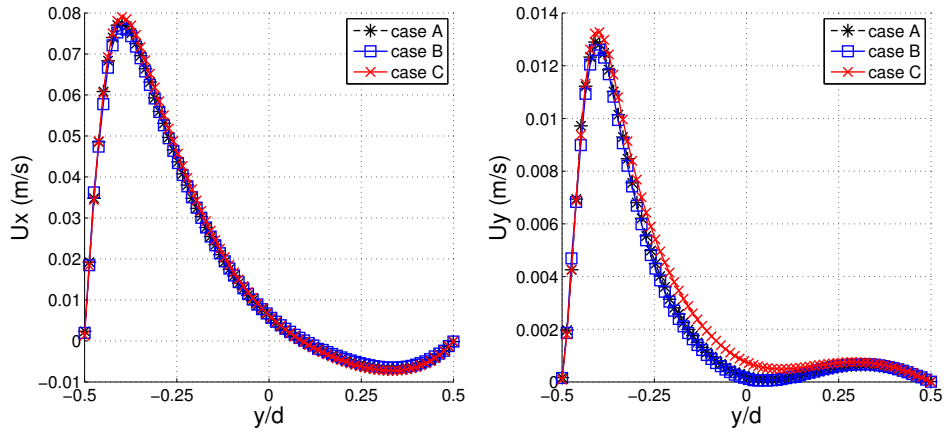

FIGURE 5.1. Comparative cross-sectional velocity data in the y-direction for Cases A, B and C in the daughter branch at x/d =0.5; (left) Axial (x-component) and (right) secondary (y-component) components.

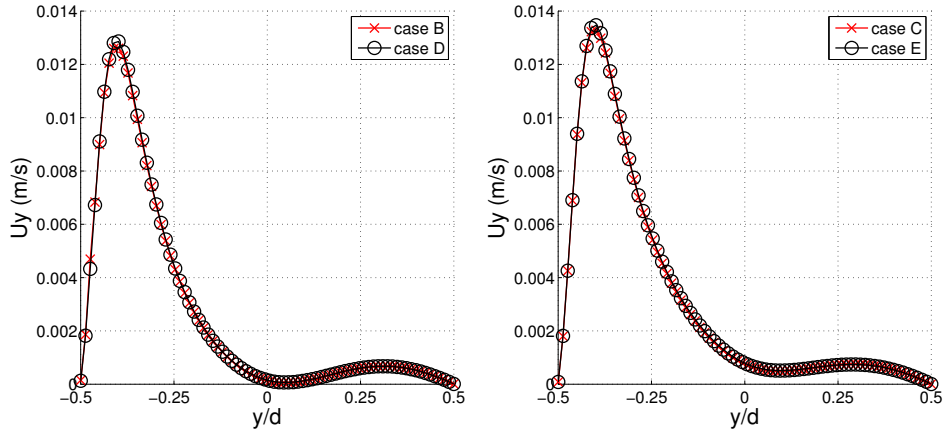

FIGURE 5.2. Comparison between; (left) hybrid grid refinement, cases B and D, and (right) hexahedral grid refinement, cases C and E, for the sensitive secondary (y-component) velocity component at axial cross-section x/d =0.5.

respectively, was carried out to check that sufficient grid resolution is maintained given the domain extension. The comparison of the secondary component, previously shown to be the most sensitive to grid density, is displayed in Figure 5.3 at axial cross-sectional positions of x/d =0.5 and 1.5. Case F shows under prediction of the velocity at the peak for position x/d =0.5 and oscillatory under prediction at mid channel for position x/d =1.5. Small differences of approximately 0.5 % exist between cases G and H at both axial positions, with a smooth definition of secondary velocity components.

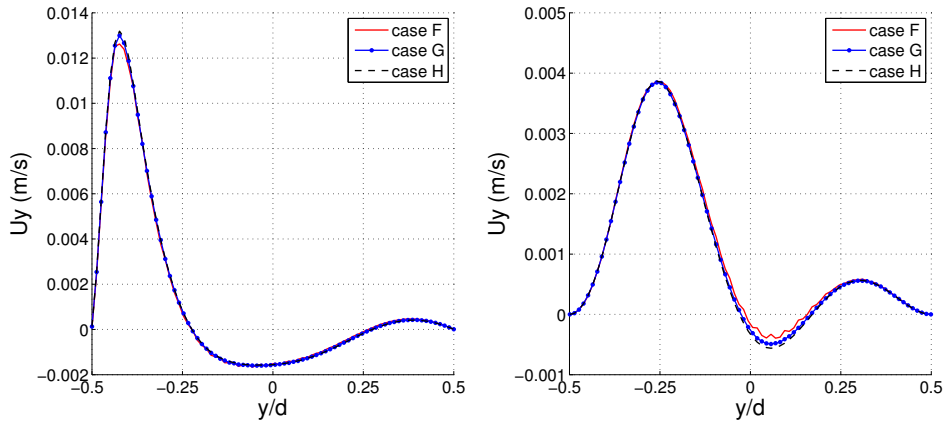

FIGURE 5.3. Comparison of secondary velocity components (y-component) in the y-direction for cases F, G and H in the daughter branch at positions x/d =0.5 and 1.5.

5.1.2. *Unsteady WSS comparison*

A comparison was performed between the pulsatile wall shear stress characteristics obtained by the two solvers considered in this study. Cases A and B from Table 5.1 are re-simulated with pulsatile inflow properties replicating a case from which the current geometry is based upon. "Case 2"from the study by Evegren *et al.* (2010) is replicated in OpenFOAM-1.6, using water as the fluid. Figure 5.4 displays the temporal comparison between regions of negative WSS for cases A and B, at similar times. The figures show that the flows are almost identical in-spite of the differences in grid type, resolution and discretization schemes. Figure 5.5 also shows that the WSS magnitudes and contours are similar in both the axial and radial components.

Figure 5.5 displays that there are slight changes in the WSS magnitudes at 180○, with the solver used in the current study yields a slightly higher peak. However the negative WSS stress regions at 0 and 360° closer to the bifurcation at x/d=0.5, corresponded well with the magnitudes and profiles, reflected throughtout the pulsation cycle.

The different solvers show similar flow characteristics and with acceptable accuracy.

5.2. Paper 1

The internal haemodilution in large arterial bifurcations, such as the renal abdominal aortic branch, may imply significant variations in important physiological parameters. The complex viscous behaviour of blood strongly influences the haemodynamic conditions that are important in understanding the development of atherosclerosis. This is due to the viscosity of blood being directly dependent on the RBC concentration. The extent of haemodilution in large 90-degree bifurcations has not been considered in the past. This study aims to quantify possible bulk changes in RBC concentration due to varying haemodynamic conditions. There is uncertainty regarding RBC distribution in arterial flows, especially in the near wall region. Sensitivity to unknown RBC properties such as inlet distribution profiles

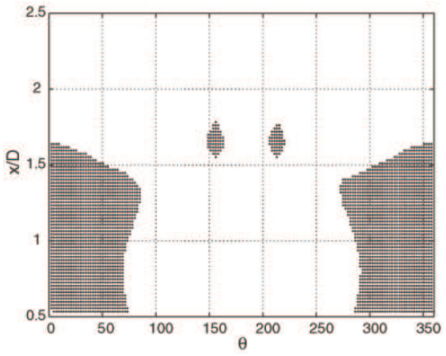

(t/T=0.274 from Evegren *et al.* (2010))

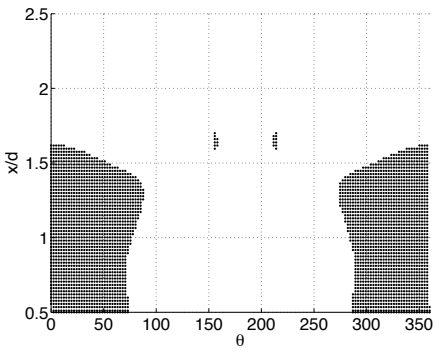

(t/T=0.274 *Current study)

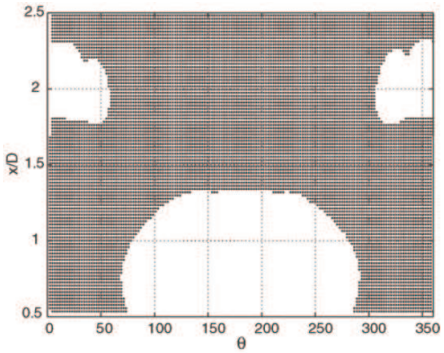

(t/T=0.280 from Evegren *et al.* (2010))

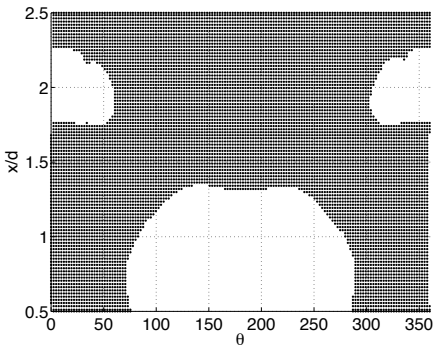

(t/T=0.280 *Current study)

FIGURE 5.4. A comparison between areas of negative axial WSS (backflow) at two points in time between the study by (left) Evegren *et al.* (2010) and the (right) current study. The figure shows the surface of the branch pipe near the bifurcation. The distance from the bifurcation is given by x/d and the pipe azimuthal angle by θ.

and mass diffusivity are considered. The range of RBC mass diffusivity is determined by a range of Schmidt numbers (Sc) relative to the viscosity of water. Bulk RBCs are defined as a fluid soluble in water.

The relative importance of RBC transport by non-Newtonian and Newtonian viscosity definitions of physiological flows is the main focus. Pulsatile frequency defined by a range of heart pulsation rates is the most dominant parameter when studying inherent flow unsteadiness. The unsteadiness is found to play an important role in haemodilution, determined by the extent of development of secondary flows. At an Sc number greater than 11, advection already starts to dominate and significant internal haemodilution exists for both Newtonian and non-Newtonian viscosity models, due to shear. Haemodilution is enhanced nearer the bifurcation due to centrifugal effects and the forming of a separation bubble. As the heart pulstaion frequency increases, so the dilution becomes more consistently large, with a smaller deviation near peak systole. Large differences in dilution between the non-Newtonian models and a Newtonian model (water) are also found, indicating that

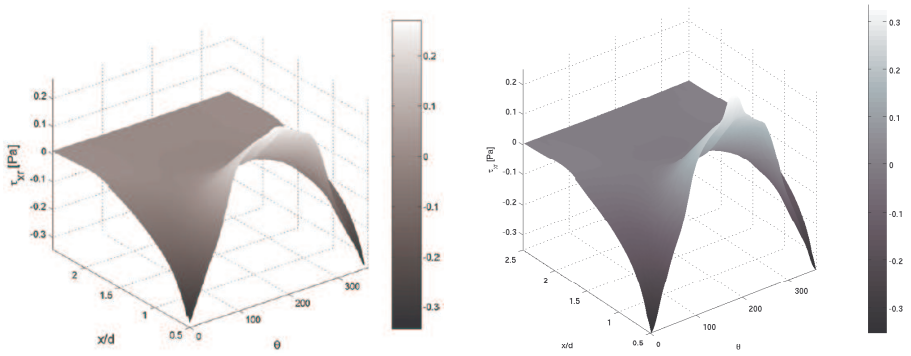

(t/T=0.278 from Evegren *et al.* (2010)) (t/T=0.278 *Current study)

FIGURE 5.5. A comparison of WSS magnitudes and contours at a specified point in time, t/T=0.278, between the study by (left) Evegren *et al.* (2010) and the (right) current study.

non-Newtonian flow shear effects are important. The results show that there are variations in internal haemodilution, due to haemodynamic unsteadiness, that may have a relevant impact to physiological parameters such as WSS, when coupling the local RBC concentration back to the viscosity models.

5.3. Paper 2

Flow unsteadiness and low time-averaged and oscillating WSS are influential features of the flow in 90-degree arterial bifurcations, regarding atherogenesis. The importance of the character of the blood being non-Newtonian has been disputed in previous numerical studies. In recent years advancements have been made in the understanding of the complex physiological and biochemical processes. In previous studies it has been shown that fluid mechanical forces, specifically temporal WSSGs, could play an important role *in-vivo* to the structural and chemical response of the endothelium. During this study, the importance of blood-like non-Newtonian viscosity on physiological parameters is considered. This encompasses the effect of RBC dilution and the implications to WSS variations.

Further evidence is provided for WSS variations previously correlated with the diseased regions of the larger arteries. The effects of the blood-like non-Newtonian viscosity models in the progression of separated and secondary flows in the region of the bifurcation is important. The regions of reversed flow are shown to be more focal to the bifurcation in disease correlated area. The RBC volume fraction dependency on non-Newtonian viscosity models is important for the magnitudes of the WSS gradients and their magnitude. High temporal WSS gradients (WSSG) follow a stagnation point that moves with the development of the separation bubble during the heart pulsation cycle. This elevated temporal gradient is due to the shear-thinning property of the non-Newtonian viscosity, the magnitude of which is dependent on the RBC volume fraction near the wall. The focal nature of the gradient has direct implications with respect to the response of the endothelium.

CHAPTER 6

Conclusions

In this work the influence of RBC concentration on the haemodynamic conditions in the region of arterial bifurcations has been investigated. The geometry represents similar arterial bifurcations existing in the aorta. Physiological parameters, such as WSS, important for the understanding of atherogenesis are studied, regarding variations in flow rate and heart pulsation frequency. Sensitivity to the inlet RBC distribution and intrinsic mass diffusivity are also considered. Conclusions from this study are:

- Variations in the RBC concentration exists near bifurcations in the larger arterial networks.

- Both non-Newtonian and Newtonian shear viscosity models of the flow show clear RBC dilution effects due to shear. The formation of the separation bubble in the daughter branch is the main fluid mechanical feature responsible for enhancement of dilution.

- The inflow conditions are important in defining the extent of formation of the separation bubble. The inherent unsteadiness in the heart cycle is the most dominant inflow condition and defines more frequent changes in RBC concentration or dilution, with increased pulsation frequency. This in turn means more frequent and complex changes in viscosity, implying complex variations in an important physiological parameter such as WSS.

- There are large differences in RBC dilution as computed by the non-Newtonian models, relative to the Newtonian model. This implies that there are variations in viscosity that need to be considered in the region of bifurcations, when studying dependent physiological parameters important to athergenesis.

- Regions of separated and reversed flows, related to atherogenesis, are more closely focused to the bifurcation under blood-like non-Newtonian flow conditions than under Newtonian conditions. This may imply that Newtonian models inaccurately determined regions of separated, unsteady flows near the bifurcation in disease correlated regions.

- The RBC volume fraction dependency on the implemented non-Newtonian viscosity models is important in determining the magnitudes of the wall shear stress and the its gradients, due to dilution. The effect of dilution has a strong influence on the unsteadiness of the WSS and the flow inside the separation bubble. This may imply modified transport of atherogenic

substances in the region of bifurcations, otherwise damped by conventional, excessively viscous non-Newtonian modelling.

- High temporal WSS gradients follow a stagnation point that moves with the development of the separation bubble during the heart pulsation cycle. This elevated temporal gradient is due to the shear-thinning property of the non-Newtonian viscosity, the magnitude of which is dependent on the RBC volume fraction near the wall. The focal nature of the gradient has direct implications with respect to the response of the endothelium, mechnically and biochemically.

CHAPTER 7

Future Work

In the work following we will consider the density variations due to RBC dilution. This will be accomplished through a two-phase Euler-Euler miscible liquid solver in OpenFOAM, integrating the non-Newtonian viscosity models. This will include considering the two phases as Newtonian fluids and studying the different possible viscosity values of the RBC phase, relative to plasma. The viscosity of the aqueous fluid contained by RBCs is variable, depending on the concentration of haemoglobin, and is one of the factors defining the bulk fluid viscosity. Analysis of the flow field characteristics, pressure losses and WSS variations will be made. Particular interest lies in the effects of non-Newtonian blood behaviour on the secondary flow characteristics. The difference in the flow characteristics may also possibly be a factor in the near wall transport of atherogenic materials in addition to its effect on the WSS.

Furthermore, the methodology may be applied to multiple bifurcating domains, where the characteristics of the flow field and RBC distribution phenomena will be studied. Again, the effects of flow rate and pulsation frequency and sensitivity to the inlet velocity profile, will also be studied. The non-rigidity of the arterial wall will not be considered, since the rheological properties of the fluid are the main focus.

Blood is a dense suspension of cells, dominated by RBCs, where complex intrinsic properties due to shear are not well quantified or understood. Few definitive studies exist regarding relations for mass diffusivity and distributions of RBCs in large arterial flows. The objective is to explicitly compute the rheological properties of the flow of water containing RBC like particles at high concentration. We shall use an existing Lattice Boltzmann method (combined with an immersed boundary like approach for handling the RBC). Initial tests include a channel flow of a fluid containing about 7% RBC shaped particles. Future calculations shall handle pipe flows with varying RBC concentrations and varying pulsation rate (from 0 to physiological values). An extension to charged particles shall also be considered. The computations shall be used to compute constitutive relations for the suspension viscosity.

Acknowledgements

Firstly, I would like to thank my supervisors Professor Laszlo Fuchs and Doctor Lisa Prahl-Wittberg for their help, support and tolerance. Thank for always having your doors open for adhoc discussions and guidance.

The financial support of Vetenskapsrådet is greatly appreciated. The computing resources were supplied by the Swedish National Infrastructure for Computing (SNIC) and the HPC clusters; High Performance Computing Center North (HPC2N) and National Supercomputer Centre in Linkping (NSC).

To my office comrades. The developmental as well as casual discussions induce a relaxing atmosphere at the office. Thank you very much for all the good company, humour and support; Feng Zhang, Bernhard Semlitsch, Yue Wang and Aleksander Pasieczny. Thank you very much to the close research group Dr. Mireia Altimira, Dr. Anders Dahlkild, Dr. Mihai Mihaescu, Dr. Etienne Robert, Martin Sder, Olle Bodin, Johan Fjllman, Karl Hkansson, Mathias Kvick, Emma Alenius, Alexander Sakowitz, Markus Pastuhoff, Sissy Kalpakli, Dr. Niklas Winkler for the friendly support and questioning. Furthermore, I would also like to thank Carolina Eneqvist, Heide Hornk, Hans Silverhag, Malin Lundin, Karina Bellbrant, Stefan Skult and Pr Ekstrand for offering immediate administrative assistance whenever required. The weekly departmental and personal fikas are always pleasant experiences. Thank you for the friendly chats during all the occasions we meet, Lailai Zhu, Joy Klinkenberg, Amin Rasam, Zeinab Pouransari, Dr. Minh Do-Quang, Dr. Geert Brethouwer, Florian Stillfried, Andreas Vallgren, Krishnagoud Manda, Marit Berger, Amer Malik, Johan Malm, David Tempelmann, Natalia Kosterina, Qiang Li and everyone else.

I would like to thank my mother, father and brother for always being there for me. I respect you all for the fights that you put up in the last two years to survive. Finally, I would like to honour my loyal, ever loving fiancée, Ellinor Elowsson, who always puts life into perspective when I need it most. Thank you for supporting me.

References

Aarts, P., Van Den Broek, S., Prins, G., Kuiken, G., Sixma, J. & Heethaar, R. 1988 Blood platelets are concentrated near the wall and red blood cells, in the center in flowing blood. *Arteriosclerosis, Thrombosis, and Vascular Biology* **8** (6), 819.

Anderson, J. D. 1995 *Computational Fluid Dynamics: The Basics with Applications*. McGraw-Hill: Mechanical Engineering Series.

Bakhru, A. & Erlinger, T. 2005 Smoking cessation and cardiovascular disease risk factors: results from the third national health and nutrition examination survey. *PLoS medicine* **2** (6), e160.

Barnes, H. 1995 A review of the slip (wall depletion) of polymer solutions, emulsions and particle suspensions in viscometers: its cause, character, and cure. *Journal of Non-Newtonian Fluid Mechanics* **56** (3), 221–251.

Barnes, H. 2000 Measuring the viscosity of large-particle (and flocculated) suspensions–a note on the necessary gap size of rotational viscometers. *Journal of non-newtonian fluid mechanics* **94** (2-3), 213–217.

Bharadvaj, B., Mabon, R. & Giddens, D. 1982*a* Steady flow in a model of the human carotid bifurcation. part i–flow visualization. *Journal of Biomechanics* **15** (5), 349–362.

Bharadvaj, B., Mabon, R. & Giddens, D. 1982*b* Steady flow in a model of the human carotid bifurcation. part ii–laser-doppler anemometer measurements. *Journal of Biomechanics* **15** (5), 363–365.

Birchall, D., Zaman, A., Hacker, J., Davies, G. & Mendelow, D. 2006 Analysis of haemodynamic disturbance in the atherosclerotic carotid artery using computational fluid dynamics. *European radiology* **16** (5), 1074–1083.

Bishop, J., Popel, A., Intaglietta, M. & Johnson, P. 2002 Effect of aggregation and shear rate on the dispersion of red blood cells flowing in venules. *American Journal of Physiology-Heart and Circulatory Physiology* **283** (5), H1985.

Bronzino, J., ed. 2000 *The Biomedical Engineering Handbook, second edition*. Boca Raton: CRC Press LLC.

Brooks, D., Goodwin, J. & Seaman, G. 1970 Interactions among erythrocytes under shear. *Journal of applied physiology* **28** (2), 172.

Burton, A. 1965 Physiology and biophysics of the circulation. *Academic Medicine* **40** (8).

Caro, C. 1966 The dispersion of indicator flowing through simplified models of the circulation and its relevance to velocity profile in blood vessels. *The Journal of Physiology* **185** (3), 501.

Caro, C. 2009 Discovery of the role of wall shear in atherosclerosis. *Arteriosclerosis, thrombosis, and vascular biology* **29** (2), 158.

Caro, C., Fitz-Gerald, J. & Schroter, R. 1969 Arterial wall shear and distribution of early atheroma in man. *Nature Publishing Group* .

Caro, C., Fitz-Gerald, J. & Schroter, R. 1971 Atheroma and arterial wall shear observation, correlation and proposal of a shear dependent mass transfer mechanism for atherogenesis. *Proceedings of the Royal Society of London. Series B. Biological Sciences* **177** (1046), 109.

Caro, C. & Lighthill, M. 1966 Velocity distribution in models of the circulation measured by indicator dispersion. *J Physiol* **183**, 34.

Caro, C., Pedley, T., Schroter, R. & Seed, W. 1978 *The mechanics of the circulation*. Oxford University Press New York.

Carreau, P. 1972 Rheological equations from molecular network theories. *Journal of Rheology* **16**, 99–127.

Casson, N. 1959 *Rheology of disperse systems*. Pergamon Press, London.

Cha, W. & Beissinger, R. 2001 Evaluation of shear-induced particle diffusivity in red cell ghosts suspensions. *Korean Journal of Chemical Engineering* **18** (4), 479–485.

Charm, S. & Kurland, G. 1972 Blood rheology. *Cardiovascular fluid dynamics* **2**.

Charm, S. & Kurland, G. 1974 *Blood flow and microcirculation*, , vol. 14. John Wiley and Sons, Inc.

Chien, S. 1970 Shear dependence of effective cell volume as a determinant of blood viscosity. *Science* **168** (3934), 977.

Chien, S., Usami, S., Taylor, H., Lundberg, J. & Gregersen, M. 1966 Effects of hematocrit and plasma proteins on human blood rheology at low shear rates. *Journal of Applied Physiology* **21** (1), 81.

Cockelet, G. 1987 The rheology and tube flow of blood. *Handbook of Bioengineering* p. 14.

Cockelet, G., Merrill, E., Gilliland, E., Shin, H., Britten, A. & Wells Jr, R. 1963 The rheology of human blood–measurement near and at zero shear rate. *Journal of Rheology* **7**, 303–307.

Cohen, E. & De Schepper, I. 1992 Transport properties of concentrated colloidal suspensions. *AIP Conference Proceedings* **256**, 359.

Copley, A., Luchini, B. & Whelan, E. 1968 On the role of fibrinogen-fibrin complexes in flow properties and suspension-stability of blood systems. In *Hemorheology. Proc. First Internat. Conf. University of Iceland, Reykjavik, 10–16 July 1966*, p. 375. Pergamon Press, Oxford, New York.

Cross, M. 1965 Rheology of non-newtonian fluids: a new flow equation for pseudoplastic systems. *Journal of Colloid Science* **20** (5), 417–437.

Cross, M. 1970 Kinetic interpretation of non-newtonian flow. *Journal of Colloid and Interface Science* **33** (1), 30–35.

Cutnell, J. & Johnson, K. 1998 *Physics, 8th Edition*. Wiley.

DeBakey, M., Lawrie, G. & Glaeser, D. 1985 Patterns of atherosclerosis and their surgical significance. *Annals of surgery* **201** (2), 132.

DePaola, N., Gimbrone, M., Davies, P. & Dewey, C. 1992 Vascular endothelium responds to fluid shear stress gradients. *Arteriosclerosis, Thrombosis, and Vascular Biology* **12** (11), 1254–1257.

Dintenfass, L. 1968*a* Blood viscosity internal fluidity of the red cell, dynamic coagulation and the critical capillary radius as factors in physiology and pathology or circulation and microcirculation. *The Medical journal of Australia* **1** (16), 688.

Dintenfass, L. 1968*b* Internal viscosity of the red cell and a blood viscosity equation. *Nature Publishing Group* **219**, 956–958.

Duguid, J. & Robertson, W. 1957 Mechanical factors in atherosclerosis. *Lancet* **272** (6981), 1205.

Evegren, P., Fuchs, L. & Revstedt, J. 2010 Wall shear stress variations in a 90-degree bifurcation in 3d pulsating flows. *Medical engineering & physics* **32** (2), 189–202.

Farmakis, T., Soulis, J., Giannoglou, G., Zioupos, G. & Louridas, G. 2004 Wall shear stress gradient topography in the normal left coronary arterial tree: possible implications for atherogenesis. *Current Medical Research and Opinion®* **20** (5), 587–596.

Farmer, J. & Gotto, A. 1997 *Dyslipidemia and other risk factors for coronary artery disease. u: Braunwald E. i dr.(ur.) Heart disease: A textbook of cardiovascular medicine*. Philadelphia, itd: WB Saunders.

Ferdowsian, H. & Barnard, N. 2009 Effects of plant-based diets on plasma lipids. *The American journal of cardiology* **104** (7), 947–956.

Ferziger, J. & Perić, M. 1999 *Computational methods for fluid dynamics*, , vol. 2. Springer Berlin.

Friedman, M., Deters, O., Bargeron, C., Hutchins, G. & Mark, F. 1986 Shear-dependent thickening of the human arterial intima. *Atherosclerosis* **60** (2), 161–171.

Friedman, M., Deters, O., Mark, F., Brent Bargeron, C. & Hutchins, G. 1983 Arterial geometry affects hemodynamics: A potential risk factor for atherosclerosis. *Atherosclerosis* **46** (2), 225–231.

Friedman, M., Hutchins, G., Brent Bargeron, C., Deters, O. & Mark, F. 1981 Correlation between intimal thickness and fluid shear in human arteries. *Atherosclerosis* **39** (3), 425–436.

Friedman, M., O'Brien, V. & Ehrlich, L. 1975 Calculations of pulsatile flow through a branch: implications for the hemodynamics of atherogenesis. *Circulation Research* **36** (2), 277.

Fry, D. 1968 Acute vascular endothelial changes associated with increased blood velocity gradients. *Circulation Research* **22** (2), 165.

Gambillara, V., Montorzi, G., Haziza-Pigeon, C., Stergiopulos, N. & Silacci, P. 2005 Arterial wall response to ex vivo exposure to oscillatory shear stress. *Journal of vascular research* **42** (6), 535–544.

Gibson, C., Diaz, L., Kandarpa, K., Sacks, F., Pasternak, R., Sandor, T., Feldman, C. & Stone, P. 1993 Relation of vessel wall shear stress to atherosclerosis progression in human coronary arteries. *Arteriosclerosis, Thrombosis, and Vascular Biology* **13** (2), 310.

Gimbrone Jr, M., Topper, J., Nagel, T., Anderson, K. & GARCIA-CARDEÑA, G. 2000 Endothelial dysfunction, hemodynamic forces, and atherogenesis. *Annals of the New York Academy of Sciences* **902** (1), 230–240.

Goldsmith, H. 1971 *Red cell motions and wall interactions in tube flow.*, , vol. 30. Federation proceedings.

Goldsmith, H. & Marlow, J. 1979 Flow behavior of erythrocytes. ii. particle motions in concentrated suspensions of ghost cells. *Journal of Colloid and Interface Science* **71** (2), 383–407.

Goldsmith, H. & Mason, S. 1971 Some model experiments in hemodynamics iv. *Theoretical and Clinical Hemorheology, Springer, New York* pp. 47–59.

Hudson, S. 2003 Wall migration and shear-induced diffusion of fluid droplets in emulsions. *Physics of fluids* **15**, 1106.

Hund, S. & Antaki, J. 2009 An extended convection diffusion model for red blood cell-enhanced transport of thrombocytes and leukocytes. *Physics in medicine and biology* **54**, 6415.

Johnston, B., Johnston, P., Corney, S. & Kilpatrick, D. 2004 Non-newtonian blood flow in human right coronary arteries: steady state simulations. *Journal of Biomechanics* **37** (5), 709–720.

Jou, L. & Berger, S. 1998 Numerical simulation of the flow in the carotid bifurcation. *Theoretical and computational fluid dynamics* **10** (1), 239–248.

King, M. & Leighton Jr, D. 2001 Measurement of shear-induced dispersion in a dilute emulsion. *Physics of Fluids* **13**, 397.

Ku, D., Giddens, D., Zarins, C. & Glagov, S. 1985 Pulsatile flow and atherosclerosis in the human carotid bifurcation. positive correlation between plaque location and low oscillating shear stress. *Arteriosclerosis, Thrombosis, and Vascular Biology* **5** (3), 293–302.

Lee, D. & Chiu, J. 1996 Intimal thickening under shear in a carotid bifurcation–a numerical study. *Journal of biomechanics* **29** (1), 1–11.

Leighton, D. & Acrivos, A. 1987 The shear-induced migration of particles in concentrated suspensions. *Journal of Fluid Mechanics* **181** (1), 415–439.

Leonard, B. P. 1979 A stable and accurate convective modelling procedure based on quadratic upstream interpolation. *Computer Methods in Applied Mechanics and Engineering* **19** (1), 59–98.

Libby, P., DiCarli, M. & Weissleder, R. 2010 The vascular biology of atherosclerosis and imaging targets. *Journal of Nuclear Medicine* **51**, 33S.

Libby, P., Ridker, P. & Maseri, A. 2002 Inflammation and atherosclerosis. *Circulation* **105** (9), 1135.

Lloyd-Jones, D., Adams, R., Brown, T., Carnethon, M., Dai, S., De Simone, G., Ferguson, T., Ford, E., Furie, K., Gillespie, C. *et al.* 2010 Executive summary: heart disease and stroke statistics–2010 update: a report from the american heart association. *Circulation* **121** (7), 948.

Lowe, G., Fowkes, F., Dawes, J., Donnan, P., Lennie, S. & Housley, E. 1993 Blood viscosity, fibrinogen, and activation of coagulation and leukocytes in peripheral arterial disease and the normal population in the edinburgh artery study. *Circulation* **87** (6), 1915.

McDonald, D. 1960 Blood flow in arteries. *Baltimore, Williams and Wilkins Co* .

Merrill, E., Cokelet, G., Britten, A. & WELLS Jr, R. 1963*a* Non-newtonian rheology of human blood-effect of fibrinogen deduced by" subtraction". *Circulation Research* **13** (1), 48.

Merrill, E., Gilliland, E., Cokelet, G., Shin, H., Britten, A. & Wells Jr, R. 1963*b* Rheology of human blood, near and at zero flow:: Effects of temperature and hematocrit level. *Biophysical Journal* **3** (3), 199–213.

Merrill, E., Gilliland, E., Lee, T. & Salzman, E. 1966 Blood rheology: effect of fibrinogen deduced by addition. *Circulation research* **18** (4), 437–446.

Merrill, E., Margetts, W., Cokelet, G. & Gilliland, E. 1963*c* The casson equation and rheology of blood near zero shear. In *Symposium on Biorheology*, pp. 135–143. Interscience Publishers, New York.

Montecucco, F. & Mach, F. 2009 Atherosclerosis is an inflammatory disease. In *Seminars in immunopathology*, , vol. 31, pp. 1–3.

Moore, J. *et al.* 1994 Fluid wall shear stress measurements in a model of the human abdominal aorta: oscillatory behavior and relationship to atherosclerosis. *Atherosclerosis* **110** (2), 225–240.

Nagel, T., Resnick, N., Dewey Jr, C. & Gimbrone Jr, M. 1999 Vascular endothelial cells respond to spatial gradients in fluid shear stress by enhanced activation of transcription factors. *Arteriosclerosis, thrombosis, and vascular biology* **19** (8), 1825.

Nott, P. & Brady, J. 1994 Pressure-driven flow of suspensions: simulation and theory. *Journal of Fluid Mechanics* **275**, 157–200.

Pedley, T. 1980 *Fluid mechanics of large blood vessels*. Cambridge Press.

Perktold, K., Resch, M. & Florian, H. 1991 Pulsatile non-newtonian flow characteristics in a three-dimensional human carotid bifurcation model. *Journal of biomechanical engineering* **113**, 464.

Quemada, D. 1977 Rheology of concentrated disperse systems and minimum energy dissipation principle. *Rheologica Acta* **16** (1), 82–94.

Quemada, D. 1978 Rheology of concentrated disperse systems ii. a model for non-newtonian shear viscosity in steady flows. *Rheologica Acta* **17** (6), 632–642.

Raja BS, Susma AM, e. a. 2002 Pathogenesis of atherosclerosis: a multifactorial process. *Exp Clin Cardiol.* **7** (1), 40–53.

Ross, R. *et al.* 1999 Atherosclerosis is an inflammatory disease. *American Heart Journal* **138**, 419–420.

Sinha, R., Cross, A., Graubard, B., Leitzmann, M. & Schatzkin, A. 2009 Meat intake and mortality: a prospective study of over half a million people. *Archives of internal medicine* **169** (6), 562.

Soulis, J., Farmakis, T., Giannoglou, G. & Louridas, G. 2006 Wall shear stress in normal left coronary artery tree. *Journal of biomechanics* **39** (4), 742–749.

Soulis, J., Giannoglou, G., Chatzizisis, Y., Seralidou, K., Parcharidis, G. & Louridas, G. 2008 Non-newtonian models for molecular viscosity and wall shear stress in a 3d reconstructed human left coronary artery. *Medical engineering & physics* **30** (1), 9–19.

Stary, H. 2000 Natural history and histological classification of atherosclerotic lesions: an update. *Arteriosclerosis, thrombosis, and vascular biology* **20** (5), 1177.

Stary, H., Blankenhorn, D., Chandler, A., Glagov, S., Insull Jr, W., Richardson, M., Rosenfeld, M., Schaffer, S., Schwartz, C. & Wagner, W. 1992 A definition of the intima of human arteries and of its atherosclerosis-prone regions. a report from the committee on vascular lesions of the council on arteriosclerosis, american heart association. *Arteriosclerosis, Thrombosis, and Vascular Biology* **12** (1), 120.

Streppel, M., Ocké, M., Boshuizen, H., Kok, F. & Kromhout, D. 2009 Long-term wine consumption is related to cardiovascular mortality and life expectancy independently of moderate alcohol intake: the zutphen study. *Journal of epidemiology and community health* **63** (7), 534.

Tang, D., Yang, C., Mondal, S., Liu, F., Canton, G., Hatsukami, T. & Yuan, C. 2008 A negative correlation between human carotid atherosclerotic plaque progression and plaque wall stress: in vivo mri-based 2d/3d fsi models. *Journal of Biomechanics* **41** (4), 727–736.

Thom, T., Haase, N., Rosamond, W., Howard, V., Rumsfeld, J., Manolio, T., Zheng, Z., Flegal, K., O'Donnell, C., Kittner, S. *et al.* 2006 Heart disease and stroke statistics–2006 update: a report from the american heart association statistics committee and stroke statistics subcommittee. *Circulation* **113** (6), e85.

Thurston, G. 1979 Rheological parameters for the viscosity viscoelasticity and thixotropy of blood. *Biorheology* **16** (3), 149.

Thurston, G. 1994 Non-newtonian viscosity of human blood: flow-induced changes in microstructure. *Biorheology* **31** (2), 179.

Tortora, G. & Derrickson, B. 2006 *Principles of Anatomy and Physiology*. John Wiley & Sons.

VanderLaan, P., Reardon, C. & Getz, G. 2004 Site specificity of atherosclerosis. *Arteriosclerosis, thrombosis, and vascular biology* **24** (1), 12–22.

Walburn, F. & Schneck, D. 1976 A constitutive equation for whole human blood. *Biorheology* **13** (3), 201.

Weissberg, P. 2000 Atherogenesis: current understanding of the causes of atheroma. *Heart* **83** (2), 247.

Wilkinson, W. 1960 *Non-Newtonian Fluids*. Pergamon Press, Oxford.

Wootton, D. & Ku, D. 1999 Fluid mechanics of vascular systems, diseases, and thrombosis. *Annual review of biomedical engineering* **1** (1), 299–329.

Yang, C., Canton, G., Yuan, C., Ferguson, M., Hatsukami, T. S. & Tang, D. 2010 The role mechanical forces play in advanced human carotid plaque progression: New insights from an <i>in vivo</i> mri multi-year patient-tracking 3d fsi study. In *6th World Congress of Biomechanics (WCB 2010). August 1-6, 2010 Singapore*.

Zarins, C., Giddens, D., Bharadvaj, B., Sottiurai, V., Mabon, R. & Glagov, S. 1983 Carotid bifurcation atherosclerosis. quantitative correlation of plaque localization with flow velocity profiles and wall shear stress. *Circulation Research* **53** (4), 502.

Zydney, A., Oliver III, J. & Colton, C. 1991 A constitutive equation for the viscosity of stored red cell suspensions: Effect of hematocrit, shear rate, and suspending phase. *Journal of Rheology* **35**, 1639.

Part II

Papers

Paper 1

Proceedings of the ECCOMAS Thematic International Conference on Simulation and Modeling of Biological Flows (SIMBIO 2011) September 21–23, 2011, VUB, Brussels, Belgium

Haemodynamics in a 3D 90-degree Bifurcation

Stevin van Wyk[*], Lisa Prahl Wittberg[*] and Laszlo Fuchs[*]

1 Linné FLOW Centre KTH Mechanics, Royal Institute of Technology, Stockholm SE-100 44, Sweden, stevin@mech.kth.se

Abstract

The transport behaviour of the haematocrit in the larger arteries is important in defining the variations in viscosity of blood. In this study, a finite volume method is used in order to simulate the blood flow and haematocrit transport through a large 3D human-like 90-degree bifurcation. The simulations are carried out to investigate the importance of explicitly modelling the non-Newtonian viscosity of blood regarding defining the flow. It is expected to be especially important in the regions surrounding a bifurcation. The main focus is to compare non-Newtonian to Newtonian behaviour of the flow through important parameters such as pressure losses, mean viscosity variations and bulk transport properties of haematocrit. The study considers a broad range of physiological and pulsatile flow conditions, and displays the importance of modelling blood flow as a non-Newtonian fluid. The results have a relevant impact regarding the possible discrepencies in important physiological parameters such as wall shear stress (WSS), when coupling the haematocrit field data back to the viscosity models.

Keywords: Haemodynamics, Blood, Biomechanics, CFD, Bifurcation.

Introduction

The role of the complex viscous behaviour of human blood on the haemodynamic conditions of the cardiovascular system is important. A good example is the development and progression of cardiovascular diseases such as coronary thrombosis, which is strongly influenced by the viscous properties [5, 13] and the local distribution and interaction of Red Blood Cells (RBC) and Platelets. Platelet transport towards and deposition on the vessel wall, fundamental to plaque formation in coronary atherogenesis [4, 31], have been strongly related to blood vessel shear rate and haematocrit [1, 41]. The increased fluid shear increases the rotation of the RBC and thereby hypothesised to enhance platelet diffusivity [28]. An increase or decrease in volume fraction haematocrit on the other hand has been reported to displace or expell platelets, more or less respectively, to the cell poor fluid volumes [1, 23]. Sites of plaque formation that lead to thrombosis are common in the region of the larger 90-degree arterial branches in man. Understanding of two-phase mechanisms in blood, RBC and plasma, is therefore important in prediction and possible control of platelet deposition. Re-atherogenesis is shown to play an important role in the failure of vascular implants such as vascular grafts, artificial hearts, heart valves and ventricular assist devices [21, 32, 38, 39, 43].

Over the years several non-Newtonian models have been developed to account for the shear thinning properties of blood, with respect to two main parameters, shear rate and volume fraction haematocrit. The models are all steady state models, calibrated for ranges of fixed pressure gradients that defines the range of fixed shear rates in viscometers. The parameters are fixed by bulk macroscopic measurements and not by the microscopic suspension properties. This means that the effective viscosity defined is not an intrinsic property of the suspension, rather a property dependent on specific flow conditions and the averaging of the instrument used to measure [2, 3]. However, due to observations made during this study, it is believed that these models may define important flow field data in physiologically relevant flows; i.e. global parameters, such as pressure drop and mean transport properties of RBCs.

In this study, the temporal and spatial variations of the flow, local viscosity and haematocrit for pulsatile blood-like non-Newtonian fluid properties, in a 90-deg bifurcation, are investigated. Comparisons with Newtonian cases offer a measure for non-Newtonian behaviour of the blood if one assumes that the blood can be considered as a homogeneous mixture characterized by a mixture viscosity. Simulations are carried out with three pulsatile inflow cases, resembling varying load conditions in the human circulatory system, applied to the 3D 90 degree bifurcation geometry. Few studies of this kind have been presented in the past. To be discussed are the effects of pulsation frequency, RBC mass diffusivity, boundary conditions and viscosity on the effects of internal haemodilution (i.e. RBC concentration variations due to shear). The RBC concentration is modelled via a scalar transport model that can be coupled back to the viscosity models.

Methods

Theoretical Background

Viscosity Models

In this study, four different models have been implemented in order to quantify the dynamic viscosity (μ) of Human blood. The chosen models are identified as the most comprehensively developed and widely used, accounting for important behavioural parameters such as the existence of shear strength (shear stress required to initiate flow), Newtonian viscous limits, shear rate dependency and its dependency on cell and molecular composition [12, 44]. Three of the models are functions of both haematocrit and shear rate, while the fourth is a function of solely the latter property.

The Bird-Carreau model, initially developed for reaction kinetics of polymers and similar to a model postulated by Cross [17], describes the viscosity by the following equation [9, 27, 40]:

$$\mu = \mu_\infty + (\mu_0 - \mu_\infty)[1 + (\lambda\dot{\gamma})^2]^{\frac{n_C - 1}{2}} \tag{1}$$

Where $\mu_0 = 0.056Pas$ represents "zero shear viscosity", the viscosity value just before the fluid comes to rest; $\mu_\infty = 0.00345Pas$ is the Newtonian viscosity or "infinite shear viscosity", the viscosity value at high shear rates, $\lambda = 3.313s$ is the relaxation time constant for haematocrit, n_C is the power law index defining the degree of non-Newtonian behaviour and $\dot{\gamma}$ is the rate of shear of the flow (the same definition in each model). The Bird-Carreau model has been widely used in literature using the constant values as displayed above. It represents the widest range of shear rates of the four models since it reduces to a finite viscosity value at zero shear rate. The major disadvantage is that no explicit haematocrit dependency is defined.

The Casson model, initially derived to describe the flow behaviour of printing ink, was adapted to describing blood viscosity as follows [10, 12]:

$$\mu = \frac{\tau}{\dot{\gamma}} \tag{2}$$

$$\frac{\tau}{\dot{\gamma}} = \frac{\left[\sqrt{k_C(H)\dot{\gamma}} + \sqrt{\tau_y(H)}\right]^2}{\dot{\gamma}} \quad \text{for} \quad \tau > \tau_y(H)$$
$$\dot{\gamma} = 0 \quad \text{for} \quad \tau <= \tau_y(H) \tag{3}$$

Where τ is the fluid shear stress. Terms $k_C(H)$ and $\tau_y(H)$ are a functions of haematocrit H as follows:

$$k_C(H) = \frac{\mu_p}{(1-H)^A} \tag{4}$$

$$\tau_y(H) = \left[\frac{B}{A}((1-H)^{A/2} - 1)\right]^2 \tag{5}$$

Where μ_p and H represent the blood plasma viscosity and fraction haematocrit, respectively, values for which are displayed in Table 1. The Casson intrinsic viscosity, $k_C(H) = 0.003\ Pas$ and Shear strength, $\tau_y(H) = 0.0053\ Pa$, are both functions of haematocrit, defined according to experimental data for human blood. Constants A and B represent sets of grouped experimental constants defined in work by Cocklet et al. [15], where $A = a\beta$ and $B = a\alpha_B - 1$. The values of the constants are evaluated according to experimental data and can be used to compute the above values for $k_C(H)$ and $\tau_y(H)$ [15, 34, 35]. The model is valid over a wide range of shear rates, however, the shear rate needs to be greater than 1 s^{-1} [12, 45].

One of the most recently developed models is that of the Quemada constitutive equation, known to represent the broadest range of shear rates for blood, greater than approximately 0.01 s^{-1} [45]. It was developed to describe the Newtonian viscosity of concentrated particle suspensions through the following equation [36]:

$$\mu = \mu_p \left(1 - \frac{k(\dot{\gamma}, H)}{2} H\right)^{-2} \tag{6}$$

Where $k(\dot{\gamma}, H)$ is a function of the haematocrit, μ_p is the blood plasma viscosity and H is fraction haematocrit, for which blood values are quoted in Table 1. Here $k(\dot{\gamma}, H)$ incorporates the shear rate and haematocrit dependencies as follows [37]:

$$k(\dot{\gamma}, H) = \frac{k_0 + k_\infty(\dot{\gamma}/\dot{\gamma}_C)^{1/2}}{1 + (\dot{\gamma}/\dot{\gamma}_C)^{1/2}} \tag{7}$$

$$\dot{\gamma}_C = e^{\left(-6.1508 + 27.923H - 25.6H^2 + 3.697H^3\right)} \tag{8}$$

$$k_0 = e^{\left(3.874 - 10.41H + 13.8H^2 - 6.738H^3\right)} \tag{9}$$

$$k_\infty = e^{\left(1.3435 - 2.803H + 2.711H^2 - 0.6479H^2\right)} \tag{10}$$

Where parameters $\dot{\gamma}_C$, k_0 and k_∞ are the critical shear rate and non-dimensional intrinsic viscosities related to low and high shear rates, respectively. These correlations have been developed by Cokelet et al. [14].

The Walburn and Schneck model is an optimised power law model that includes the important dependencies on shear rate, haematocrit and plasma protein concentration [42]. Equation 11, below, displays its form.

$$\mu = C_1 e^{C_2 H} e^{C_4 \frac{TPMA}{H^2}} \dot{\gamma}^{-C_3 H} \tag{11}$$

Here the empirical constants are $C_1 = 0.000797\ Pas$, $C_2 = 0.0608$, $C_3 = 0.00499$, $C_4 = 14.585\ l/g$. Haematocrit is defined as a percentage and $TPMA = 25\ g/l$ is the total proteins minus albumin concentration for human blood. The shear rate validity for this model has been reported as being in the range greater than approximately 0.01 s^{-1} [45]. Figure 1 plots the profiles of each model.

Each of the non-Newtonian models described above are implemented with respect to corresponding shear rate validity limits mentioned. All constant material parameters used during this investigation for blood, and the Newtonian fluid, Water, are described in Table 1. The Newtonian value of viscosity for blood is that commonly found to be

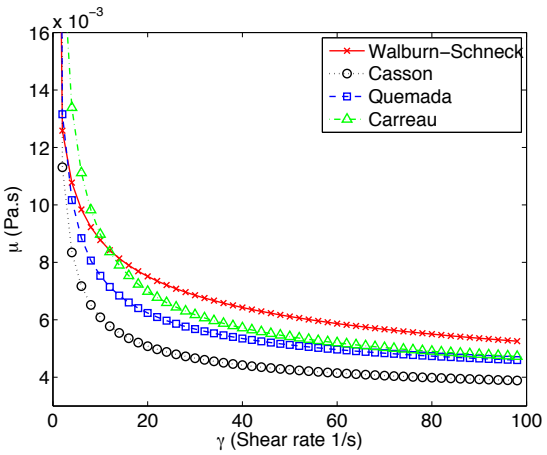

Figure 1 non-Newtonian viscosity models at 45% Heamatocrit

the lowest viscosity for blood at normal levels, approximately 3.5 times that of water. Whole blood composition (i.e. all components of the blood) at normal levels contains on average approximately 45% haematocrit [7, 18, 33].

Table 1 Material properties for Human Blood at 37 ^oC and Water at 20 ^oC

Material	Density (ρ) (kg/m^3)	Newtonian Viscosity (μ) (Pas)
Whole blood	1060 [8, 18]	0.0035 [7]
Blood plasma	1025 [7]	0.00132 [7]
Water	998.2	0.001

RBC Mass Diffusivity

The mass diffusivity of RBCs and other macro-cells is a consequence of several factors such as fluid shear, electrostatic forces and collisions. There are few studies available that quantify this property. The mass diffusivity of RBCs in concentrated suspensions is enhanced by the flow [6, 11, 24, 26, 29, 30] and constrained by close packing of neighbouring particles [16]. All studies only consider steady flow conditions in simple tube geometries and define empirical shear induced relations describing enhanced diffusivity properties of RBCs [6, 11, 24]. The values determined via these experimental studies are approximately two orders of magnitude greater than Brownian diffusion estimates. However, higher values could be expected during pulsatile flows in complex bifurcating domains. Here complex flow shear patterns, due to strong secondary flow, could further enhance diffusion. It is not yet known how transport properties of blood are affected in the region of bifurcations. Therefore, in this study, a wide range of values are considered in order to represent the possible values for diffusivity that could occur in these regions of the arterial network.

Governing Flow Equations

The flow of both the Newtonian and non-Newtonian fluids are modelled in the single phase incompressible formulation of the Navier-Stokes equations. The fluids are defined as homogeneous mixtures and expressed as:

$$\frac{\partial u_i}{\partial x_i} = 0 \tag{12}$$

$$\frac{\partial u_i}{\partial t} + u_j \frac{\partial u_i}{\partial x_j} = -\frac{1}{\rho}\frac{\partial p}{\partial x_i} + \nu \frac{\partial^2 u_i}{\partial x_j^2} \tag{13}$$

where $\nu = \mu/\rho$ is the kinetmatic viscosity. The dynamic viscosity, μ, defined through each of the non-Newtonian models, is normalised by the constant density, ρ, defining the RBC phase as having the same density as the carrier phase.

The haematocrit is modelled as an advected mixture, along with Fick's laws of diffusion, taking the form of a scalar or mass transport equation. This model uses the flow field defined by the flow equations discussed above as its advector. This form of the transport equation and mass conservation are expressed respectively as:

$$\frac{\partial H}{\partial t} = D_H \frac{\partial^2 H}{\partial x_j \partial x_j} - u_j \frac{\partial H}{\partial x_j} \tag{14}$$

Where H is the haematocrit or local volume fraction of the mixture and D_H is the mass diffusivity co-efficient thereof. The range of mass Diffusivity studied is quoted as a range of Schmidt numbers (Sc) in order to assess its influence on the possible RBC range of diffusivities. In equation 14, for mass conservation of the scalar, the left-hand side describes the change over time of the enclosed volume and the right-hand side considers the sum of advective and diffusive fluxes across the boundaries.

Charateristic velocity (U_0 - peak inlet velocity), length (D, main branch diameter) ,time (ω, angular frequency) and the average inlet volume fraction ($\overline{H}$) scales can be assigned to non-dimensionalise the mass transport equation, as follows:

$$\frac{4\alpha^2}{Re}\frac{\partial H^*}{\partial T} = \frac{1}{Pe}\frac{\partial^2 H^*}{\partial x_j^{*2}} - u_j^* \frac{\partial H^*}{\partial x_j^*} \tag{15}$$

Where $H^* = H/\overline{H}$, $T = \omega t$, $u_j^* = u_j/U_0$ and $x_j^* = x_j/D$. The non-dimensional terms, Reynolds number, Re, Womersley number, α, Peclet number, Pe and Schmidt number, Sc, can be written as:

$$Re = \frac{U_0 D}{\nu} \tag{16}$$

$$\alpha = \frac{D}{2}\sqrt{\frac{\omega}{\nu}} \tag{17}$$

$$Sc = \frac{\nu}{D_H} \tag{18}$$

$$Pe = ReSc \tag{19}$$

The Womersley number represents the relative importance of transient inertial forces versus the viscous forces. The Reynolds number relates the convective inertial forces to the viscous forces. The combination of these two numbers determines the time dependent flow properties. The Schmidt number is a measure of the rate of viscous diffusion to the rate of mass diffusion of a species in the flow. Mass diffusion here considers only that due concentration gradients. The Peclet number is a measure of dominance of advection of the species with respect to diffusion.

Numerical Methods and Case Set-up

Numerical Methods

A finite volume scheme is employed to discretize the governing equations to second accuracy. Backward implicit time advancement is employed to evolve the equations in time. A constant time step is used to ensure a time resolved solution along with the constant fulfilment of the CFL condition below 1 at each time-step. The PISO scheme maintains pressure-velocity coupling during each time step, via implementation of the pimpleFoam solver in OpenFOAM-1.6. Each of the fifteen cases require approximately 18 pulsation periods to attain a solution that is independent of the initial conditions.

A mesh consisting only of hexahedral elements is implemented. Three grids are used to investigate whether sufficient grid resolution is attained. Consecutively finer grid resolutions; 475 179, 1 410 945 and 4 818 447, grid numbers 1, 2 and 3 respectively, are created for the geometry displayed in Figure 3. The numerical grids are extended at the outlet positions displayed in Figures 3 and 5, in order to improve the description of the development of the haemtocrit in the region of the daughter branch and the bifurcation. Here backflow at the outlets, without the extensions, would lead to unrealistic, uniform distribution values entering the region of interest. The actual distribution is highly non-uniform. The averaged element size (h) for each of the three grids are related as follows; h2/h1 = 1.44 and h3/h2 = 1.51. Sufficient mesh resolution is attained with grid two of element size 1 410 945, when considering the velocity field. Care has also been taken in defining a high enough resolution in the core of the daughter branch to model the gradients important to the scalar transport model. Grid three mentioned above (cell size 4 818 447), is a local hex refinement of grid two in the region V1. It is therefore also used to evaluate the accuracy of chosen grid two in modelling the scalar transport gradients. Figure 2 shows that no further refinement of grid two is required when analyzing absolute haematocrit values and dilution behaviour, during systole, displayed at the top and bottom respectively. The Bird-Carreau non-Newtonian model is chosen to test this accuracy. Error of the order of 4% for the absolute value plot at x/d=0.5 along the z-axis, depicted at the top of Figure 2, is computed at t/T ≈0.24 just after peak flow. However, this does not significantly affect the dilution in V1, as an error of approximately 0.5% is

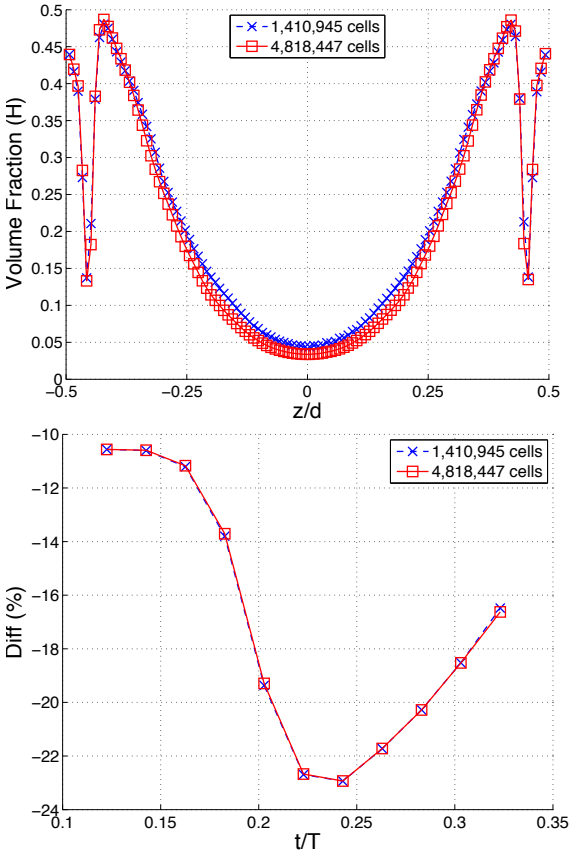

Figure 2 (top) Volume fraction haematocrit (H) line plot along the z-axis of a daughter branch cross-section at x/d=0.5 and t/T ≈0.24, as depicted in Figure 5.; (bottom) Percentage difference between average haematocrit in V1 and the inlet from t/T= 0.1 to 0.3

computed during systole, depicted at the bottom of Figure 2. The error estimate is defined as the RMS of the differences, normalised by the range of values as follows:

$$Error = \frac{\sqrt{\frac{\sum_{i=1}^{n}(\phi_{1,i} - \phi_{2,i})^2}{n}}}{(\phi_{1,2,max} - \phi_{1,2,min})} \tag{20}$$

where ϕ is the property and n is the number of samples.

Computational Geometry and Boundary Conditions

A simplified arterial model is chosen in order to avoid patient specific models. It is a simplified model resembling one of the larger arterial branches in humans adequate for understanding general flow behaviour [20]. The geometry consists of a main branch with a diameter, D =13.2 mm and a daughter branch with diameter, d =9.35 mm. The 90-degree bifurcation has a smooth, arterial like shape with an approximate radius of curvature of 9.7 mm, allowing for a time-dependent point of separation. The geometry in question is shown in Figure 3.

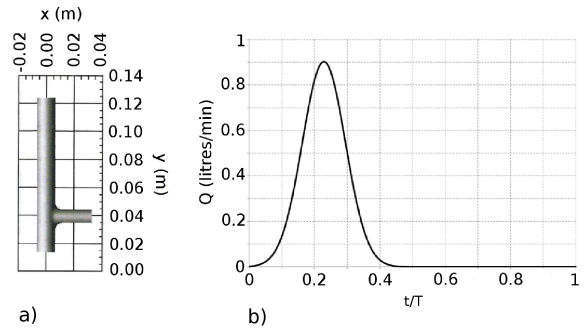

Figure 3 a) Geometric domain with absolute dimensions, b) Intel flow rate vs. Time

The choice of inflow boundary conditions, displayed in Table 2, are chosen according to characteristic arterial flow data common to the abdominal aorta and its larger branches [7]. Peak Inflow velocity or amplitude is estimated from this data. The range of periodic pulsation rates (heart rates), characteristic of arterial flows, are chosen according to a normal range representative of the in-vivo flow conditions in humans. As argued for the geometric choice, a well-defined temporal inflow profile is chosen in order to define this periodic pulsating character [19, 20].

$$Q_{INLET} = A_{MB}.U_0.e^{-0.5c^2} \quad , \quad c = \frac{\frac{t-nT}{0.6T} - 0.38}{0.11} \tag{21}$$

Where n is the number of preceding periods; i.e. for the first period $n = 0$, the second $n = 1$, etc. U_0 is the peak inlet velocity determined by the present Reynolds number, T is the period time, determined by the present Womersley number, and A_{MB} is the cross-sectional area of the main branch. The inlet flow rate vs. time is plotted in Figure 3 above for the inflow case investigated during this study.

Further boundary conditions implemented are no-slip conditions at the walls and constant reference pressures at the two outlets. The walls are modelled as rigid structures.

Regarding the scalar transport modelling, the inlet boundary conditions implemented are chosen to maintain a constant average Haematocrit, H, that is transported with each of the flow fields. Two profiles are chosen with different Haematocrit values at the walls while maintaining a constant average, shown in Figure 4. The profiles are modelled from experimental high volume fraction RBC profile measurements for laminar flows in tubes [1]. This is typical behaviour of RBCs where the RBCs migrate away from the walls in tube flow due to wall effects [22, 25]. A hyperbolic tangent equation describes this migration in tube flow, leaving a cell depleted plasma layer at the wall. The equation takes the form as follows:

$$H = \tilde{H}\left(1 + \tanh\left[m(r-\delta)\right]\right) + H_w \tag{22}$$

Here $\tilde{H}$ is a value chosen to achieve a target bulk haemtocrit of 45%, H_w is the haematocrit value set at the wall,

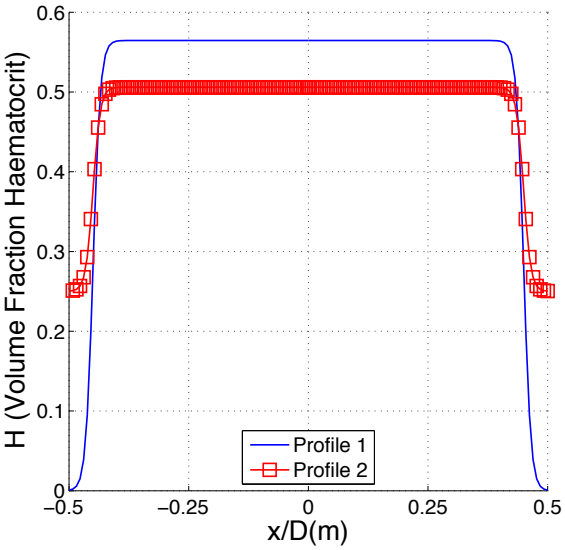

Figure 4 Implemented Haematocrit inlet profiles

r is the radial co-ordinate, m and δ are chosen to set the profile of the distribution towards the wall.

Each of the inlet haematocrit profiles maintain the zero gradient conditions to co-incide with that set at the walls. The volume field condition is initialized with the same average value of 45% as that at the inlet. Zero gradient conditions are also stipulated at both outlets.

Data is acquired after several periods depending on each flow case. The convergence criteria used for this study was that the volumetric difference in mass in the region of interest V2, from cycle to cycle, not to change by more than 1%.

Case Setup and Analysis

Three inflow cases are defined to which each of the Newtonian and non-Newtonian viscous models are applied. Each case has the same peak inflow velocity but differ in pulsation time, shown in Table 2. The range of pulsation time, presented as beats per minute (BPM), represents a range of physiological human heart rates, depending on the individual and degree of effort. Reynolds and Womersley numbers for blood are quoted as maximum values, regarding the minimum viscosity for blood quoted in Table 1.

Table 2 Case set up parameters. Peak inflow velocity, heart beats per minute (BPM), max (Re) and max (α).

	Peak Inlet Velocity (m/s)	BPM	Re	α
case 1	0.11	30	440	6.5
case 2	0.11	60	440	9
case 3	0.11	90	440	11

For each of the flow cases the scalar transport model,

representing the transport properties of RBC as a mixture, is computed. The flow is described as homogenous. That is, the RBC mixture phase or haematocrit has the same density as the carrier fluid. The haemtocrit, however, is defined as occupying a certain volume fraction of the fluid volume representing the mass of RBC. A species equation, equation 14, is used to model the mass diffusion and advection of the haematocrit as a volume fraction value. This equation is coupled back to the computed flow field (u_j). Three RBC mass diffusivities are considered for each inflow case, represented by a range Schmidt numbers defined with respect the viscosity of water, an order of magnitude apart, Sc ≈1.1, 11, 110. As stated earlier, experimental values for mass diffusivity of RBCs in complex shear flow cases does not exist in literature.

The presentation of results will refer to Table 2 when case referencing. The Newtonian reference case is used to obtain a measure of non-Newtonian behaviour and aims to show that the effects are not simply caused by an increase or decrease in Newtonian viscosity. The similarities in bulk behaviour displayed between the non-Newtonian models offers qualitative information regarding blood like mass transport phenomena.

The main region of interest, located by the shaded region in Figure 5, is due to secondary flows that influence transport properties, forming a notable separation bubble due to the 90-degree deviation in the flow. Reference dimensions and sample regions used in representing the analysed data are illustrated in Figure 5.

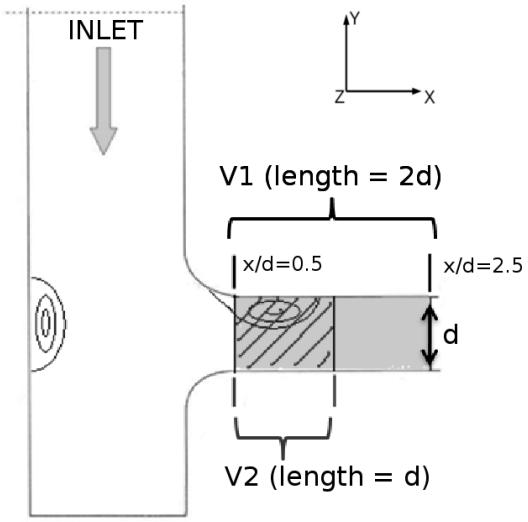

Figure 5 Co-ordinate system and region references

Volumetric data is extracted from the designated regions of interest, V1 and V2, regarding pressure gradients, viscosity and volume fraction haematocrit variations. Effects of pulsation frequency, RBC diffusivity and the distribution profile on the haemodynamic properties are presented. One-way and two-way coupled field dependencies are also compared. Region V2 is half the volume of region V1, focused on the separation bubble. It is chosen to quantify the influence, proportion wise, the separation bubble has on haematocrit variation in region V1.

Results

The results presented in the following sections will focus on the differences in transport properties for an RBC mixture using Newtonian and non-Newtonian viscosity models. Firstly, the differences non-Newtonian viscosity models share when describing blood-like flow behaviour will be discussed. The effects of RBC mass diffusivity, pulsation frequency, inlet boundary conditions (Profile 1 and 2) and the different viscosity models on transport properties in V1 will be displayed. Finally, the influence of the separation bubble on the change in haematocrit in region V1 is analysed relative to variations in region V2.

Pressure losses and Viscosity variation

Mean field pressure gradient variations, representing pressure losses, for region V1 for all non-Newtonian models relative to water are depicted in Figure 6. Mean pressure gradient values for case 1 initially show a sharp increase, becoming larger than that of water. This coincides with the initial high mean levels in viscosity and an increasing flow rate during systole, Figure 7. The maximum differences in peak pressure gradient around t/T ≈0.18 are approximately 20% for between the Bird-carreau and Casson models. During this increase in flow rate to the point of peak systole the pressure gradient tends to be higher than for water. Almost immediately after the peak pressure gradient a sudden drop takes place for all cases, reaching a minimum just after peak systole before rising again. This also coincides with the minimum mean viscosity where the shear rates are highest. From this point onwards much lower pressure gradients exist compared to water for case 1. Case 3 continues to rise from the point just after peak systole at t/T ≈0.24, where pressure gradients are lower than that of water, to t/T ≈0.32 where higher pressure gradients than that of water peak again. From this point onwards there is a drop again, until t/T ≈0.5 where the pressure gradient is slightly lower than water. Around t/T ≈0.7 the pressure gradients begin to resemble that of water as the blood comes to rest or exhibits minimal motion. Thereafter the pressure gradient differences almost disappear as flow ceases during diastole. In general, during the pulsation cycles for all frequencies, large differences in pressure gradient are observed between the non-Newtonian viscosity models and the Newtonian model water.

The viscosity variation plots displayed in Figure 7 show that as the flow rate increases during systole, all the models and cases reach a minimum at peak inflow, t/T ≈0.22. As the flow rate decreases the viscosity increases again until a point at t/T ≈0.55 for case 1 and t/T ≈0.7 for case 2. There is no distinct point at which a peak is reached in case 3, as the subsequent decrease seen in case 1 is due to reverse flow. As the pulsation frequency increases reverse flow in region V1 decreases and

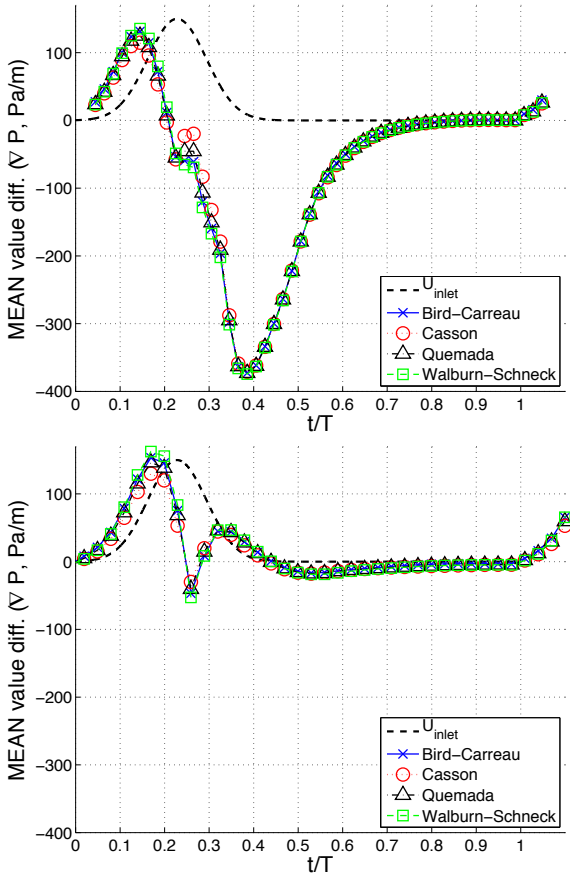

Figure 6 Difference in the mean pressure gradient (∇P) for all non-Newtonian models minus the pure Newtonian case (Water) for (top) Case 1 and (bottom) case 3.

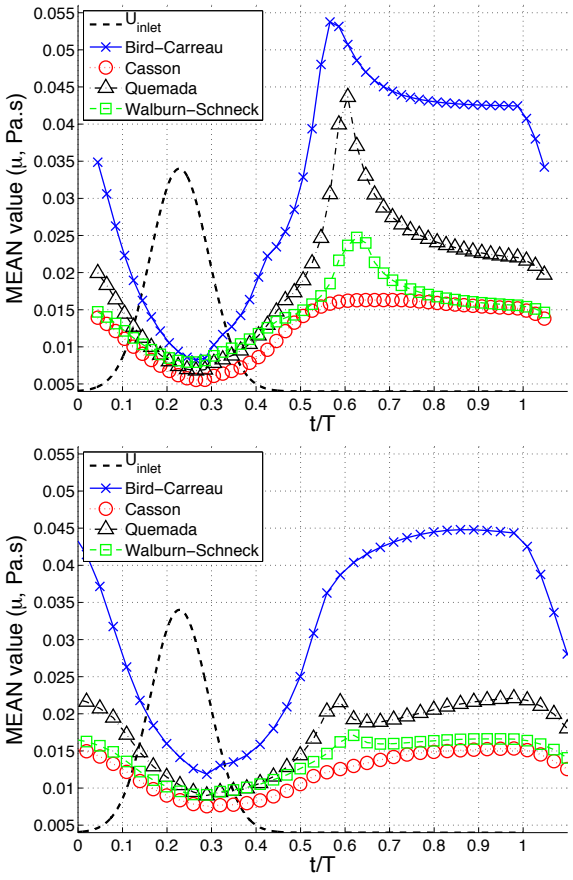

Figure 7 Difference in mean field viscosity (μ) quantities for all non-Newtonian models in region V1 for (top) Case 1 and (bottom) Case 3.

takes place for a shorter period of time at 90 bpm. It is also observed that each of the viscosity models exhibit very different peaks in viscosity. This is due to the validity limits set for each model that are constrained differently at shear rates less than 1 s^{-1}. The reason for the Bird-Carreau model to display the highest mean viscosity is due to being the only model valid for the full range of shear rates, including zero shear rate. The results presented in this section dislplays the importance of describing the fluid, blood, as non-Newtonian in character. The non-Newtonian flow behaviour is therefore more important than a simple increase or decrease in viscosity and will describe vastly different transport behaviour than a Newtonian fluid like water would.

Dilution characteristics

The dilution charaterictics are quantified as the temporal variation of the average haematocrit fraction in region V1 minus the inlet average. In all figures the dilution variation is displayed as a percentage difference or deviation with reference to inlet profile 1. Large variations are observed in the region of the daughter branch when advection dominates i.e. at high Schmidt numbers. The highest Schmidt number investigated during the study is 110 for which diffusion is observed to be very low. In the region of bifurcations, flow features such as separation and secondary flows cause these large variations due to shear. Early on in the pulsation cycle the centrifugal effect, characteristic to the radius of the bifurcation curvature, leads to the flow separation and generates secondary vortices. The shear layers produced by these secondary flows leads to the mass transport behaviour affecting haematocrit dilution in the region of bifurcations.

Figure 8 shows the progression of dilution for cases 1 and 3 in region V1 as a percentage drop in fraction. In all cases the general progression is similar and correlates with the applied inflow characteristics. However, with increasing pulsation frequency the correlation becomes less. For case 1 the first stage of systole shows an increase in dilution leading to a maximum around peak systole, at $t/T \approx$0.22, of as high as 22% for the Bird-Carreau model and lowest 16% for the Casson model. For case 3 there is a delay in peak dilution, taking place at around $t/T \approx$0.3, leading to dilution of 20% and 12% for the same models as in case 1. This is an expected delay for higher Womersley numbers, where the transient inertia is higher leading to a delay in the core flow momentum. Formation of the sep-

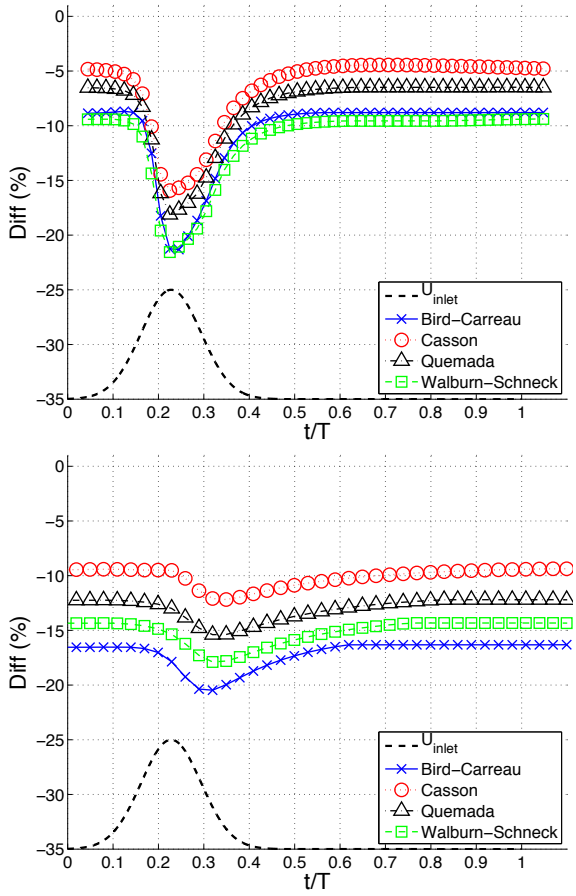

Figure 8 Comparison of mean fraction haematocrit difference in region V1, minus the inlet average, for (top) Case 1 and (bottom) Case 3.

aration bubble is therefore delayed, due to the flow taking more time to accelerate to a certain velocity. The absolute increase in dilution between systole and diastole for case 1 is larger than that for case 3. Case 1 shows an absolute difference of between 11 and 12% and Case 3 only between 3 and 4%, considering the same viscosity models as earlier. The is caused due to the diminished size of the separation bubble at higher pulsation frequencies. The delay in formation and the shorter pulsation time, decreases the time available for the separation bubble to form. The size of the separation bubble can be depicted by the local extent of negative axial flow (backflow) near the bifurcation, in the daughter branch. Figure 9 displays the axial velocity contours of the Bird-Carreau model at t/T ≈0.34, after systole, when the separation bubble approximately nears its maximum size for all cases. The localised 'bubble' of backflow decreases in size as the pulsation frequency increases. The emphasis or focus on the impact of the separation bubble is described in the section following.

After the peak in dilution, the separation bubble continues to grow during the deceleration stage of systole. A steady decrease in dilution is observed in both cases 1 and 3, eventually reaching a constant bulk haematocrit fraction in the domain. Case 1 reaches this point between t/T ≈0.4 and 0.6 and case 3 between t/T ≈0.6 and 0.8, depending on the viscosity models. The minimum dilution is therefore attained and ranges between 9% and 5% for case 1 and between 16% and 10% for case 3, regarding the Bird-

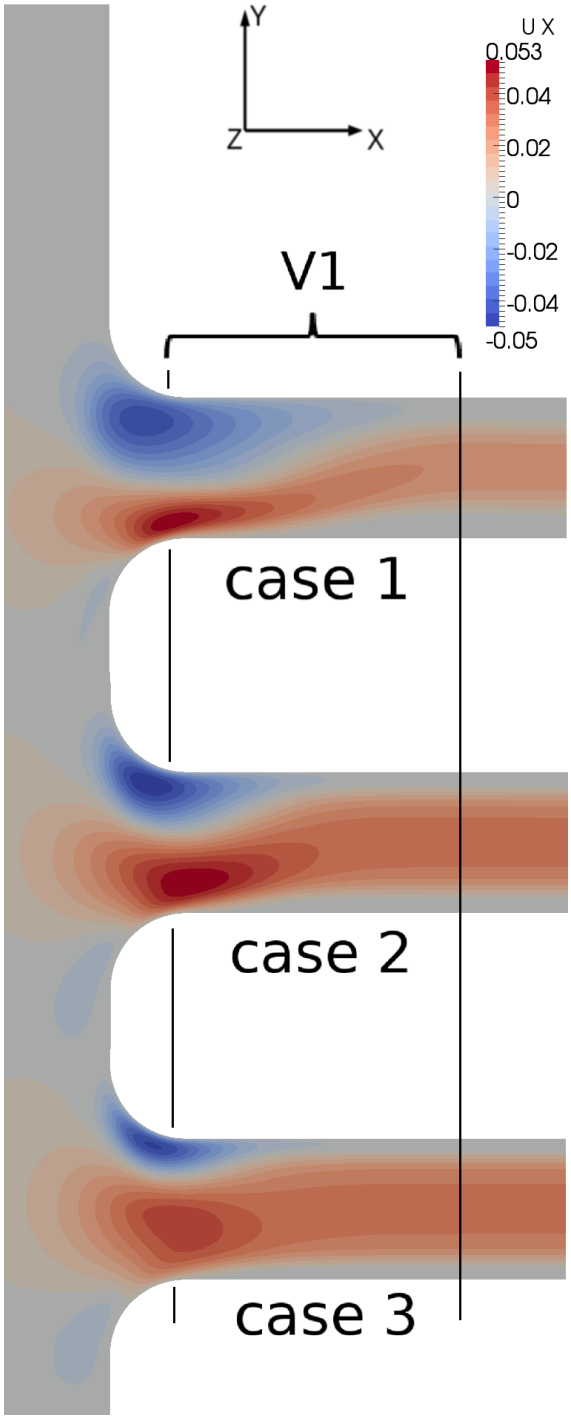

Figure 9 Axial velocity (m/s) contours relative to the daughter branch of all cases for the Bird-Carreau model, at t/T ≈0.34.

Carreau and Casson viscosity models respectively. The differences in the dilution properties described by the different viscosity models are due to a combination of the differences in their viscosity limits and non-Newtonian behavioural description. However, there is a consistent observation that can be made regarding the extent of dilution throughout the pulsation cycle. The non-Newtonian model with the consistently highest mean viscosity, as seen in Figure 7, generates the highest levels of dilution. This can be observed for both cases in Figure 8 and is also true when considering the minimums. In general the Bird-Carreau and the Casson models represent the two extremes for maximum and minimum dilution respectively. Models Walburn-Schneck and Quemada always tend to define values between these models and can be seen to be strongly related to the mean viscosity defined in Figure 7. This in turn can be related to the shear layer thickness defined by each viscosity model. A higher mean viscosity is associated with thicker shear layers in the daughter branch.

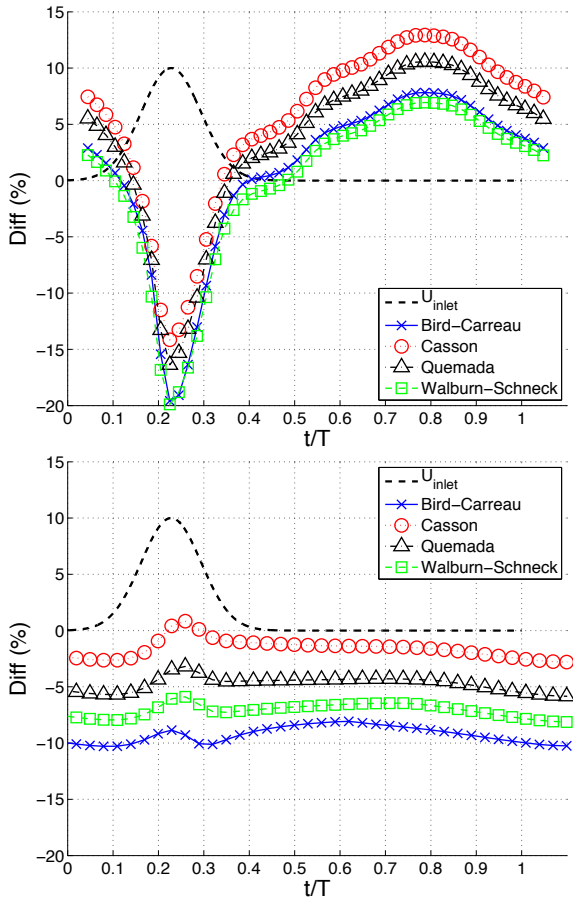

Figure 10 Comparison of mean fraction haematocrit difference in region V1, minus the that defined by water, for (top) Case 1 and (bottom) Case 3.

Another fundamental behavioural property displayed in Figure 8 is the difference in the maximum range of haematocrit variation or dilution for each viscosity model. As the pulsation frequency increases this range decreases i.e. there is smaller difference between the systolic and diastolic dilution in case 3 than in case 1. This can be explained through equation 15, describing the effect of non-dimensional parameters, Reynolds (Re), Womersley(α) and Schmidt (Sc) numbers, on the transport. The plots in Figure 8 maintain constant Re and Sc, but increase α as the frequency increases. This therefore means that the $\frac{\partial H^*}{\partial T}$ term, which signifies the rate of change in haematocrit over time, decreases and is consistent with what is observed in the results. Another important feature is that case 3 also shows a lower value of dilution during the diastolic phase than case 1, reflected by all the viscosity models. This can be understood by the above explanation and

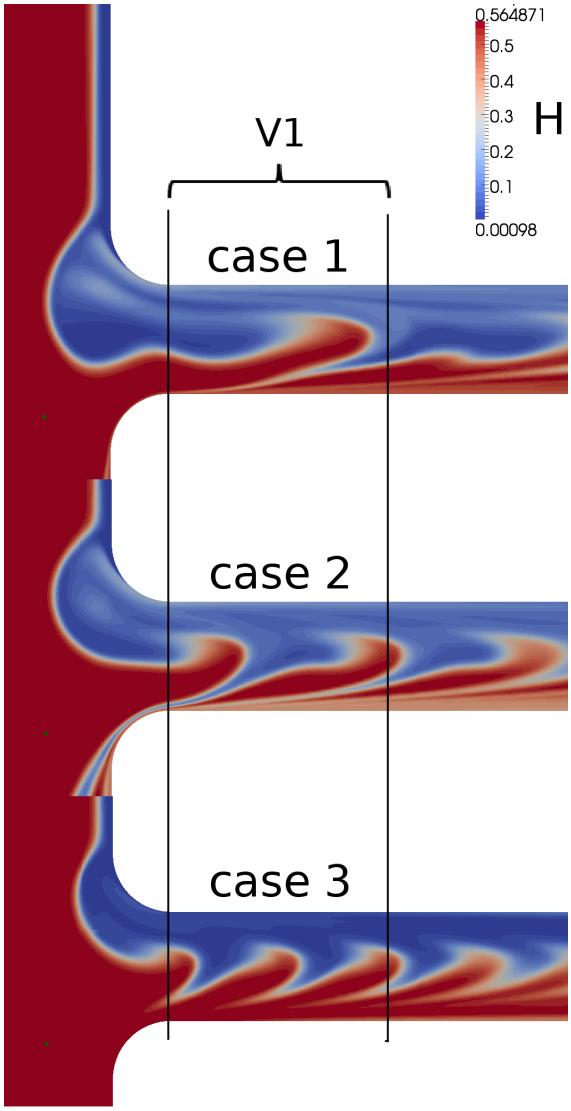

Figure 11 Example of local haematocrit fraction variation for all cases at t/T =1 (end of the cycle), with increasing frequency, focusing on region V1. Data is extracted at the centre channel cross-section, showing the complete bifurcation profile.

can be graphically expressed by the number of haematocrit pulses or packets existing in region V1 at any point in time during diastole. Figure 11 uses the Bird-Carreau viscosity model as an example to illustrate the evolution of the pulses of haematocrit with increasing frequency from case 1 to 3 respectively. The diminished size of the separation bubble for increased frequency is also evident, described earlier as one of the main reasons for decrease in the total increase in dilution from the diastolic level.

The impact of defining blood as a non-Newtonian fluid, in order to model its two phase flow properties, is quantified by comparing its dilution behaviour to that of water. Figure 10 displays temporal data of the dilution defined by non-Newtonian models minus the dilution defined by water for case 1 and case 3, in relation to Figure 8. In case 1 it is observed that during diastole (t/T =0.4 to 1) there is a difference in relative dilution. This is due to the flow of water alone, as all non-Newtonian models show no change in dilution during this part of the cycle. The dilution defined by the non-Newtonian viscosity models shows a maximum of between 7 and 13% less compared to water. The reason for this is that water has a relatively low Newtonian viscosity and is observed to maintain momentum in the flow throughout the cycle, since much less force is required to move a volume of fluid. This means that transport properties vary by advection througout the cycle. In case 3 it can be notice that the difference during diastole is much less pronounced as compared to case 1. This in turn is due to the same reasons described earlier, refering to equation 15. The non-Newtonian models display greater dilution throughout this part of the cycle, ranging between 1 and 10%.

During the systolic part of the cycle for case 1, between t/T=0 and 0.4, there are large differences in dilution. From the start of systole to the peak there is a very steap progression in relative difference, leading to a peak dilution of between 14 and 20%. After peak systole, during the decelaration phase, there is a steady decrease in dilution until a constant dilution value is reached again during diastole. This sharp variation in definition of dilution behaviour displays the degree of importance in modelling the two phase flow of blood by non-Newtonian viscosity models.

Influence of Separation Bubble

The smaller region V2 is used in order to focus on the dilution properties surrounding the separation bubble, in order to further quantify the importance of the influence that the separation bubble has on the dilution properties within region V1. At high Schmidt numbers and due to the formation of secondary flows in the daughter branch enhanced dilution behaviour exists.

Figure 12 shows the dilution properties existing in V2, along with a plot depicting its percentage difference relative to region V1. Figure 12 (top) shows that there is a maximum dilution around peak systole as in V1, with a dilution of between 25 and 32%. However, the maximum dilution is 50 to 60% greater as compared to that displayed for V1, depicted in Figure 12 (bottom) denoting the % greater drop. During peak systole, all viscosity models display the same trend, showing the dominant influence of the formation of the separation bubble. At this heart cycle frequency, region V2 shows a constantly high dilution influence, even throughout diastole, depending on the viscosity model. The different viscosity models display a great discrepancy where the Casson model shows an 80% greater drop as apposed to the Bird-Carreau model where there is a constant value of about 10% after systole. The higher value obtained using the Casson model is due to a much lower mean viscosity observed during diastole, compared to that for the Bird-Carreau model, shown in Figure 7. The effect of the flow is a combination of improved mixing and backflow mechanisms for the Casson model and the opposite effect for the Bird-Carreau model, during the transport of haematocrit. When considering the Casson model these effects carry more haematocrit away from both regions, upstream, back towards the junction, thereby further diluting the regions. Hence the greater drop percentage during diastole, than for the Bird-carreau model.

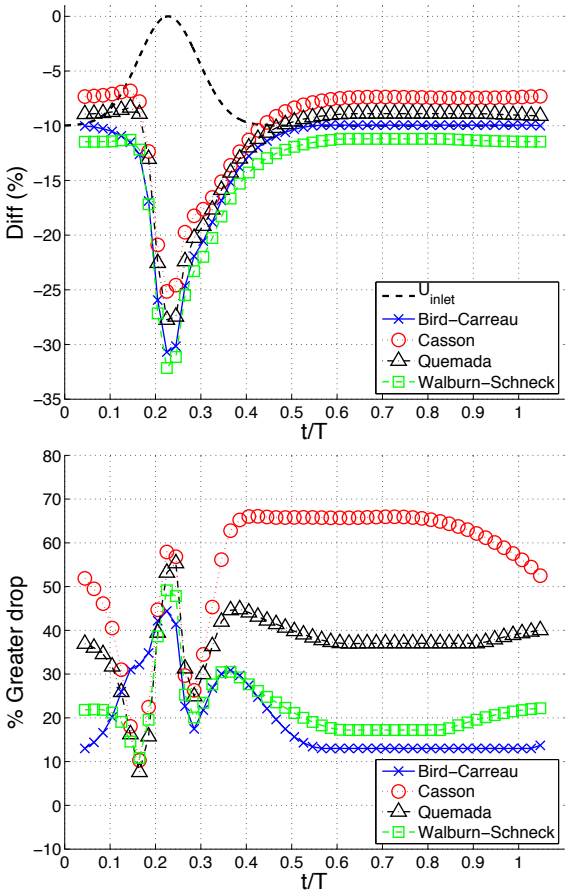

Figure 12 Case 1 (top) mean fraction haematocrit difference in region V2 with respect to the inlet average and (bottom) (%) greater drop in region V2 vcompared to region V1.

For case 3, Figure 13 displays the same form of dilution

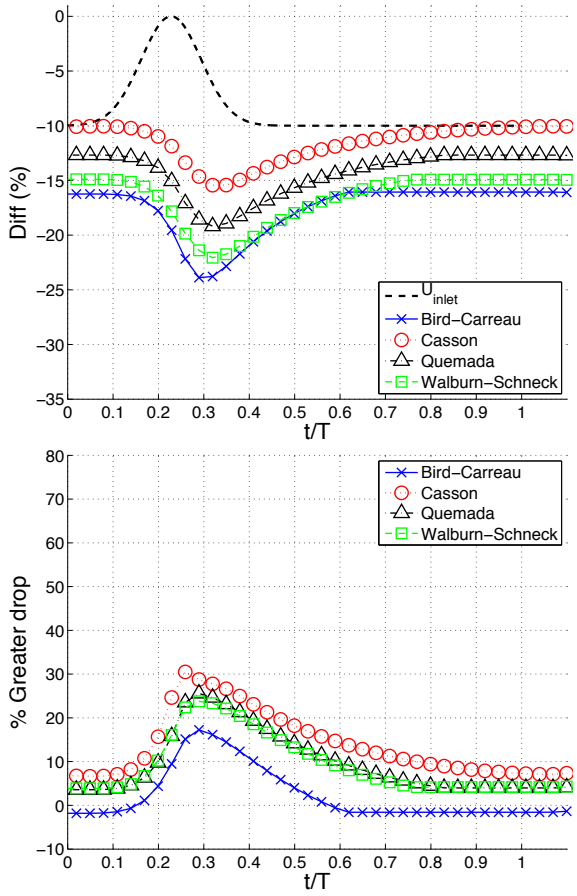

Figure 13 Case 3 (top) mean fraction haematocrit difference in region V2 with respect to the inlet average and (bottom) (%) greater drop in region V2 vcompared to region V1.

as for case 1 above. During diastole, when comparing the dilution to that occuring in region V1, there is little difference in the progression from the results displayed in Figure 8. However, there is a peak dilution around $t/T \approx 0.3$ of approximately 15 to 24% appearing during systole where the separation bubble influences the flow. This leads to a reasonably large contribution from V2 to the overall dilution in V1, signified by a 15 to 30% greater drop. Unlike case 1, there is not enough time for the flow to develop enough for mixing and backflow to play a significant role for this heart cycle frequency. The most influencial secondary flow mechanism affecting dilution behaviour is the formation of the separation bubble, causing segregated flow patterns which narrows the channel of transport into the daughter branch, during systole.

Effect of RBC profile and Schmidt number

It is of interest to understand the influence the Schmidt number as well as the inlet haematocrit profiles has on the dilution. Moreover, whether or not both RBC inlet profiles produce significant dilution, is interesting when considering the differences in variation of both Newtonian and non-Newtonian viscosity models. Also, the Sc number for which advective or diffusive fluxes dominate the flow for non-Newtonian viscosity models is as well.

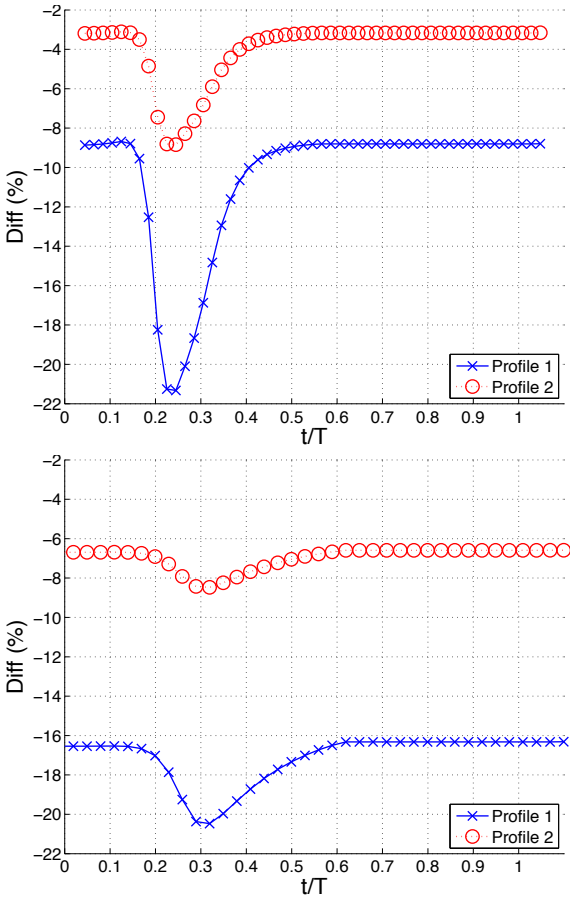

Figure 14 Difference in dilution behaviour of the Bird-Carreau model described by profile 1 and 2 for (top) Case 1 and (bottom) Case 3.

Haematocrit Inlet profile conditions

In Figure 14 the variation of dilution between cases 1 and 3 are compared for both profiles for the Bird-Carreau model. Both cases 1 and 3 display the same trend. The dilution for case 1 shows that there is a difference of 6% between the profiles during diastole and up to 12% difference near peak systole. Considering the dilution for case 3 there is a larger difference between the profiles during diastole of 10% but with a peak systole difference repeatative of case 1. Both profiles describe large, clear variations from what is imposed at the inlet. Since each profile defines the same average inlet haematocrit, the differences in dilution behaviour come from the minimum value at the wall and the gradients inherently defined. The trend described by Figure 14 is similar for all viscosity models.

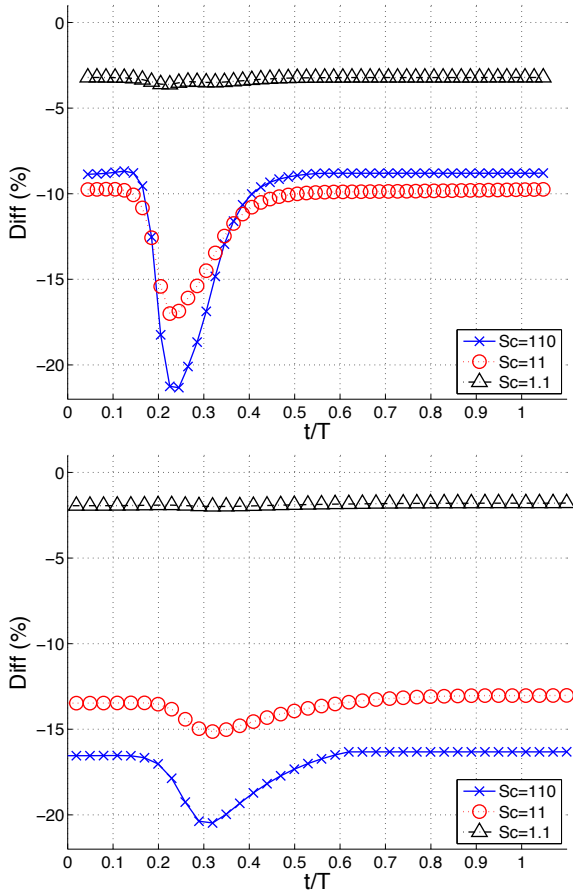

Figure 15 Difference in dilution behaviour of the Bird-Carreau model described by the range of Schmidt number investigated, between Sc = 1.1 and 110 (top) case 1 and (bottom) case 3.

Schmidt number variation

The variation of the Schmidt number represents the possibility of the increase in mass diffusivity of the haematocrit when interacting with enhanced secondary flows in the region of the bifurcation. Figure 15 shows the variation of haematocrit over a cycle for the three Schmidt numbers studied, using case 1 and case 3, region V1 and the Bird-Carreau model. The dilution is strongly influenced by the increase in Schmidt number. From $Sc \approx$11 and higher the dilution during diastole is similar around 9 to 10% (1% difference) for case 1, while displaying a larger difference for case 3 of up to 3%. Case 3 shows an additional 4 and 8% increase in diastolic dilution, for Sc =11 and 110 respectively. The higher pulsation frequency means that there are more frequent haematocrit packets generated, causing a greater increase in level of dilution. The higher Schmidt numbers are more important at higher heart pulsation frequencies.

During peak systole the difference between the higher Schmidt numbers, Sc =11 and 110, is as large as 4% for case 1 and 5% for case 3. The difference between the Schmidt numbers stays similar for all cases. However, the obsolute increase in dilution from diastole to systole is still larger for larger values of Sc. This difference is even greater when considering region V2. At low Schmidt numbers, Sc =1.1, the diffusive time scale is small enough, allowing the diffusive flux to penetrate the separation bubble. This means that only a minor variation in dilution during peak systole is experienced. There is, however, a constant dilution value of approximately 3% existing throughout the cycle. As discussed earlier, the haematocrit or the RBCs have a low mass diffusivity in high concentrations and therefore advection dominates the transport behaviour. All viscosity models display similar trends.

Conclusions

This investigation has carried out analysis of flow field and transport behaviour of a blood like fluid. The possible extent of importance of modelling blood in its true character, as a non-Newtonian viscous fluid, is quantified. Data representing pressure losses, viscosity variations and haematocrit transport behaviour has yielded:

- There are large variations in mean pressure gradients and viscosity throughout the heart cycle, at physiological pulsation frequencies between 30 and 90 beats per minute, for all non-Newtonian models relative to the Newtonian model water. This varies throughout the heart cycle for pulses between 30 and 90 beats per minute. Describing the flow from a non-Newtonian viscosity perspective is observed to be more important than a simple increase or decrease in Newtonian viscosity.

- Bulk dilution in the extended region V1 is as high as 16 to 22% in terms of RBC concentration, for case 1, representing low heart pulses of 30 bpm, and 12 to 20% for case 3, representing higher heart pulses of 90 bpm. Large changes in fraction haematocrit therefore exists in a 90 degree branch with respect to the average inlet value.

- Large differences in bulk dilution between non-Newtonian and Newtonian models exists. At peak systole up to 14 and 20% difference can be observed at low heart pulse frequencies of 30 bpm and 10% at higher pulse frequencies. This shows the importance of describing transport porperties of haematocrit via non-Newtonian viscosity models.

- The contribution of the separation bubble to bulk dilution behaviour is important. It defines the large variations throughout the heart cycle, especially during systole. Relative bulk dilution increase in region V2 with respect to V1 is as high as 60% near peak systole for case 1 and 30% for case 3.

- The large variations in bulk haematocrit existing at high Schmidt numbers, when comparing non-Newtonian to Newtonian viscosity models, implies

that there should be important influences on viscosity that need to be considered. The viscosity of blood is dependent on local haematocrit fraction.

In future work the haematocrit fraction will be coupled back to viscosity models to define a more complete viscosity dependency. It is then feasible to investigate physiological parameters such as Wall Shear Stress, thought to be important in the development of vascular diseases.

Acknowledgements

The financial support from the Swedish Research Council (Vetenskapsrådet) is greatly acknowledged. Computational resources were provided by the Swedish National Infrastructure for Computing (SNIC) and the High Performance Computing Center North (HPC2N).

References

[1] P. Aarts, S. Van Den Broek, G. Prins, G. Kuiken, J. Sixma, and R. Heethaar. Blood platelets are concentrated near the wall and red blood cells, in the center in flowing blood. *Arteriosclerosis, Thrombosis, and Vascular Biology*, 8(6):819, 1988.

[2] H. Barnes. A review of the slip (wall depletion) of polymer solutions, emulsions and particle suspensions in viscometers: its cause, character, and cure. *Journal of Non-Newtonian Fluid Mechanics*, 56(3):221–251, 1995.

[3] H. Barnes. Measuring the viscosity of large-particle (and flocculated) suspensions–a note on the necessary gap size of rotational viscometers. *Journal of non-newtonian fluid mechanics*, 94(2-3):213–217, 2000.

[4] H. Baumgartner and C. Haudenschild. Adhesion of platelets to subendothelium. *Annals of the New York Academy of Sciences*, 201(1):22–36, 1972.

[5] R. Becker. The role of blood viscosity in the development and progression of coronary artery disease. *Cleveland Clinic journal of medicine*, 60(5):353, 1993.

[6] J. Bishop, A. Popel, M. Intaglietta, and P. Johnson. Effect of aggregation and shear rate on the dispersion of red blood cells flowing in venules. *American Journal of Physiology-Heart and Circulatory Physiology*, 283(5):H1985, 2002.

[7] J. Bronzino, editor. *The Biomedical Engineering Handbook, second edition*. Boca Raton: CRC Press LLC, 2000.

[8] D. Brooks, J. Goodwin, and G. Seaman. Interactions among erythrocytes under shear. *Journal of applied physiology*, 28(2):172, 1970.

[9] P. Carreau. Rheological equations from molecular network theories. *Journal of Rheology*, 16:99–127, 1972.

[10] N. Casson. *Rheology of disperse systems*. Pergamon Press, London, 1959.

[11] W. Cha and R. Beissinger. Evaluation of shear-induced particle diffusivity in red cell ghosts suspensions. *Korean Journal of Chemical Engineering*, 18(4):479–485, 2001.

[12] S. Charm and G. Kurland. Blood rheology. *Cardiovascular fluid dynamics*, 2, 1972.

[13] Y. Cho and K. Kensey. Effects of the non-newtonian viscosity of blood on flows in a diseased arterial vessel. part 1: Steady flows. *Biorheology*, 28:241, 1991.

[14] G. Cockelet. The rheology and tube flow of blood. *Handbook of Bioengineering*, page 14, 1987.

[15] G. Cockelet, E. Merrill, E. Gilliland, H. Shin, A. Britten, and R. Wells Jr. The rheology of human blood–measurement near and at zero shear rate. *Journal of Rheology*, 7:303–307, 1963.

[16] E. Cohen and I. De Schepper. Transport properties of concentrated colloidal suspensions. *AIP Conference Proceedings*, 256:359, 1992.

[17] M. Cross. Kinetic interpretation of non-newtonian flow. *Journal of Colloid and Interface Science*, 33(1):30–35, 1970.

[18] J. Cutnell and K. Johnson. *Physics, 8th Edition*. Wiley, 1998.

[19] P. Evegren, L. Fuchs, and J. Revstedt. On the secondary flow through bifurcating pipes. *Physics of Fluids*, 22:103601, 2010.

[20] P. Evegren, L. Fuchs, and J. Revstedt. Wall shear stress variations in a 90-degree bifurcation in 3d pulsating flows. *Medical engineering & physics*, 32(2):189–202, 2010.

[21] A. Garatti, G. Bruschi, T. Colombo, C. Russo, M. Lanfranconi, F. Milazzo, M. Frigerio, and E. Vitali. Clinical outcome and bridge to transplant rate of left ventricular assist device recipient patients: comparison between continuous-flow and pulsatile-flow devices. *European Journal of Cardio-Thoracic Surgery*, 34:275, 2008.

[22] H. Goldsmith. *Red cell motions and wall interactions in tube flow.*, volume 30. Federation proceedings, 1971.

[23] H. Goldsmith. The flow of model particles and blood cells and its relation to thrombogenesis. *Progress in hemostasis and thrombosis*, 1:97, 1972.

[24] H. Goldsmith and J. Marlow. Flow behavior of erythrocytes. ii. particle motions in concentrated suspensions of ghost cells. *Journal of Colloid and Interface Science*, 71(2):383–407, 1979.

[25] H. Goldsmith and S. Mason. Some model experiments in hemodynamics iv. *Theoretical and Clinical Hemorheology, Springer, New York*, pages 47–59, 1971.

[26] S. Hudson. Wall migration and shear-induced diffusion of fluid droplets in emulsions. *Physics of fluids*, 15:1106, 2003.

[27] B. Johnston, P. Johnston, S. Corney, and D. Kilpatrick. Non-newtonian blood flow in human right coronary arteries: steady state simulations. *Journal of Biomechanics*, 37(5):709–720, 2004.

[28] K. Keller. Effect of fluid shear on mass transport

in flowing blood. In *Federation proceedings*, volume 30, page 1591, 1971.

[29] M. King and D. Leighton Jr. Measurement of shear-induced dispersion in a dilute emulsion. *Physics of Fluids*, 13:397, 2001.

[30] D. Leighton and A. Acrivos. The shear-induced migration of particles in concentrated suspensions. *Journal of Fluid Mechanics*, 181(1):415–439, 1987.

[31] P. Libby, M. DiCarli, and R. Weissleder. The vascular biology of atherosclerosis and imaging targets. *Journal of Nuclear Medicine*, 51:33S, 2010.

[32] P. Lin, R. Bush, Q. Yao, A. Lumsden, and C. Chen. Evaluation of platelet deposition and neointimal hyperplasia of heparin-coated small-caliber eptfe grafts in a canine femoral artery bypass model1. *Journal of Surgical Research*, 118:45–52, 2004.

[33] G. Lowe, F. Fowkes, J. Dawes, P. Donnan, S. Lennie, and E. Housley. Blood viscosity, fibrinogen, and activation of coagulation and leukocytes in peripheral arterial disease and the normal population in the edinburgh artery study. *Circulation*, 87(6):1915, 1993.

[34] E. Merrill, E. Gilliland, G. Cokelet, H. Shin, A. Britten, and R. Wells Jr. Rheology of human blood, near and at zero flow:: Effects of temperature and hematocrit level. *Biophysical Journal*, 3(3):199–213, 1963.

[35] K. Perktold, M. Resch, and H. Florian. Pulsatile non-newtonian flow characteristics in a three-dimensional human carotid bifurcation model. *Journal of biomechanical engineering*, 113:464, 1991.

[36] D. Quemada. Rheology of concentrated disperse systems and minimum energy dissipation principle. *Rheologica Acta*, 16(1):82–94, 1977.

[37] D. Quemada. Rheology of concentrated disperse systems ii. a model for non-newtonian shear viscosity in steady flows. *Rheologica Acta*, 17(6):632–642, 1978.

[38] C. Schmid, T. Tjan, C. Etz, C. Schmidt, F. Wenzelburger, M. Wilhelm, M. Rothenburger, G. Drees, and H. Scheld. First clinical experience with the incor left ventricular assist device. *The Journal of heart and lung transplantation*, 24:1188–1194, 2005.

[39] Y. Shapira, A. Sagie, R. Jortner, Y. Adler, and R. Hirsch. Thrombosis of bileaflet tricuspid valve prosthesis: clinical spectrum and the role of nonsurgical treatment. *American Heart Journal*, 137:721–725, 1999.

[40] J. Soulis, G. Giannoglou, Y. Chatzizisis, K. Seralidou, G. Parcharidis, and G. Louridas. Non-newtonian models for molecular viscosity and wall shear stress in a 3d reconstructed human left coronary artery. *Medical engineering & physics*, 30(1):9–19, 2008.

[41] V. Turitto and H. Baumgartner. Platelet interaction with subendothelium in a perfusion system: physical role of red blood cells. *Microvascular Research*, 9(3):335–344, 1975.

[42] F. Walburn and D. Schneck. A constitutive equation for whole human blood. *Biorheology*, 13(3):201, 1976.

[43] M. Wilhelm, D. Hammel, C. Schmid, A. Rhode, T. Kaan, M. Rothenburger, J. Stypmann, M. Schafers, C. Schmidt, H. Baba, et al. Long-term support of 9 patients with the debakey vad for more than 200 days. *Journal of thoracic and cardiovascular surgery*, 130:1122–1129, 2005.

[44] W. Wilkinson. *Non-Newtonian Fluids*. Pergamon Press, Oxford, 1960.

[45] A. Zydney, J. Oliver III, and C. Colton. A constitutive equation for the viscosity of stored red cell suspensions: Effect of hematocrit, shear rate, and suspending phase. *Journal of Rheology*, 35:1639, 1991.

2

Paper 2

Wall shear stress variations and unsteadiness of pulsatile blood-like flows in 90-degree bifurcations

Stevin van Wyk[*], Lisa Prahl Wittberg[*], and Laszlo Fuchs[*]

KTH Mechanics, Royal Institute of Technology, Stockholm SE-100 44, Sweden, stevin@mech.kth.se

To be submitted to Medical Engineering and Physics

Abstract

Over the last decades advancements have been made in the understanding of the complex mechanical and biochemical processes in atherogenesis. Complex interaction of the different processes govern the development of atherosclerosis, a previously assumed to be lipid storage disease. It has been shown that fluid mechanical forces could play an important role for the pathological changes of the endothelium. This study provides further indications for the effects of fluid mechanical aspects often correlated with the diseased regions of larger arteries. The effects of non-Newtonian viscosity models are important for the flow behaviour. The regions of reversed flow are more pronounced near the bifurcation in disease correlated areas. The Red Blood Cell (RBC) volume fraction is also important for the magnitudes of the wall shear stress (WSS) and its gradients. Unsteady high temporal WSS gradients (WSSG) are found moving downstream with flow stagnation. This elevated temporal gradient is due to the shear-thinning property of the non-Newtonian viscosity, the magnitude of which is dependent on the RBC volume fraction. The focal nature of the gradient has direct implications on the response of the endothelium.

Keywords: Wall shear stress, Wall shear stress gradients, Biomechanics, CFD, Blood, Atherosclerosis.

Nomenclature

Symbol	*Description*	Units
μ	*Effective Dynamic Viscosity*	Pas
τ	*Fluid Shear Stress*	Pa
$\dot{\gamma}$	*Shear rate magnitude*	s^{-1}
H	*Haematocrit (V_{RBC}/V_{Total})*	-
V_{RBC}	*Volume of RBCs*	m^3
V_{Total}	*Total fluid volume*	m^3
μ_p	*Plasma Dynamic Viscosity*	Pas
$TPMA$	*Total Proteins Minus Albumin*	g/l
IFC	*Inflow case*	-
C	*Casson model*	-
Q	*Quemada model*	-
WS	*Walburn-Schneck model*	-
BPM	*Heart Beats per minute*	min^{-1}
U_0	*Peak Mean Inlet Velocity*	m/s
D	*Diameter of main branch*	m
d	*Diameter of daughter branch*	m
$P1$	*Inlet RBC Profile 1*	-
$P2$	*Inlet RBC Profile 2*	-
$\overline{\lvert\tau\rvert_{Peaks}}$	*Mean value of Coupled Peak WSS magnitudes*	Pa
$\lvert d\tau/dt\rvert_{Peak}$	*Peak temporal WSSG magnitude*	Pa/s

Introduction

Atherosclerosis is a common cardiovascular disease that progradiates rather slowly. It may lead to thrombosis in the coronary and aortic arterial branches causing disruption of blood flow to important regions of these organs. The formation or development of atherosclerosis is initially localized to the region of a sharp curvature or bifurcation. The flow in these regions is characterized by flow separation, reversed flow and unsteadiness and has been strongly attributed to the development process over the last sixty years [7, 11, 19, 23, 32].

The flow behaviour is thought to affect biological processes through increased residence times or biochemical release processes. Direct mechanical forces on the endothelial layer, on the other hand, have been related to the dysfunction or damage to the cells. In recent times, both these processes have been studied through variations in wall shear stresses (WSS). One of the most common correlations to atheroma location is regions of low WSS, which has been thought to be related to the modified transport of solutes at the arterial wall [9, 10]. More recently correlations have been made between a combination of low time-averaged and oscillatory WSS with plaque location. Both experimental and numerical, steady and pulsatile flow studies have been carried out to relate this low

time-averaged and the oscillatory WSS character to regions of reversed flow and sites prone to disease [3, 4, 24, 28, 45]. It is often mentioned that this is thought to affect the mass transport of atherogenic materials in the lumen, increasing residence times near the arterial walls [4, 8, 28]. There are also suggestions from studies that link high WSSG to the disruption of the endothelial cell layer, causing disorientation or damage [18, 22, 35]. Intimal hyperplasia, thought to be an initiator to atherogenesis and a consequence of relevant WSSG components [17, 27, 44], is related to widening and stretching of endothelial cell junctions [29]. There is no definitive reason or process that can account for the atherogenic processes, other than to say that plaque sites correspond largely to regions of flow separation, reversed flow, low and oscillatory WSS, and the departure from unidirectional flow.

The aim of this study is to investigate temporal and spatial variations of the WSS for a blood like fluid in regions where plaques are commonly found. The flow is affected by local viscosity variations due to variations in local RBC volume fraction in the region of the bifurcation. The computational results will be related to current hypotheses relating WSS variations to the possible risk sites. Three different non-Newtonian viscosity models are considered for three inflow conditions, considering an increase in the peak flow rate and heart frequency rates. To the knowledge of the authors, this is the first numerical study of its kind considering coupling of the local RBC volume fraction variation affecting the viscosity of the blood flow in large arteries. This study is based upon a geometry used in a previous Newtonian flow study to which comparison can directly be made [21].

Methods

Theoretical Background

Viscosity Models

The blood is a multiphase mixture of water with cells and molcules of widely different size. The volume of RBC is about 45% of the total blood volume. The cells and the macro-molecules contribute to the non-Newtonian behaviour of the viscosity of the blood. The local RBC concentration cannot be assumed to be constant as the cells are subject to different forces. Thus, a realistic model of blood viscosity requires that the temporal and spatial distribution of the RBC is accounted for and this is integrated into the viscosity models. In this study, three different viscosity models have been implemented accounting for the local variation in RBC concentration and thereby quantifying the dynamic shear viscosity of human blood. The chosen models are identified as the most comprehensively developed and widely used concerning RBC fraction and shear rate (also dependent on the RBC concentration).

The ***Casson model***, initially derived to describe the flow behaviour of printing ink, was adapted to describing blood viscosity as follows [12, 13]:

$$\mu = \frac{\tau}{\dot{\gamma}} \tag{1}$$

$$\frac{\tau}{\dot{\gamma}} = \frac{\left[\sqrt{k_C(H)\dot{\gamma}} + \sqrt{\tau_y(H)}\right]^2}{\dot{\gamma}} \quad \text{for} \quad \tau > \tau_y(H)$$
$$\dot{\gamma} = 0 \quad \text{for} \quad \tau <= \tau_y(H) \tag{2}$$

The terms $k_C(H)$ (Casson viscosity) and $\tau_y(H)$ (Shear Strength) are functions of H as follows:

$$k_C(H) = \frac{\mu_p}{(1-H)^A} \tag{3}$$

$$\tau_y(H) = \left[\frac{B}{A}((1-H)^{A/2} - 1)\right]^2 \tag{4}$$

The constants A and B represent grouped experimental constants, where $A = a\beta$ and $B = a\alpha_B - 1$ [15]. The values of the constants are evaluated according to experimental values for $k_C(H) = 0.003\ Pas$ and $\tau_y(H) = 0.0053\ Pa$, determined for human blood at H ∼45 % [15, 33, 36]. The model is valid over a wide range of shear rates, greater than 1 s^{-1} [13, 46].

One of the most recently developed models is that of the ***Quemada constitutive equation***, quoted as representing one of the broadest range of shear rates for blood, greater than approximately 0.01 s^{-1} [46]. It was developed to describe the shear thinning viscosity dependency of concentrated particle suspensions through the following equation [37, 38]:

$$\mu = \mu_p \left(1 - \frac{\frac{k_0 + k_\infty(\dot{\gamma}/\dot{\gamma}_C)^{1/2}}{1+(\dot{\gamma}/\dot{\gamma}_C)^{1/2}}}{2} H\right)^{-2} \tag{5}$$

Parameters $\dot{\gamma}_C$, k_0 and k_∞ are the critical shear rate and non-dimensional intrinsic viscosities related to low and high shear rates, respectively. Empirical correlations for the RBC concentration dependency on each of these parameters has been developed as follows [14]:

$$\dot{\gamma}_C = e^{\left(-6.1508 + 27.923H - 25.6H^2 + 3.697H^3\right)} \tag{6}$$

$$k_0 = e^{\left(3.874 - 10.41H + 13.8H^2 - 6.738H^3\right)} \tag{7}$$

$$k_\infty = e^{\left(1.3435 - 2.803H + 2.711H^2 - 0.6479H^2\right)} \tag{8}$$

The ***Walburn-Schneck model***, is quoted as being an optimised power law model [43]. Equation 9, below, displays its form.

$$\mu = C_1 e^{C_2 H} e^{C_4 \frac{TPMA}{H^2}} \dot{\gamma}^{-C_3 H} \tag{9}$$

Here the empirical constants are $C_1 = 0.000797\ Pa.s$, $C_2 = 0.0608$, $C_3 = 0.00499$, $C_4 = 14.585\ l/g$. H is defined as a percentage and $TPMA = 25$ for human

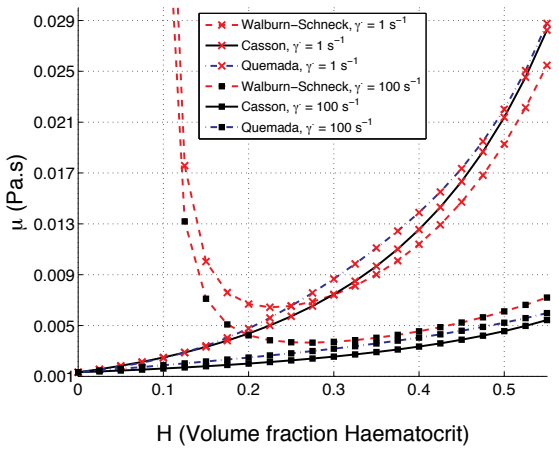

Figure 1 non-Newtonian viscosity model dependency on RBC concentration

blood. The model is valid for shear rate greater than approximately 0.01 s^{-1} [46].

Figure 1 shows the profiles of each model at low and high shear rates of 1 and 100 s^{-1}, respectively. The shear rate validity limits mentioned for each model are used to define the viscosity limits. A haematocrit (RBC concentration) limit is only set for the Walburn-Schneck model at approximately 25 % due to the invalid relationship at lower haematocrit fractions, clearly displayed by Figure 1. All material constant parameters used for density, Newtonian viscosities (water and plasma) are described in Table 1. The bulk RBC volume fraction per volume of whole blood composition at normal levels contains on average approximately 45% haematocrit [5, 16, 31].

Table 1 Properties for Human Blood at 37 ^oC and Water at 20 ^oC

Material	Density (ρ) (kg/m^3)	Viscosity (μ) (Pas)
Whole blood	1060 (ρ_m) [6, 16]	-
Blood plasma	1025 (ρ_p) [5]	0.00132 (μ_p) [5]
Water	998.2 (ρ_w)	0.001 (μ_w)

Governing Flow Equations

The flow of Newtonian and non-Newtonian fluids can be modelled by a single phase incompressible formulation of the Navier-Stokes equations. The fluids are defined as homogeneous mixtures and expressed as;

$$\frac{\partial u_i}{\partial x_i} = 0 \tag{10}$$

$$\frac{\partial u_i}{\partial t} + u_j \frac{\partial u_i}{\partial x_j} = \frac{1}{\rho}\left[-\frac{\partial p}{\partial x_i} + \mu \frac{\partial^2 u_i}{\partial x_j \partial x_j}\right] \tag{11}$$

Here, μ is defined through each of the non-Newtonian or Newtonian models and normalised by constant fluid densities, ρ, defining the RBC or haematocrit phase as having the same density as the carrier phase i.e. blood plasma.

The advection of the haematocrit mixture is modelled via equation 12. Here we assume that all forces acting on the RBCs can be expressed by a single effect, namely that of diffusivity. The evolving haematocrit distribution is coupled back to the flow field through the dynamic shear viscosity dependency. The form of the transport equation and thereby mass conservation can be expressed as;

$$\frac{\partial H}{\partial t} = D_H \frac{\partial^2 H}{\partial x_j \partial x_j} - u_j \frac{\partial H}{\partial x_j} \tag{12}$$

where H is the haematocrit or local RBC volume fraction and D_H is the mass diffusivity coefficient thereof. Values of the mass diffusivity for the RBCs corresponding to a Schmidt number (Sc) range relative to the viscosity of water correspond to the following;

$$11 < Sc = \frac{\mu}{\rho D_H} < 110 \tag{13}$$

Characteristic velocity (U_0 - peak inlet velocity), length (D, main branch diameter) ,time (ω, angular frequency) scales can be assigned to non-dimensionalise the Navier-Stokes equation, as follows:

$$\frac{4\alpha^2}{Re}\frac{\partial u_i^*}{\partial T^*} + u_j^* \frac{\partial u_i^*}{\partial x_j^*} = -\frac{\partial p^*}{\partial x_i^*} + \frac{1}{Re}\frac{\partial^2 u_i^*}{\partial x_j^{*2}} \tag{14}$$

where $T^* = \omega t$, $u_i^* = u_i/U_0$, $u_j^* = u_j/U_0$, $x_i^* = x_i/D$, $p^* = p/\rho {U_0}^2$ and $x_j^* = x_j/D$. The non-dimensional terms, the Reynolds number Re and the Womersley number α, can be written as:

$$\alpha = \frac{D}{2}\sqrt{\frac{\omega\rho}{\mu}} \tag{15}$$

$$Re = \frac{U_0 D \rho}{\mu} \tag{16}$$

The Womersley number represents the relative importance of transient versus viscous effects, whereas the Reynolds number relates the convective inertial forces to the viscous forces. The combination of these two numbers determines the time dependent flow properties.

Numerical Methods and Case Set-up

Numerical Methods

A finite volume scheme is employed to discretize the governing equations to second order accuracy. Backward implicit time advancement is employed to evolve the equations in time. A constant time step is used to ensure a time resolved solution along with the constant fulfilment of the CFL condition below 1 at each time-step. The RBC transport equation is solved and the subsequent computed (local) RBC concentration coupled to the solution of the

Navier-Stokes equation via the evaluation of the local non-Newtoninian shear viscosity models. Depending on the flow rate, the cases required approximately between 9 and 18 (heart-cycle) periods to obtain a solution, independent of the initial conditions.

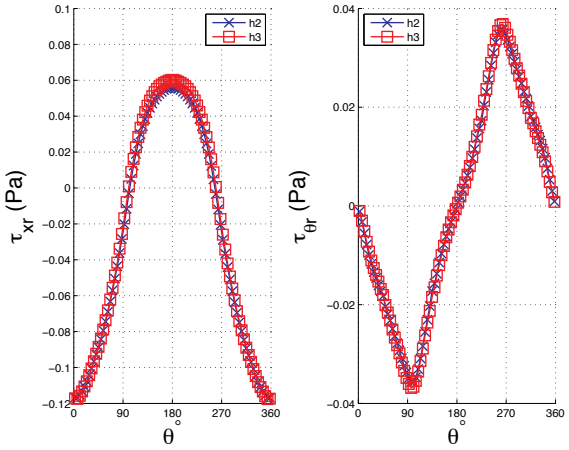

Figure 2 Axial (left) and azimuthal (right) wall shear stress components vs. the azimuthal co-ordinate for grids $h2$ and $h3$ at the x/d=0.68 axial cross-sectional position of the daughter branch.

We consider the flow in a geometry displayed in Figure 3. For the grid sensitivity study, three hexahedral grids have been used. Grid $h1$, $h2$ and $h3$ contain 475 179, 1 410 945 and 4 818 447 cells, respectively. The outlets of the daughter and main branches are extended by 5 and 2 pipe diameters, respectively. This is done in order to improve the description of the development of the RBC distribution in the regions of the daughter branch and the bifurcation. Here, flow reversal may occur at the outlets if no extension is used. This is inconsistent with the assumptions made at the outflow boundaries. By extending the domain, the flow is unidirectional at the outlet boundaries. The averaged element size (h) for each of the three grids are related as follows; $h2/h1 = 1.44$ and $h3/h2 = 1.51$. Sufficient mesh resolution is attained with grid $h2$ of element size 1 410 945 considering the velocity field gradients. However this does not guarantee that the WSS stress gradients, are predicted with sufficient accuracy, due to coupling with the RBC field. Grid $h3$ (cell size 4 818 447), is a local hex refinement of grid $h2$ in the region of interest and used to evaluate the accuracy of grid $h2$ with respect to the WSS gradients. Figure 2 displays the results with the two grids, showing the adequacy of grid $h2$ when analysing the absolute values of WSS in the axial and azimuthal directions, displayed at the left and right frames, respectively. The Casson non-Newtonian model is used in this accuracy test. An error of less than 2 % for the axial WSS (τ_{xr}) at x/d=0.68 along the y-axis is found at $t/T \approx 0.42$ near the end of systole. There are sharp changes in the azimuthal component of WSS ($\tau_{\theta r}$). However, the approximate error is only 0.5 % and corresponds to the largest error in WSS during the cycle. The error estimate is defined as the RMS of the differences, normalised by the range of values as follows:

$$Error = \frac{\sqrt{\frac{\sum_{i=1}^{n}(\phi_{1,i} - \phi_{2,i})^2}{n}}}{(\phi_{1,2,max} - \phi_{1,2,min})} \quad (17)$$

where ϕ is the property and n is the number of samples.

Computational Geometry and Boundary Conditions

A simplified arterial model is chosen in order to avoid patient specific models. It is a simplified model resembling one of the larger arterial branches in humans adequate for understanding general flow behaviour [21]. The geometric dimensions shown in Figure 3 for D =13.2 mm and d =9.35 mm [21]. The 90-degree bifurcation has a smooth, arterial like shape with an approximate radius of curvature of 9.7 mm, allowing for a time-dependent point of separation.

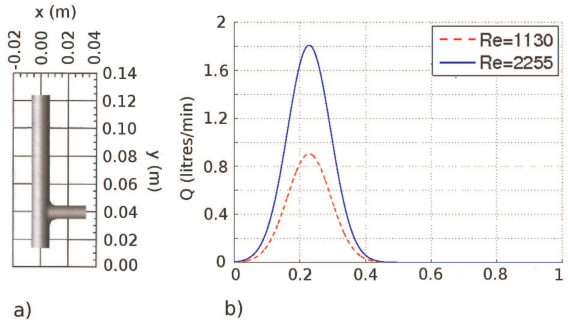

Figure 3 a) Geometric domain with absolute dimensions, b) Intel flow rate vs. Time

Different inflow boundary conditions, displayed in Table 2, are chosen according to characteristic arterial flow data common to the abdominal aorta and its larger branches [5]. Peak Inflow velocity or amplitude is estimated from this data. The range of periodic pulsation rates (heart rates), characteristic of arterial flows, are chosen according to a normal range representative of the *in-vivo* flow conditions in humans. As argued for the geometric choice, a well-defined temporal inflow profile is needed in order to determine the periodic pulsating character of the flow and its frequency (Womersley number) response [20, 21, 41].

$$Q_{IN} = A_D.U_0.e^{-0.5c^2} \quad , \quad c = \frac{\frac{t - nT}{0.6T} - 0.38}{0.11} \quad (18)$$

where n is the number of preceding periods; i.e. for the first period $n = 0$, the second $n = 1$, etc. U_0 is determined by the Reynolds number, T is the period time, determined by the Womersley number, and A_D is the cross-sectional area of the main branch. The inlet flow rate vs. time is

Table 2 Case set-up matrix. An **x** indicates a simulated case.

Inflow Case (IFC) No.				**Newtonian**	**non-Newtonian**							
				Water	*un-Coupled*			*Coupled*				
					Models			Inflow Parameters		Models		
U_0	BPM	Re	α		C	Q	WS	*RBC Profs*	Sc	C	Q	WS
	1							*P2*	*110*	**x**	**x**	**x**
				x	**x**	**x**	**x**	*P1*	*110*	**x**	**x**	
0.11	*60*	*1130*	*14.6*					*P1*	*11*	**x**	**x**	
	2							*P2*	*110*	**x**	**x**	**x**
				x	**x**	**x**	**x**	*P1*	*110*	**x**	**x**	
0.11	***90***	*1130*	***18.2***					*P1*	*11*	**x**	**x**	
	3							*P2*	*110*	**x**	**x**	**x**
				x	**x**	**x**	**x**	*P1*	*110*	**x**	**x**	
0.22	*60*	***2260***	*14.6*					*P1*	*11*	**x**	**x**	

plotted in Figure 3 for the inflow cases investigated in this study.

On the walls the no-slip condition is applied, whereas constant reference pressures are given at the two outlets. The walls are modelled as rigid structures.

The inlet boundary condition for the RBC transport equation is chosen to maintain a constant average (bulk) haematocrit, H, for each of the flow cases. The profiles are taken from observations of experimental RBC profile measurements for laminar flows in large arterial scale tubes [1]. The typical away migration of RBCs near the walls in arteriole or capillary scale tube flow, due to wall effects at low shear rates, is also displayed in previous experimental studies [25, 26]. In these studies which are at high shear rates (not encountered in large arteries) RBCs tend to migrate towards the wall, whereby the RBC phase display enhanced diffusive behaviour. A hyperbolic tangent equation is used to model the inlet behaviour observed in large arterial flow, with a cell depleted layer near the walls. Thus, the inlet RBC concentration profile takes the following form:

$$H = \widetilde{H}\left(1 + \tanh\left[m(r - \delta)\right]\right) + H_{wall} \tag{19}$$

Here $\tilde{H}$ is a value chosen to achieve a target bulk haemtocrit of 45 %, H_{wall} is the haematocrit fraction value set at the wall, r is the radial co-ordinate, m and δ are chosen to qualitatively describe the distribution towards the wall. H_{wall} is set to two different values, 0 (0 %) and 0.25 (25 %), to study the effect of the different inlet profiles, P1 and P2, respectively. This represents one of the possible ways of defining an increased RBC concentration toward the walls, and thereby the sensitivity to the inlet RBC distribution boundary conditions. Zero gradient conditions are set at the walls by each of these profiles to be consistent with the zero gradient conditions at the walls throughout the domain. Zero gradient conditions are also applied at both outlets.

Several periods are required before periodicity criteria is met so that the effects of initial conditions are eliminated whereby data could be extracted. The periodicity criterion used here is that the volumetric difference in RBC mass in the region of interest does not change by more than 1%, from cycle to cycle.

Case Setup and Analysis

The range of flow cases considered are given in Table 2. Three inflow cases are studied representing the effect of an increase in flow rate and an increase in heart pulsation frequency. The heart pulsation range, in Beats Per Minute (BPM), represents two typical physiological human heart rates. The flow rates or peak average inlet velocities are within the range of values common between the ascending and abdominal aortic regions and their larger branches. The inflow cases are dependent on the individual, the degree of effort and the possible variation in arterial dimensions. The Reynolds and Womersley numbers for blood are as quoted, regarding the most consistent viscosity values for blood, the blood plasma viscosity (μ_p), given in Table 1. Blood plasma is assumed to be a Newtonian fluid [5]. The considered cases include the effect of an increase in RBC mass diffusivity through a decrease in Schmidt number Sc and the variation of RBC concentration gradients via the RBC distribution profiles, P1 and P2. In Table 2 the non-Newtonian models are refered to as either coupled or un-coupled, meaning that the evolution of viscosity is either dependent on the computed haematocrit field or not, respectively.

The dominance of the advective properties due to the flow scales studied have been demonstrated in a previous study, where Sc numbers above 11 display a significantly lower influence of diffusive fluxes [41]. The values for the effective RBC diffusivities implemented are therefore approximately two to three orders of magnitude greater than

that found in literature for tube flow experiments.

The formation of a notable separation bubble and secondary flows in the daughter branch, due to the 90-degree deflection of the flow, is thought to be important for atherogenesis. Hence, our region of interest is the region close to the bifurcation and it is shown by the shaded region in Figure 4. A co-ordinate system and reference dimensions used in denoting domain locations and the axial and azimuthal components of the physiological variables are also illustrated in Figure 4. Flow cases are referred to according to the notation in Table 2.

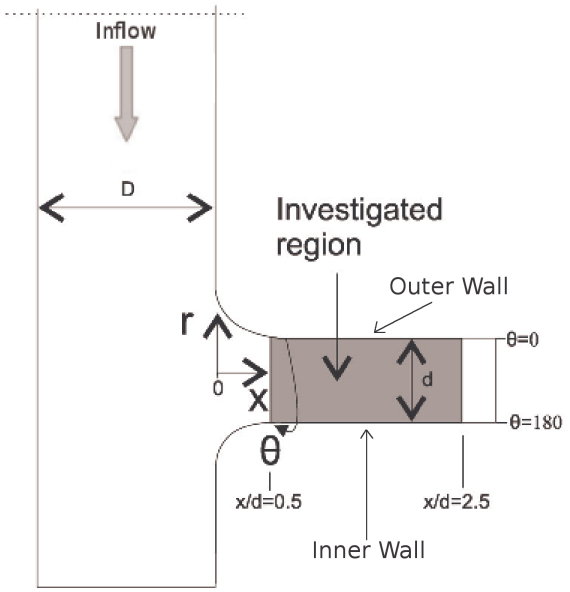

Figure 4 Axial and azimuthal reference co-ordinate system and location of the investigated region in the daughter branch, taken from a previous study [21]

Results

The aim of this study is to investigate the sensitivity of WSS dynamics to changes in the non-dimensional numbers (Re,α,Sc) as well as the effects of blood-like non-Newtonian viscosity. Spatial and temporal WSS variations and gradients are the focus in regions commonly susceptible to disease formation in arterial bifurcations. Reversed flow behaviour in the daughter branch is analysed also since regions prone to disease have been associated with regions of secondary, separated and reversed flows [7, 11]. A comparison between the Newtonian and non-Newtonian viscosity models is also made. In recent times elevated WSSGs have been the focus of studies relating to regions of plaque formation and endothelial function [2, 17, 27, 44].

Temporal WSS derivatives

Both spatially and temporally varying WSSGs have been hypothesized to be related to the possible dis-orientation of endothelial cells or complex induced stresses that affect biochemical expression in the endothelial layer. The proliferation of cells in the endothelial layer has been associated with the early stages of atherogenesis, which in turn has been found to be enhanced by elevated temporal WSSGs [27, 44]. The most notable in the present study is the temporal derivative variation at the outer wall near the bifurcation, where plaque formation typically starts. The formation and motion of a focal peak is observed during systole, coinciding with the formation of the separation bubble. A point sample over time at x/d=0.58 and azimuthal angle $\theta = 4.6°$, consistent with the WSS analysis to follow, is used to represent the flow dynamics in the outer wall region. In this region spatial derivatives are not very different in character from those of the Newtonian model, described in a previous study for the same geometry. The distribution of the spatial derivative is not as strikingly focal to atherogenic related regions as the temporal derivative.

In Figure 5 the temporal derivatives are plotted for both the uncoupled and coupled non-Newtonian viscosity models for each inflow case. The plot on the left depicts Inflow Cases 2 and 3, normalized with respect to the peaks of each model in Inflow Case 1, providing information regarding the increase in the scale of the gradient with the increase in pulsation frequency and flow rate, respectively. The plot on the right depicts the difference in gradient with respect to the Newtonian model.

At pulsation frequencies 60 and 90 BPM, Inflow Cases 1 and 2, the common trend shows an increase in gradient to around t/T=0.1 followed by a fast, steady decrease to near peak systole. A sharp peak is reached for all non-Newtonian model simulations, both coupled and uncoupled. This peak arises due to co-incidence with a stagnation point that moves past this position on the wall. The stagnation point forms between the separation bubble and the reattached flow downstream. The existence of the stagnation point leads to a sudden increase in viscosity due to the sudden, substantial decrease in shear rate, evident in Figure 10. With an increase in pulsation frequency to 90 BPM, Figure 5 (a) shows that the peak temporal gradient is doubled and follows a similar pattern to 60 BPM. Similarly, the increased flow rate of Inflow Case 3 also displays a doubling of the gradient at the first sharp peak near t/T=0.2. The peak occurs earlier due to the increased Reynolds number and the faster development of the separation bubble, leading to faster movement of the stagnation point.

The plot on the RHS gives an indication of the relative difference in temporal gradient with respect to the Newtonian model. Each of the non-Newtonian models shows a sharp difference near peak systole (t/T=0.22), with the uncoupled models defining much greater positive and negative gradient magnitudes as compared to the coupled. This is due to the greater peak magnitudes displayed in Figure 9 and a similar time scale between the peaks. The coupled models show decreased magnitudes due to the lower viscosities defined via the consistently lower volume fractions

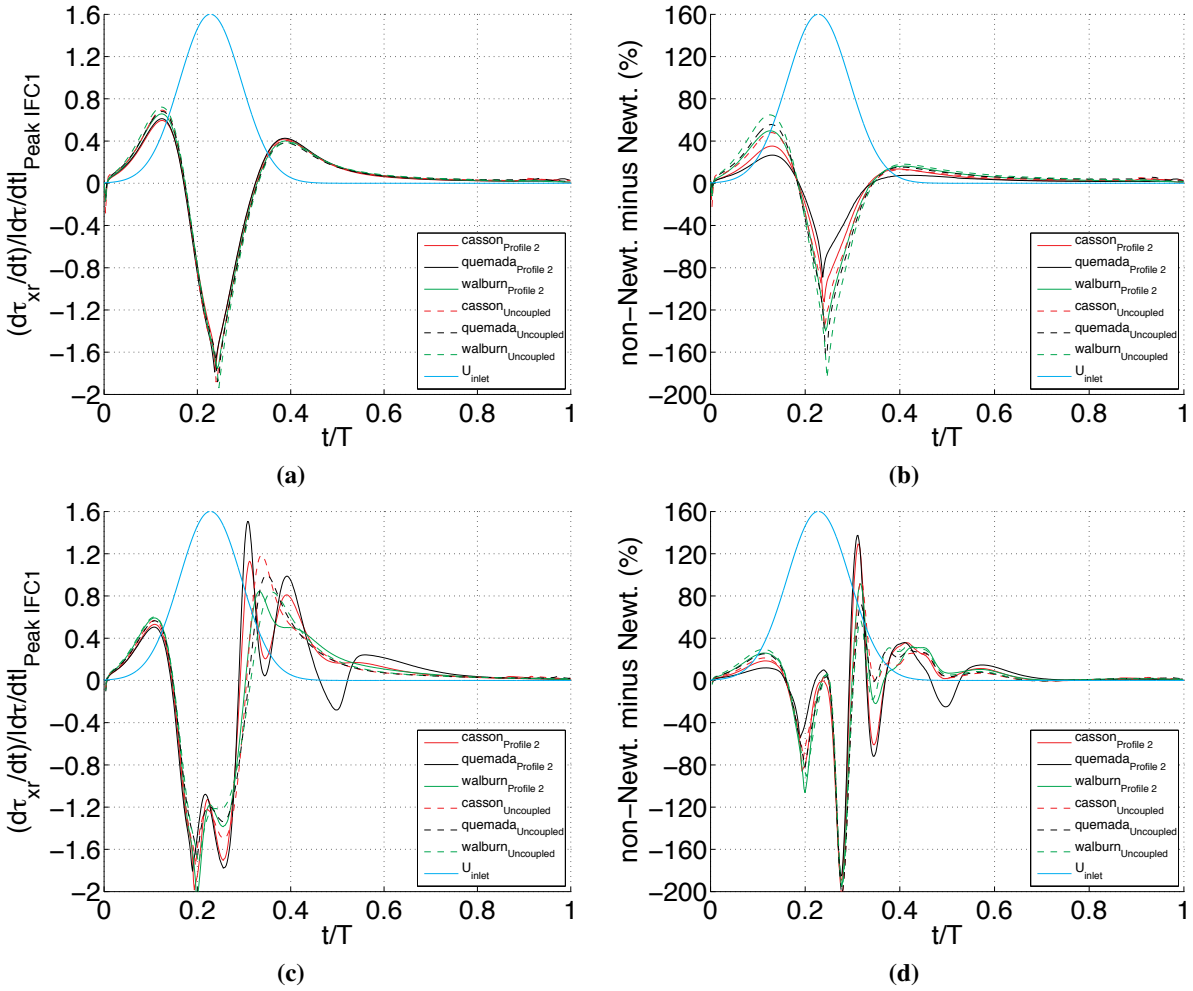

Figure 5 A comparison of the temporal WSSG for IFC 2 and 3 at point x/d=0.58 and azimuthal angle 4.6° for all non-Newtonian models, top and bottom respectively. On the left, a) & c) normalized by the peaks of IFC 1 and on the right, b) & d) the difference between the non-Newtonian and Newtonian models.

of RBCs near the wall. The sharp increase and decrease in the temporal gradient, most importantly, is a function of the shear rate dependency of the non-Newtonian viscosity models. The magnitudes are regulated by the regional change in RBC volume fraction, as will be described in the following section. Regarding the increased flow rate of Inflow Case 3, the coupled models display increased unsteadiness consistent with the lower viscosities and higher shear rates, as shown in Figure 10, closer to the Newtonian behaviour. A comparison with the Newtonian model shows a peak in difference at t/T=0.2, consistent with the stagnation point formation described earlier. Large variations ensue after a second peak near t/T=0.26. The differences thereafter are primarily due to the large gradient differences with the Newtonian model.

A depiction of the focal nature of the temporal gradients on the outerwall compared to the Newtonian model, is displayed for points in time during systole in Figures 6 and 7. The Figures represent the inflow cases at 60 BPM, 1 and 3, showing the local temporal gradient magnitudes, both normalized by the peak of the Quemada model. The points in time show the focal downstream movement of the peak temporal WSSG on the outer wall, due to the shear thinning property of blood-like viscosity models. In both flow cases it is found that the distribution of the sharp peaks is greater and more focused on the outer wall than that found for the Newtonian model.

non-Newtonian WSS Dynamics

The regions where reversed flow are found offers insight into areas of unsteady near wall dynamics and can be obtained through the negative WSS (the shaded regions) patterns. Figure 8 shows the WSS vary during systole as compared to the Newtonian model, during which the most relevant dynamical behaviour takes place. The differences in WSS directional development are similar for profiles P1 and P2. Therefore only the behaviour due to inflow profile P2 is displayed.

Each of the non-Newtonian models shows a slightly

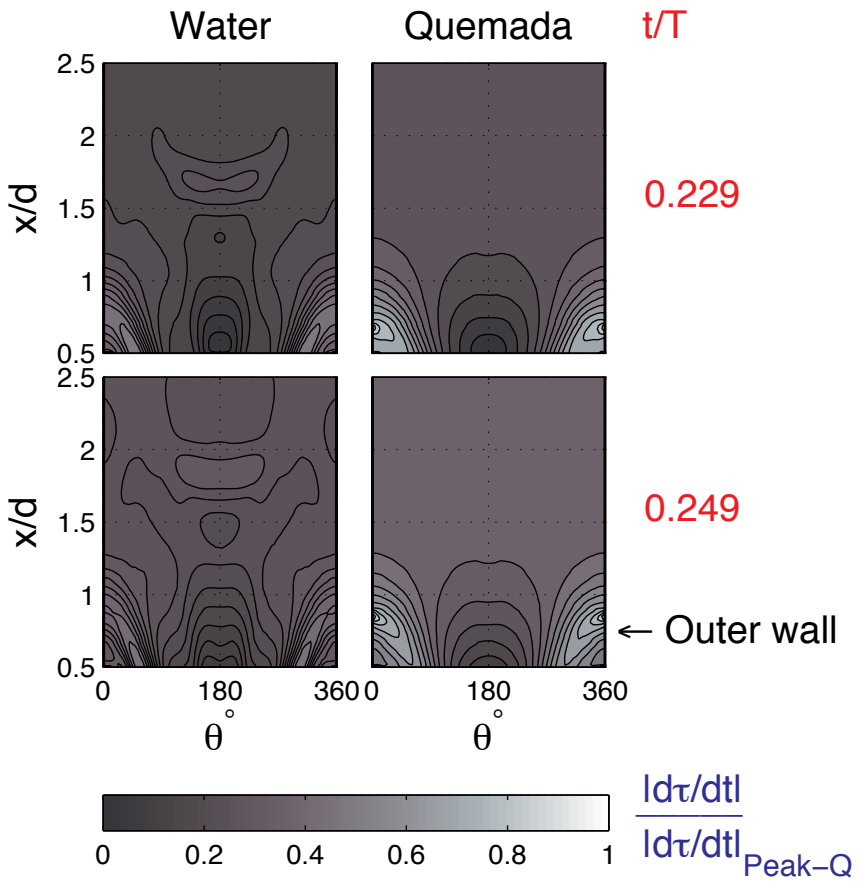

Figure 6 A non-Newtonian versus Newtonian model for the Temporal WSSG distribution at two points located within the investigated region for IFC 1. Plotted with respect to the axial and azimuthal co-ordinate system in Figure 4.

different time response to separation but with very similar patterns of formation for the respective inflow cases. At 60 BPM the time for the separation bubble to grow to approximately an axial position of x/d=1 on the outer wall takes place at around t/T=0.261, after systole. Increasing the frequency to 90 BPM there is a delay in the growth to a similar size at around t/T=0.273, which is expected with respect to equation 14. At double the flow rate i.e. Inflow Case 3, the growth is accelerated due to increased centrifugal forces and appears earlier at around t/T=0.23. In each of the flow cases, the separation bubble size of the Newtonian model extends approximately 20 % further downstream than the non-Newtonian models. In general, non-Newtonian separated flow takes place closer to the bifurcation during systole than the Newtonian model. For each of the studied cases reversed flow develops further downstream at the outer wall for the Newtonian model. Therefore it does not fully represent the localised nature of the unsteadiness closer to arterial bifurcations.

The point used to analyse the temporal WSSGs is also used for the WSS components to describe the relation to the temporal WSSG. In Figure 9 both axial and azimuthal WSS components are plotted to study the effect of both separated and secondary flow patterns during the heart pulsation for each inflow case. In Figure 9 each case is normalized by the mean of peak WSS magnitudes ($\overline{|\tau|_{Peaks}}$) of the coupled non-Newtonian models. The temporal development of the axial WSS dynamics for Inflow Cases 1 (60 BPM) and 2 (90 BPM) are represented by Inflow Case 2 in Figure 9 due to the similarity in trend. The peak to peak difference is greater though, defining the larger temporal WSSG displayed earlier for Inflow Case 2, due to the change taking place over a similar time scale. Inflow Case 1 and 2 display the same mean peak WSS magnitude indicating that it is a function of the Reynolds number. Regarding the azimuthal component, the flow does not change direction towards the inner wall during diastole, as observed for the Newtonian model. Here, the negative direction indicates flow towards the outer wall. This implies that particulate matter is constantly transported towards regions prone to plaque formation.

In general the coupled models display lower WSS magnitudes, as compared to each respective uncoupled model, due to the dilution taking place, shown in Figure 10. The Quemada model displays the lowest WSS magnitudes due to the lowest defined viscosity, caused by the lowest pre-

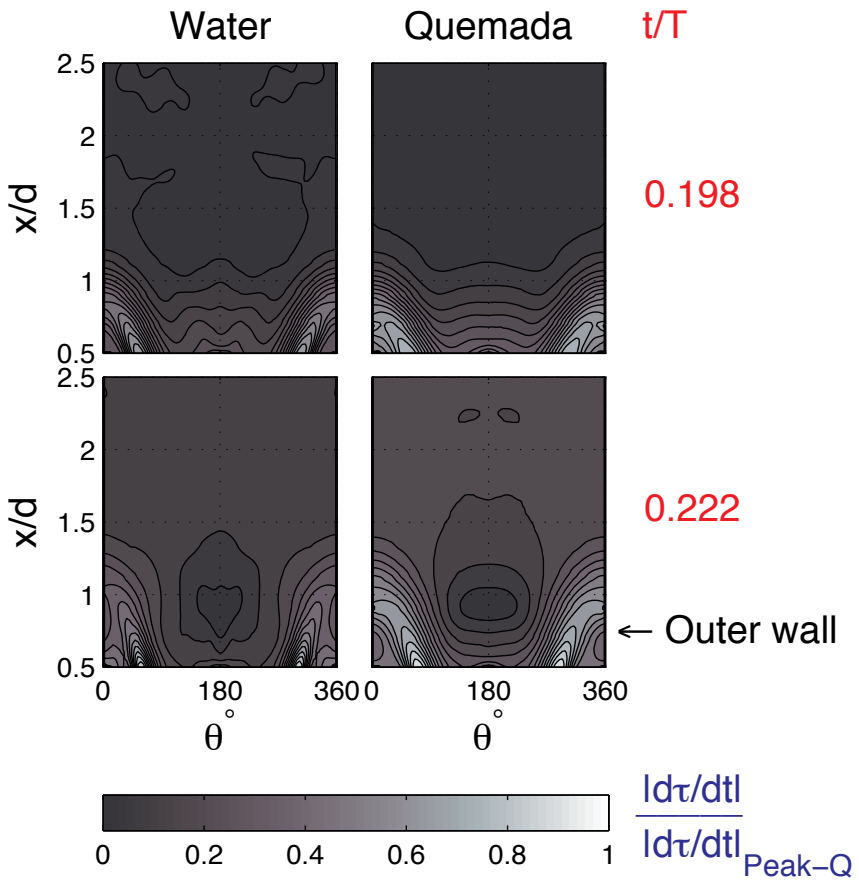

Figure 7 A non-Newtonian versus Newtonian comparison of the Temporal WSSG distribution at points in time of the investigated region for IFC 3. Plotted with respect to the axial and azimuthal co-ordinate system in Figure 4.

dicted RBC volume fraction, in turn leading to higher shear rates. Due to dilution, the increased flow rate displays the effect of decreased viscosity through the fluctuations of the WSS, displayed in Figure 9. Unsteadiness caused by the complex seconday flows after the peak in back flow, is observed in both the axial and azimuthal components. The coupled models display behaviour more similar to that of the Newtonian model in terms of the increases in oscillating WSS inside the separation bubble. At the higher flow rate, both WSS components become less comparable to the peak magnitude during the acceleration stage of systole, caused by the much higher shear at the inner wall due to the larger centrifugal forces.

Coupled vs Uncoupled non-Newtonian Flow

The local RBC volume fraction through the coupled non-Newtonian models has been shown to influence the fluctuation in WSS, Figure 9. Figures 11 and 12 display the variation via the terms of Navier Stokes equation, equation 11, and the non-Newtonian viscosity variables, respectively, at a point inside the separation bubble for a pulsation frequency of 60 BPM i.e. Inflow Case 1. This frequency is used in order to illustrate the effect of coupled vs uncoupled viscosity modelling on the flow field dynamics. The position chosen is located 10 % in the daughter branch diameter (d) in the radial direction (away from the wall) and coincides axially with the analysed position at the wall. As discussed in the previous section the results indicate that the flow unsteadiness inside the separation bubble may be important to atherogenic processes due to its correlation with the near wall dynamics. In Figure 11, the magnitudes of the transient and convective acceleration terms, the pressure gradient and divergence of viscous stress terms of the momentum equation, are plotted over the pulsation cycle. Most notably of all the terms is the viscous diffusion term ($\mu\nabla^2 u$) shows that with decreasing viscosity the diffusion is lower throughout the cycle. The coupled non-Newtonian models display less diffusion as compared to the uncoupled models during the accelerating and decelerating stages of the flow. At the onset of the bubble formation near peak flow, t/T =0.2, the lowest value is reached for all models. The largest discrepancy in viscous diffusion between the models occurs during the decelerating stage where secondary flows become more influential. This can be explained by Figure 12, showing that a minimum RBC volume fraction is reached near peak sys-

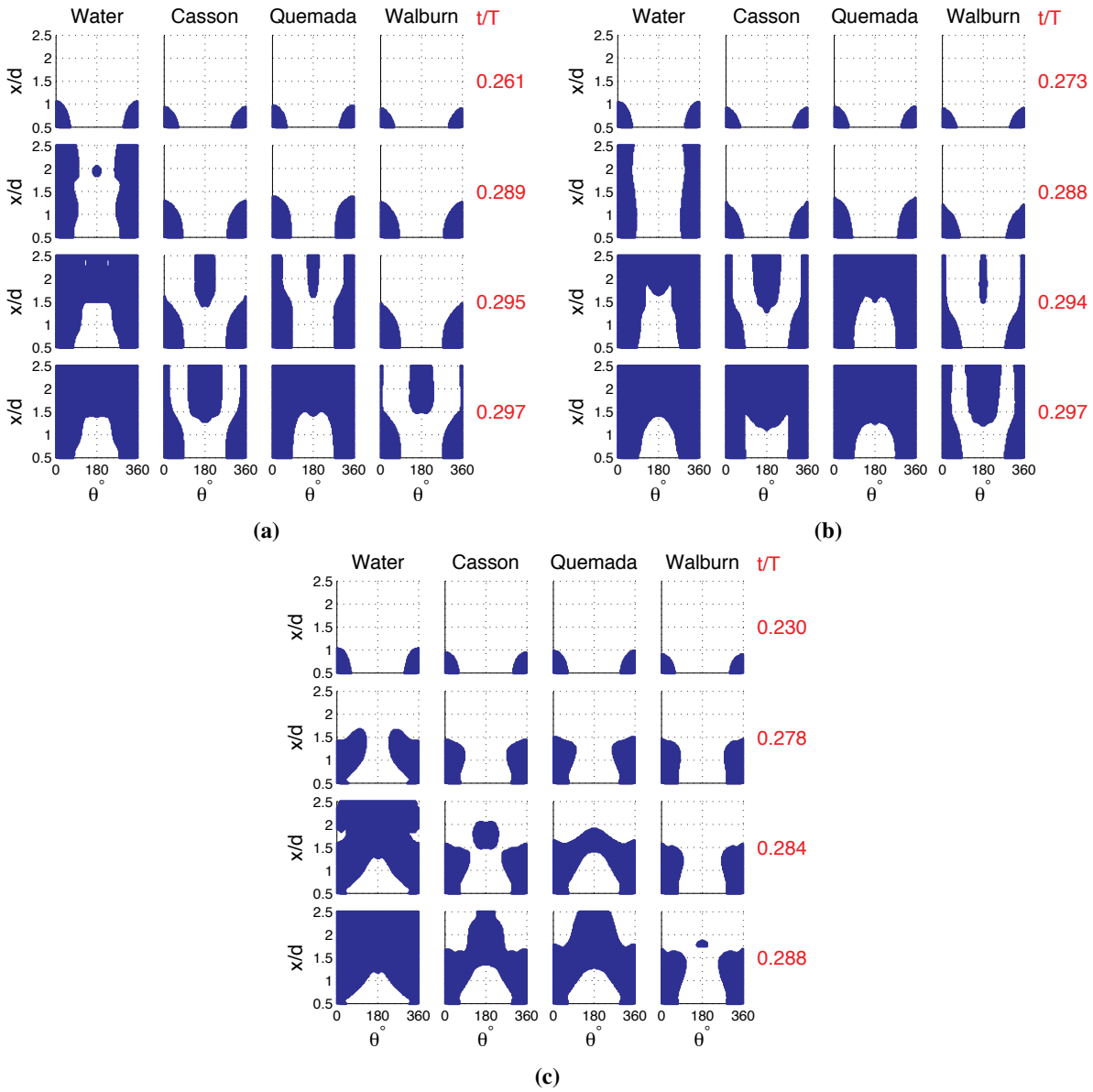

Figure 8 A comparison of regions of negative axial WSS or backflow (blue shaded regions) between the coupled non-Newtonian models and Newtonian (water) model, horizontally at points in time during the cycle for Inflow Cases (a) 1, (b) 2 (c) 3. Plotted with respect to the axial and azimuthal co-ordinate system in Figure 4.

tole. This leads to lower viscosity throughout most of the cycle. At the same time, higher shear rates exist, partly due to the lower flow resistance caused by the lower RBC fraction. This also leads to a further decrease in viscosity. The lower levels of viscous diffusion lead to higher levels of convection ($\nabla.(\rho uu)$) throughout the pulsation cycle, but still lower than the Newtonian model. The unsteady acceleration ($\rho\frac{du}{dt}$) and pressure gradient (∇p) terms show similar peaks at approximately t/T=0.15, before a fast decrease to a minimum at t/T=0.22. A fast increase in both terms leads to a second maximum, where the coupled models produce higher pressure losses and levels of unsteadiness compared to the uncoupled models, yet lower than for the Newtonian model.

During systole, RBC dilution inside the separation bubble may lead to a decrease in viscous diffusion by as much as 100 %, considering the Quemada model in Figure 11. In general, the coupled models display lower values than the uncoupled models throughout the cycle, especially during the acceleration and deceleration stages of systole. This implies that the uncoupled models under-estimate convection and unsteadiness, as shown in Figure 11. The increase in velocity gradients inside the separation bubble signifies more complex flows, shown by the greater fluctuation in the convective acceleration term in Figure 11 and the higher shear rates in Figure 12 during systole.

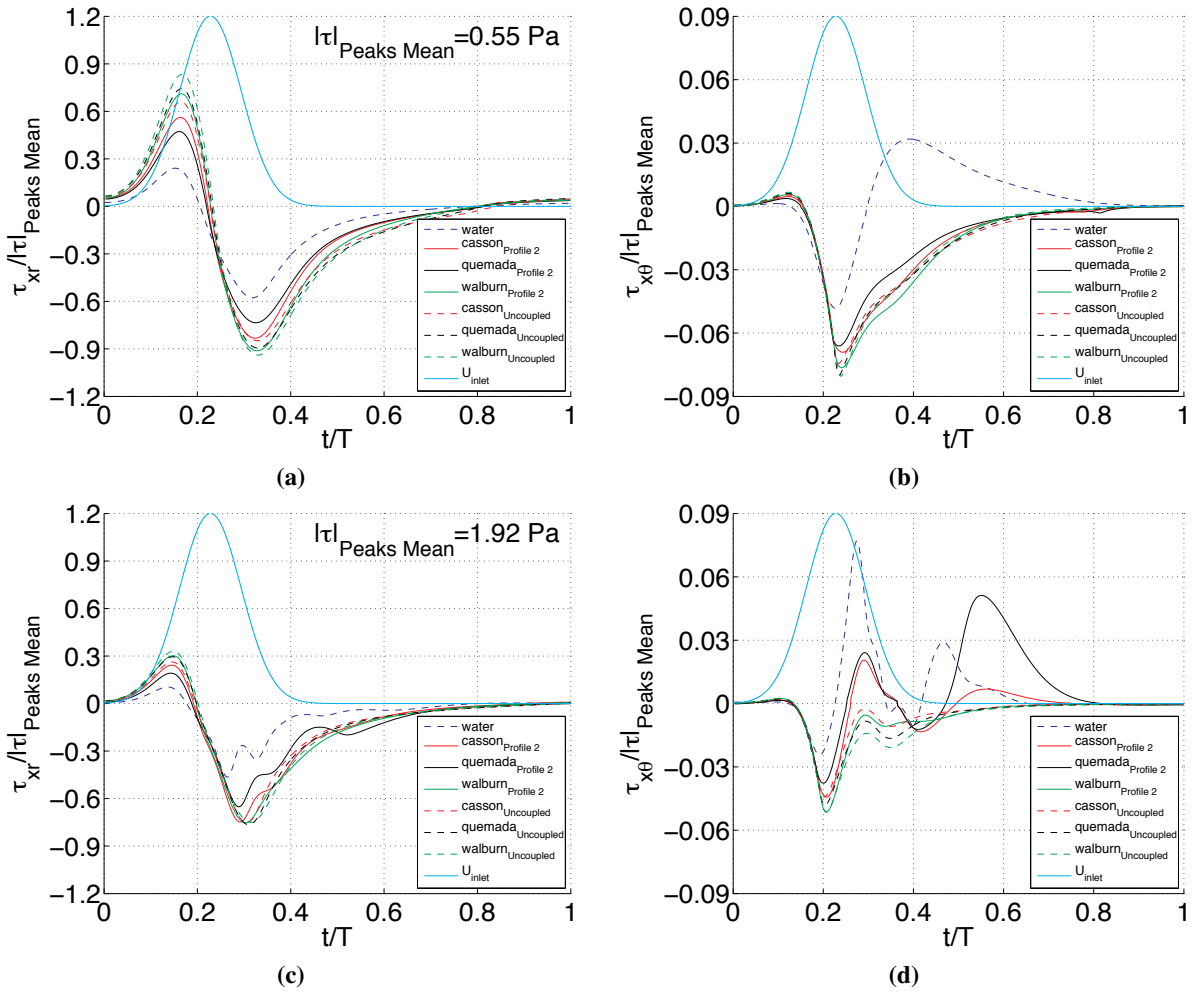

Figure 9 A comparison of axial (left) and azimuthal (right) normalized WSS variations between the coupled non-Newtonian and Newtonian (water) models at point x/d=0.58 and azimuthal angle 4.6°: (a) and (b) IFC 1; (c) and (d) IFC 3.

Influence of RBC Inflow profile

The inlet RBC distribution may produce large variations in the viscosity due to RBC dilution effects, especially in the region near the bifurcation. These variations have been shown to influence the absolute values and derivatives in the WSS. Figure 13 shows that there is a distinct difference between the peak temporal gradients defined by both the Quemada and Casson models of between 18 % and 28 %, respectively, normalized with the peak value of each profile P2 model. The pulsation frequency of 90 BPM (Inflow Case 2), is chosen for comparison due to the higher sensitivity of the temporal gradient, displayed earlier in Figure 5, to a frequency increase. These results in conjunction with Figure 14, shows that at lower volume fractions the shear rate dependency of the non-Newtonian viscosity models becomes less influential in affecting the fluctuating WSS. The peak temporal gradient decreases with the occurrence of the stagnation point. This can be explained through Figure 1, where it is observed that as the volume fraction decreases the change in shear rate has a less signif-

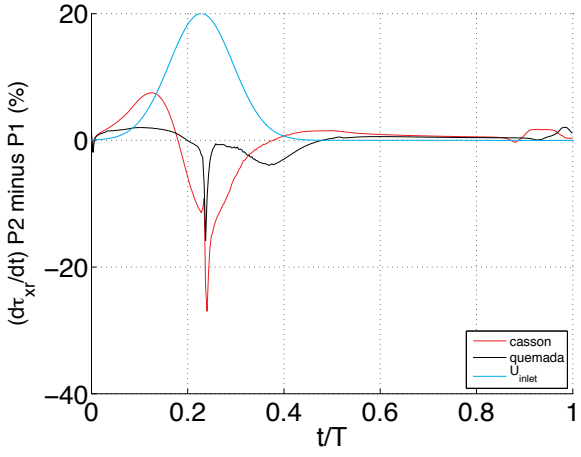

Figure 13 Percentage Difference between the temporal derivatives for inlet profiles P2 and P1, respectively, at outer wall position x/d=0.58 and 4.6° for the coupled Casson and Quemada models, normalized by the peak values of P2 coupled models.

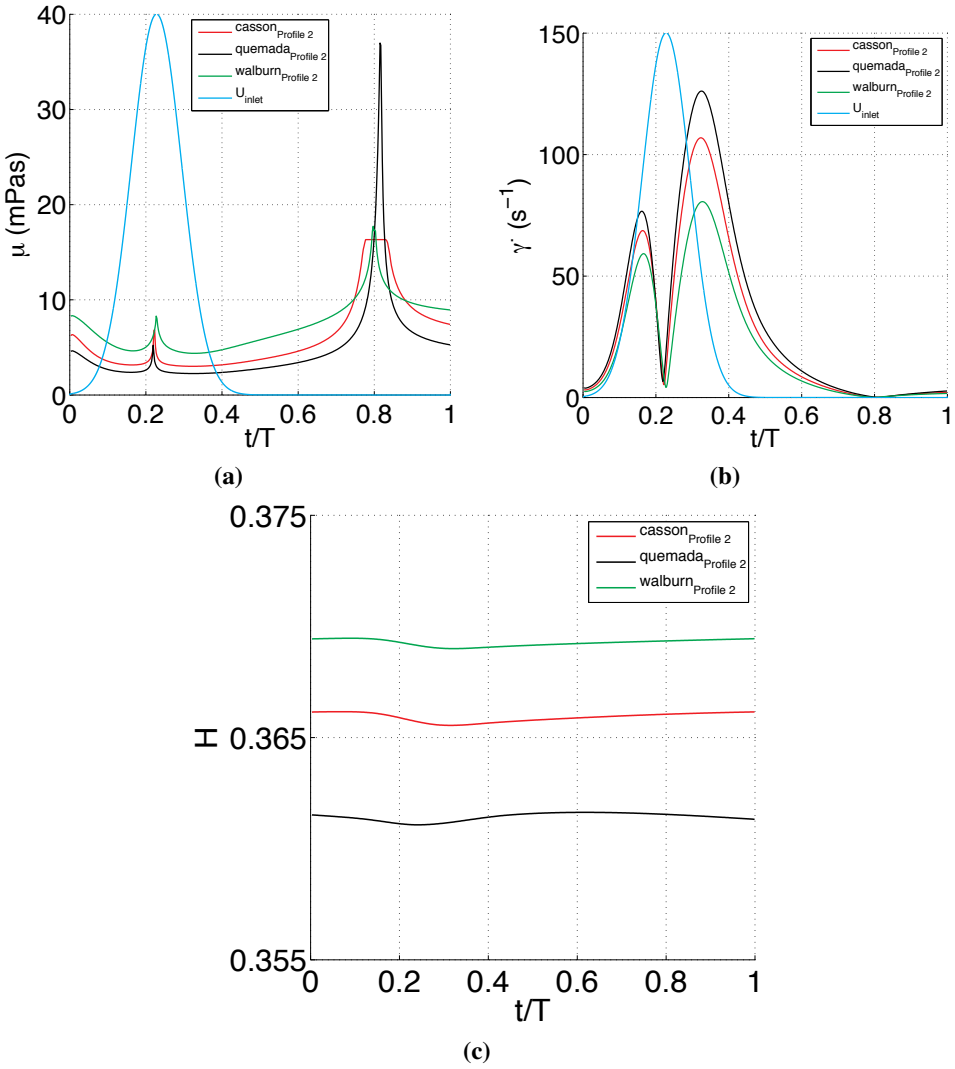

Figure 10 Time history of viscosity, shear rate and H throughout the heart-cycle for the coupled non-Newtonian models, at point x/d=0.58 and azimuthal angle 4.6°.

icant effect on the change in viscosity. Physically this may indicate the existence of less RBCs, on which the shear rate dependency is based, to resist flow.

Influence of RBC Diffusivity

During this study all data considered reflects a value for diffusivity equal to a Schmidt number (Sc) of approximately 110. A value of Sc=11 was also studied but produced no significant difference in the absolute values and development of the WSS, when comparing all Inflow Cases. In a previous study the convective properties have been shown to become more dominant at an Sc number greater than 11 [41].

Discussion and Conclusions

The relation of haemodynamics, via the complete non-Newtonian fluid mechanical aspects, to the atherogenic processes has been investigated. Numerical studies in the past have concluded that a Newtonian viscosity model is adequate in describing relevant mean physiological parameters at medium to high shear rates relevant to large arteries [21, 40]. There is evidence that the non-Newtonian character of blood is important in the region of bifurcations and curvatures, due to shear induced dilution [41]. Large variations in RBC fraction causes large variations in the local viscosity, as Figure 1 illustrates. It is therefore reasonable that the characteristic of separated and reversed flows are strongly affected by the viscosity variations. The unsteadiness or high gradient anomalies in the WSS have been hypothesized to be the mechanisms initiating or enhancing atherogenesis over many years.

In this study support is given to the localisation of sep-

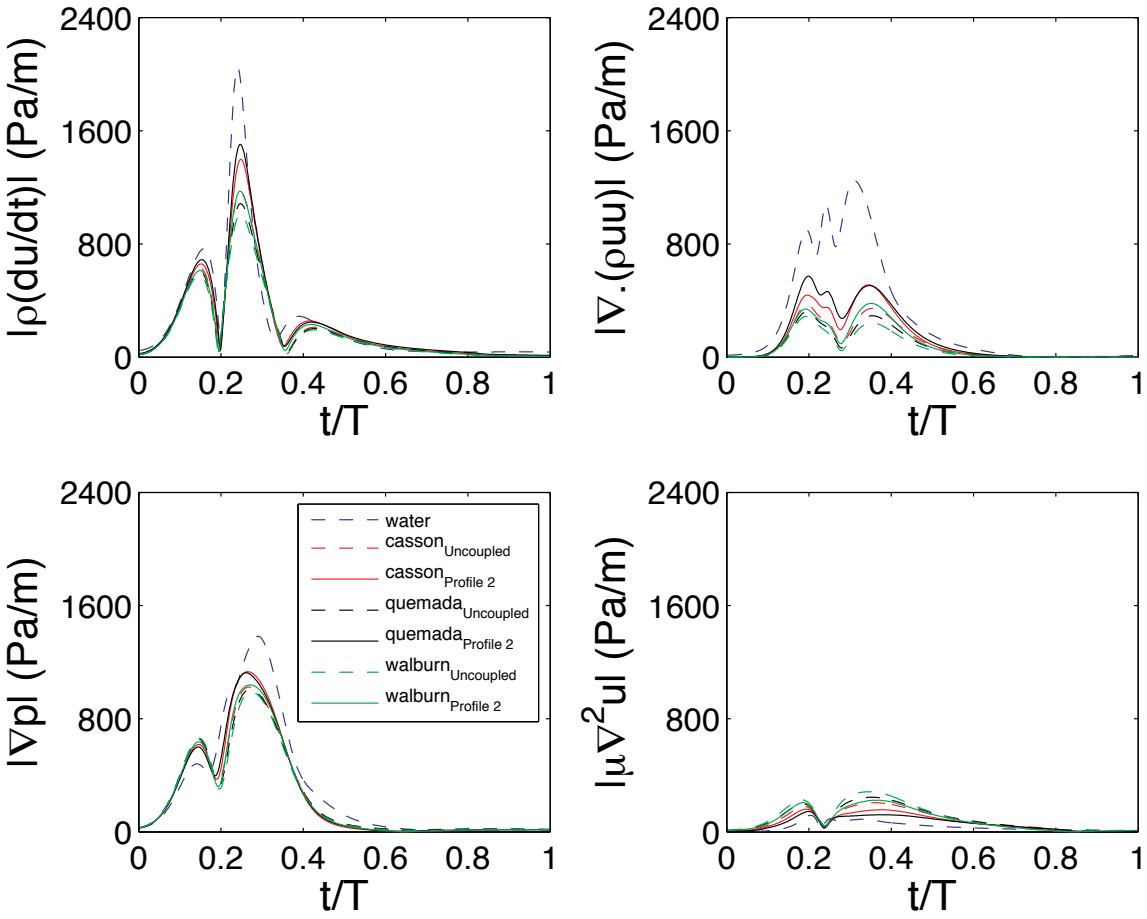

Figure 11 A comparison of the terms of equation 11, considering the differences between the non-Newtonian models, coupled and uncoupled, and the Newtonian model.

arated and secondary flows close to the bifurcation, during systole. The importance of non-Newtonian viscosity parameters in identifying physiological flow features is demonstrated. These flow regimes and sudden increases in rates of unsteadiness in the near wall region are closely associated to commonly known diseased regions near the bifurcation. During this study, separated flows related to regions of unsteadiness are shown to be more focal to the region of the bifurcation than what the Newtonian flow model predicts. Moreover, previous studies also define the flow through non-Newtonian models but never consider the variation in RBC volume fraction. In this study the variation in RBC volume fraction in the region of the bifurcation is shown to decrease by up to 40 % at a point inside the separation bubble region for the coupled non-Newtonian models, displayed in Figure 12. This has a direct influence on the terms defining the properties of the flow. The dilution behaviour decreases the viscosity near to the bifurcation due to the formation of the separation bubble, leading to a decrease in the WSS magnitudes from peak to peak during the WSS cycle at the outer wall. Comparison with the uncoupled non-Newtonian models shows over prediction of the WSS magnitudes and damp possible fluctuations due to the flow being too viscous. It is a direct effect of not considering the local volume of RBC, where RBC depleted regions decrease the viscosity.

The most striking property of the analysed flows is the distinct focal development of temporal WSS gradients on the outer wall near to the bifurcation. It is in this region of the arterial wall in 90-degree bifurcations that the most prominent plaques form [42]. A focused region of sharp increase in temporal WSSG is observed to be moving downstream during systole, co-inciding with the stagnation point that forms immediately behind the separation bubble. This is also observed to an extent in the Newtonian flow, but not nearly with the same impact on the gradient as observed due to intrinsic properties of the blood-like non-Newtonian viscosity models. The temporal WSSG can be as high as 200 % larger compared to the defined value by the Newtonian model, considering the uncoupled models. This can however be seen to be an over-estimation of approximately 100 % due to neglect of the volume fraction effects accounted for by the coupled viscosity models, as display in Figure 5. The increase in gradient is not only

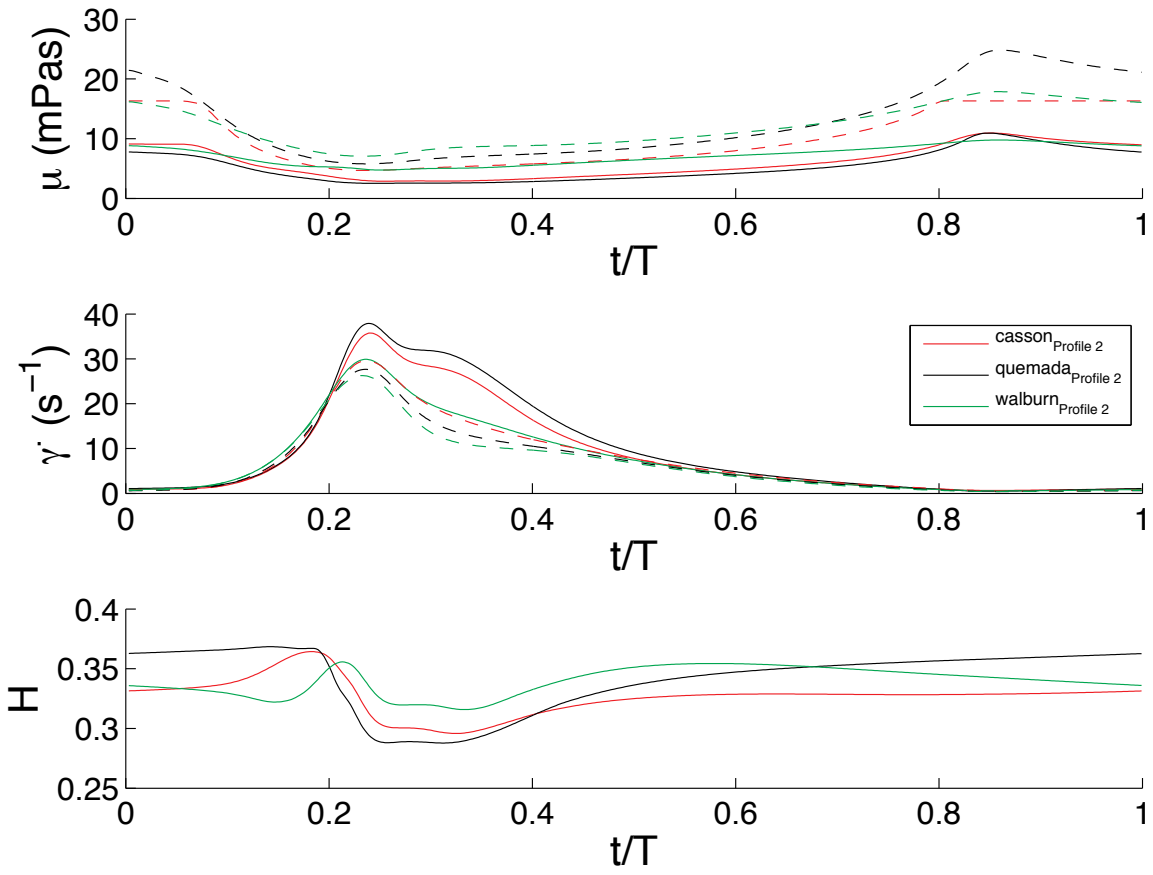

Figure 12 The time-evolution of viscosity, shear rate and H throughout the pulsation cycle for all non-Newtonian models, at point x/d=0.58 and azimuthal angle 4.6°, 10 % radially inwards from the wall.

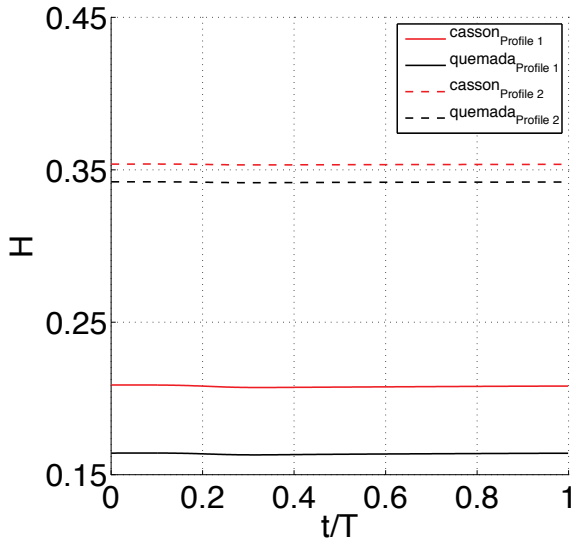

Figure 14 RBC volume fractions of inlet profiles P2 and P1, at outer wall position x/d=0.58 and 4.6° for the coupled Casson and Quemada models.

larger but increases very suddenly as well, due to the shear dependency of the non-Newtonian viscosity models. The existence of the stagnation point is the cause of a sudden decrease in shear at the wall, which in turn leads to a sudden increase in viscosity. Cell proliferation in the endothelial layer has been shown to be enhanced in vitro in regions of sudden increase in temporal WSSGs [17, 27, 44]. It is also evident that from these experiments that spatial WSSGs are not as important as the temporal WSSGs. The process of cell proliferation is thought to be the initiating process in atherogensis, pre-fatty streak formation. There is also evidence that temporal gradients in WSS, and not the absolute WSS, induce expression of bio-chemicals important in the recruitment of monocytes for example in the inflammatory process [2]. Atherosclerosis has been described by many researchers to be an inflammatory disease [30, 34, 39]. Important details in the WSS dynamics or other important physiological parameters can be lost without the consideration of the intrinsic non-Newtonian viscous properties of the blood.

Acknowledgements

The financial support from the Swedish Research Council (Vetenskapsrådet) is greatly acknowledged. Com-

putational resources were provided by the Swedish National Infrastructure for Computing (SNIC) and the High Performance Computing Center North (HPC2N).

References

[1] P. Aarts, S. Van Den Broek, G. Prins, G. Kuiken, J. Sixma, and R. Heethaar. Blood platelets are concentrated near the wall and red blood cells, in the center in flowing blood. *Arteriosclerosis, Thrombosis, and Vascular Biology*, 8(6):819, 1988.

[2] X. Bao, C. Lu, and J. Frangos. Temporal gradient in shear but not steady shear stress induces pdgf-a and mcp-1 expression in endothelial cells: role of no, nfκb, and egr-1. *Arteriosclerosis, thrombosis, and vascular biology*, 19(4):996–1003, 1999.

[3] B. Bharadvaj, R. Mabon, and D. Giddens. Steady flow in a model of the human carotid bifurcation. part i–flow visualization. *Journal of Biomechanics*, 15(5):349–362, 1982.

[4] B. Bharadvaj, R. Mabon, and D. Giddens. Steady flow in a model of the human carotid bifurcation. part ii–laser-doppler anemometer measurements. *Journal of Biomechanics*, 15(5):363–365, 1982.

[5] J. Bronzino, editor. *The Biomedical Engineering Handbook, second edition*. Boca Raton: CRC Press LLC, 2000.

[6] D. Brooks, J. Goodwin, and G. Seaman. Interactions among erythrocytes under shear. *Journal of applied physiology*, 28(2):172, 1970.

[7] C. Caro. The dispersion of indicator flowing through simplified models of the circulation and its relevance to velocity profile in blood vessels. *The Journal of Physiology*, 185(3):501, 1966.

[8] C. Caro. Discovery of the role of wall shear in atherosclerosis. *Arteriosclerosis, thrombosis, and vascular biology*, 29(2):158, 2009.

[9] C. Caro, J. Fitz-Gerald, and R. Schroter. Arterial wall shear and distribution of early atheroma in man. *Nature Publishing Group*, 1969.

[10] C. Caro, J. Fitz-Gerald, and R. Schroter. Atheroma and arterial wall shear observation, correlation and proposal of a shear dependent mass transfer mechanism for atherogenesis. *Proceedings of the Royal Society of London. Series B. Biological Sciences*, 177(1046):109, 1971.

[11] C. Caro and M. Lighthill. Velocity distribution in models of the circulation measured by indicator dispersion. *J Physiol*, 183:34, 1966.

[12] N. Casson. *Rheology of disperse systems*. Pergamon Press, London, 1959.

[13] S. Charm and G. Kurland. Blood rheology. *Cardiovascular fluid dynamics*, 2, 1972.

[14] G. Cockelet. The rheology and tube flow of blood. *Handbook of Bioengineering*, page 14, 1987.

[15] G. Cockelet, E. Merrill, E. Gilliland, H. Shin, A. Britten, and R. Wells Jr. The rheology of human blood–measurement near and at zero shear rate. *Journal of Rheology*, 7:303–307, 1963.

[16] J. Cutnell and K. Johnson. *Physics, 8th Edition*. Wiley, 1998.

[17] N. DePaola, P. Davies, W. Pritchard, L. Florez, N. Harbeck, and D. Polacek. Spatial and temporal regulation of gap junction connexin43 in vascular endothelial cells exposed to controlled disturbed flows in vitro. *Proceedings of the National Academy of Sciences*, 96(6):3154, 1999.

[18] N. DePaola, M. Gimbrone, P. Davies, and C. Dewey. Vascular endothelium responds to fluid shear stress gradients. *Arteriosclerosis, Thrombosis, and Vascular Biology*, 12(11):1254–1257, 1992.

[19] J. Duguid and W. Robertson. Mechanical factors in atherosclerosis. *Lancet*, 272(6981):1205, 1957.

[20] P. Evegren, L. Fuchs, and J. Revstedt. On the secondary flow through bifurcating pipes. *Physics of Fluids*, 22:103601, 2010.

[21] P. Evegren, L. Fuchs, and J. Revstedt. Wall shear stress variations in a 90-degree bifurcation in 3d pulsating flows. *Medical engineering & physics*, 32(2):189–202, 2010.

[22] T. Farmakis, J. Soulis, G. Giannoglou, G. Zioupos, and G. Louridas. Wall shear stress gradient topography in the normal left coronary arterial tree: possible implications for atherogenesis. *Current Medical Research and Opinion®*, 20(5):587–596, 2004.

[23] D. Fry. Acute vascular endothelial changes associated with increased blood velocity gradients. *Circulation Research*, 22(2):165, 1968.

[24] V. Gambillara, G. Montorzi, C. Haziza-Pigeon, N. Stergiopulos, and P. Silacci. Arterial wall response to ex vivo exposure to oscillatory shear stress. *Journal of vascular research*, 42(6):535–544, 2005.

[25] H. Goldsmith. *Red cell motions and wall interactions in tube flow.*, volume 30. Federation proceedings, 1971.

[26] H. Goldsmith and S. Mason. Some model experiments in hemodynamics iv. *Theoretical and Clinical Hemorheology, Springer, New York*, pages 47–59, 1971.

[27] M. Haidekker, C. White, and J. Frangos. Analysis of temporal shear stress gradients during the onset phase of flow over a backward-facing step. *Journal of biomechanical engineering*, 123:455, 2001.

[28] D. Ku, D. Giddens, C. Zarins, and S. Glagov. Pulsatile flow and atherosclerosis in the human carotid bifurcation. positive correlation between plaque location and low oscillating shear stress. *Arteriosclerosis, Thrombosis, and Vascular Biology*, 5(3):293–302, 1985.

[29] M. Lei, D. Giddens, S. Jones, F. Loth, and H. Bassiouny. Pulsatile flow in an end-to-side vascular graft model: comparison of computations with experimental data. *Journal of biomechanical engineering*, 123:80, 2001.

[30] P. Libby, P. Ridker, and A. Maseri. Inflammation and atherosclerosis. *Circulation*, 105(9):1135, 2002.

[31] G. Lowe, F. Fowkes, J. Dawes, P. Donnan, S. Lennie, and E. Housley. Blood viscosity, fibrinogen, and activation of coagulation and leukocytes in peripheral arterial disease and the normal population in the edinburgh artery study. *Circulation*, 87(6):1915, 1993.

[32] D. McDonald. Blood flow in arteries. *Baltimore, Williams and Wilkins Co*, 1960.

[33] E. Merrill, E. Gilliland, G. Cokelet, H. Shin, A. Britten, and R. Wells Jr. Rheology of human blood, near and at zero flow:: Effects of temperature and hematocrit level. *Biophysical Journal*, 3(3):199–213, 1963.

[34] F. Montecucco and F. Mach. Atherosclerosis is an inflammatory disease. In *Seminars in immunopathology*, volume 31, pages 1–3, 2009.

[35] T. Nagel, N. Resnick, C. Dewey Jr, and M. Gimbrone Jr. Vascular endothelial cells respond to spatial gradients in fluid shear stress by enhanced activation of transcription factors. *Arteriosclerosis, thrombosis, and vascular biology*, 19(8):1825, 1999.

[36] K. Perktold, M. Resch, and H. Florian. Pulsatile non-newtonian flow characteristics in a three-dimensional human carotid bifurcation model. *Journal of biomechanical engineering*, 113:464, 1991.

[37] D. Quemada. Rheology of concentrated disperse systems and minimum energy dissipation principle. *Rheologica Acta*, 16(1):82–94, 1977.

[38] D. Quemada. Rheology of concentrated disperse systems ii. a model for non-newtonian shear viscosity in steady flows. *Rheologica Acta*, 17(6):632–642, 1978.

[39] R. Ross et al. Atherosclerosis is an inflammatory disease. *American Heart Journal*, 138:419–420, 1999.

[40] J. Soulis, G. Giannoglou, Y. Chatzizisis, K. Seralidou, G. Parcharidis, and G. Louridas. Non-newtonian models for molecular viscosity and wall shear stress in a 3d reconstructed human left coronary artery. *Medical engineering & physics*, 30(1):9–19, 2008.

[41] S. van Wyk, L. Prahl Wittberg, and L. Fuchs. Haemodynamics in a 3d 90-degree bifurcation. In *ECCOMAS Thematic International Conference on Simulation and Modeling of Biological Flows*, 2011.

[42] P. VanderLaan, C. Reardon, and G. Getz. Site specificity of atherosclerosis. *Arteriosclerosis, thrombosis, and vascular biology*, 24(1):12–22, 2004.

[43] F. Walburn and D. Schneck. A constitutive equation for whole human blood. *Biorheology*, 13(3):201, 1976.

[44] C. White, M. Haidekker, X. Bao, and J. Frangos. Temporal gradients in shear, but not spatial gradients, stimulate endothelial cell proliferation. *Circulation*, 103(20):2508–2513, 2001.

[45] C. Zarins, D. Giddens, B. Bharadvaj, V. Sottiurai, R. Mabon, and S. Glagov. Carotid bifurcation atherosclerosis. quantitative correlation of plaque localization with flow velocity profiles and wall shear stress. *Circulation Research*, 53(4):502, 1983.

[46] A. Zydney, J. Oliver III, and C. Colton. A constitutive equation for the viscosity of stored red cell suspensions: Effect of hematocrit, shear rate, and suspending phase. *Journal of Rheology*, 35:1639, 1991.